5-2015

pH SENSING AND IMAGING WITH NANOPARTICLES AND IMPLANTABLE FILMS

Fenglin Wang
Clemson University, fengliw@g.clemson.edu

pH SENSING AND IMAGING WITH NANOPARTICLES AND IMPLANTABLE FILMS

A Dissertation
Presented to
the Graduate School of
Clemson University

In Partial Fulfillment
of the Requirements for the Degree
Doctor of Philosophy
Chemistry

---

by
Fenglin Wang
May 2015

Accepted by:
Dr. Jeffrey N. Anker , Committee Chair
Dr. George Chumanov
Dr. Kenneth A. Christensen
Dr. Frank Alexis

ABSTRACT

pH is a very important parameter in biological systems. Monitoring pH in situ may provide useful information for studying pH regulated cellular events, diagnosing diseases and assessing treatment efficacy. Various strategies have been introduced for developing pH sensors. However, it is still challenging to monitor pH in biological systems with high specificity, especially through thick tissue. In this dissertation, we describe three types of pH sensors which are used to noninvasively monitor pH in living cells, monitor and map bacterial growth caused pH variation through thick tissue with minimal autofluorescence background. In Chapter 2, a pH nanosensor with high specificity and sensitivity is developed based on surface-enhanced Raman scattering by encapsulating 4-mercaptobezonic acid functionalized silver nanoparticles in a proton permeable silica shell. The performance of silica protected nanosensor against aggregation and biomolecular interference is investigated. The nanosensors are introduced to report intracellular pH in living macrophages. In Chapter 3, a pH sensor film is designed for monitoring pH variation on a surface through thick tissue in real time. The pH sensor film is composed of a film of upconverting nanoparticles which functions as a local light source and a thin layer of pH indicator which modulates the luminescence in a pH dependent way. Upconverting nanoparticles are excited by near infrared laser (980 nm) which allows high tissue penetration depth and avoids autofluorescence from tissue. The pH sensor film is applied to monitor bacterial growth

caused pH decrease at the interface of sensor film and trypic soy agar in real time through 6 mm porcine tissue. In Chapter 4, a pH sensor film with the ability to image pH variation through thick tissue with high spatial resolution is designed utilizing X-ray radioluminescent particles as a local light source. pH calibration curves are generated by taking the ratio of peak intensity at 620 nm over that at 700 nm. By creating a localized reference region on the sensor film, the tissue effect on the ratio of the two peaks is adjusted. The pH sensor film is used to monitor bacterial growth and study antibiotic effect with millimeter of spatial resolution which is primarily determined by the width of the X-ray beam. Both upconverting luminescence and X-ray radioluminesce based pH sensors have the potential to revolutionize the ability to diagnose and assess treatment for implanted medical devices associated bacterial infection.

DEDICATION

This work is dedicated to my husband, Shun Xiang, my parents, Jialiang Wang and Juying Cai, and my brother, Xingyi Wang.

ACKNOWLEDGMENTS

I would like to thank my advisor Dr. Jeffrey N. Anker for his support and guidance. Dr. Anker is always so helpful. Without his help, my projects could not progress this smooth. I would also like to thank my committee members, Dr. George Chumanov, Dr. Kenneth A. Christensen and Dr. Frank Alexis. Thanks for their suggestions and support on my research projects and career development.

I am very grateful to have the opportunity to pursue my PhD and conduct research in Chemistry Department, Clemson University. I would like to thank my collaborator Yash Raval from Dr. Tzuen‐Rong J. Tzeng's lab for conducting the bacterial study and animal model together. I really appreciate the collaboration between Dr. Thomas Moore from Dr. Alexis Frank's lab, developing nanoprobes for monitoring drug release in living cells. I would like to thank the stuff in Godley-Snell Research Center for helping me with the animal studies. I would also like to thank all my colleagues in Dr. Anker's group for their help, encouragement and support, especially KhanhVan Nguyen, Hongyu Chen and Melissa Rogalski. In addition, I really appreciate all the other friends I have had during my time in Clemson University, thanks for their care and help.

Last but not least, I really appreciated the time I spent with my host family Anita and Dick. I would like to thank my parents and brother for their support and encouragement. I would especially like to thank my husband Shun Xiang for his support, love and company. We will enjoy the journey together.

TABLE OF CONTENTS

Page

Table of Contents (Continued) Page

LIST OF TABLES

LIST OF FIGURES

List of Figures (Continued) Page

List of Figures (Continued) Page

CHAPTERS

CHAPTER 1. INTRODUCTION

1.1. Outline for this dissertation

In this dissertation, we developed three types of optical sensors for measuring pH in biological systems. A pH nanosensor was designed to measure intracellular pH based on surface-enhanced Raman scattering (SERS). pH sensor films based on inner filter effect between upconverting particles/ radioluminescent particles and pH indicators were developed and used to measure pH variation caused by bacterial growth through thick tissue in situ. Below is a brief description for each chapter.

Chapter One has introduced the background and some of the recent developments of the topics related to this dissertation. First, the concept, fabrication and application of pH sensor films, optical fibers and pH nanosensors were discussed. Then, the background, applications and recent developments of SERS were described. In this dissertation, both upconverting and raidoluminescent particles were introduced as localized light sources for sensor design. Hence, the mechanisms of upconversion process and some of the applications of upconverting nanoparticles are briefly discussed. The mechanism of radioluminescent materials, the concepts and applications of X-ray luminescence computed tomography (XLCT) and X-ray excited optical luminescence (XEOL) are also briefly summarized. Two of the projects were developing novel optical techniques which have great potential to monitor bacterial infection on implanted medical devices (IMDs) noninvasively. This chapter also described some properties of biofilms and the methods

for detecting bacteria in vitro and on IMDs. Last, the photon propagation through tissue and how that affects the spatial resolution of microscopy was briefly mentioned.

Chapter Two describes a robust pH nanosensor for measuring pH in complex biological systems. The sensor was based on SERS and they were prepared by encapsulating 4-mercaptobenzoic acid (4-MBA) functionalized silver nanoparticles with a thin proton permeable silica shell. The presence of silica shell successfully protects the nanosensor from interacting with proteins. The nanosensor is demonstrated to be responsive from pH 3.0 to 6.0 with a noise level of 0.1 pH units. Intracellular pH (endosomal pH) was successfully measured based on SERS.

Chapter Three presents a pH sensor film for measuring bacterial growth caused pH decrease on the film surface through tissue in real time. The sensor consists of an upconverting nanoparticle film acting as a local light source and a film of pH indicators to modulate the spectrum. pH calibration curves without and with tissue were generated by taking the ratio of the luminescence peak intensity at 671 nm/661 nm when the films were incubated with different standard buffers. Attributed to the close proximity of these two peaks, the tissue does not have a significant effect on the peak ratios. By growing bacteria at the interface of pH sensor film and tryptic soy agar (TSA) plate, a pH decrease was monitored over 40 h through 6 mm porcine tissue.

Chapter Four reports an X-ray excited luminescence chemical imaging (XELCI) technique for mapping pH variation on surfaces implanted in thick tissue. The pH sensor film comprises of a film of radioluminescent particles which functions a local light source and a thin film of pH indicators which modulates the radioluminescent spectrum

in a pH dependent manner. pH calibration curves without and with tissue were generated by taking the ratio of the luminescence peak intensity at 620 nm over that at 700 nm and a reference point (without pH indicator) was created on the sensor film to account for the tissue effect on the peak ratio. With XELCI, both bacterial growth caused pH decrease and the antibiotic caused pH restoration on the sensor film surface were imaged through 6 mm porcine tissue with millimeter spatial resolution.

Chapter Five summaries the work and discusses the future directions and some preliminary results of these projects.

1.2 pH sensors

pH is a very important parameter in a variety of fields from industrial to environmental to biomedical. In particular, pH is critical in life sciences, food and beverage processing, water and soil examination, and marine and pharmaceutical research. For instance, intracellular pH is essential for cell function as the activity of most proteins (enzymes) is regulated by proton concentration.[1] pH is tightly controlled in mammalian tissue, closely balanced among lactic acid production, interstitial fluid buffering and perfusion. Alterations in tissue pH may be associated with or lead to different pathological states such as inflammation, ischaemia, infection, renal disease, tumor, chronic lung disorders and intrauterine abnormalities.[2] pH can affect the fermentative pattern or even the fermentation products of lactic acid bacteria.[3] Rousk investigated effect of soil pH on fungal and bacterial decomposers. They found that

neural or slightly alkaline conditions favored bacterial growth while an acidic pH favored fungal growth.[4] pH smaller than 4.5 has a universal inhibition of all microbial variables, e.g. biomass and functional efficiency. In addition, the growth and metabolism of cells or bacteria can generate acidic species which can lower the localized pH. Monitoring pH variation could indicate the growth of cells or bacteria.[5] In particular, monitoring pH growth on implant surface may provide useful information for diagnosing bacterial colonization and infection.[6] Hence, developing techniques for measuring pH is of great importance.

The two most common methods to measure pH are electrochemical and optical strategies. pH electrode measures the activity of hydronium ions in aqueous solution using a reference electrode and a working electrode. The working electrode is made from a special glass which allows the hydronium ions exchange between the glass membrane and the surrounding solution. The potential, due to the difference in activities of hydronium ions between the test solution and reference solution, is measured with a pH meter and is proportional to the pH of the sample. A pH electrode is reliable and easy to use, has relatively low cost and can perform rapid measurements. It also has a wide working range using a two-point calibration method. However, pH electrode has several disadvantages which limit their applications in sensing pH inside cells and imaging pH in vivo. pH electrode has relatively large size which requires a relatively large sample volume and the glass membrane is rigid, fragile and not suitable for alkaline solutions. It is also susceptible to electrical interference and it also suffers from electrode signal drift which prevents its long-term measurements. In addition, biofouling and the constant

needs for calibration are problematic when they are introduced to measure pH in biological systems in vivo.

1.2.1 Design of optical pH sensors

Optical pH sensor offers an alternative approach. As compared to pH electrodes, optical pH sensors have several advantages. They can be miniaturized down to submicrometer or even nanometer dimensions. pH optical fiber sensors and pH nanosensors have been extensively studied and applied for monitoring intracellular pH. For instance, Tan and coworkers developed an optical fiber with a tip size of 0.1 μm and a response time of millisecond for monitoring pH within rat embryo.[7] Optical pH sensors do not need a reference sensor and their performance is not affected by electrical or electromagnetic interferences. They can be used for remote and on-line sensing with minimal invasiveness. Holobar et al. monitored pH in bioreactors using fluorescent sensors in 1993.[8] Lee et al. designed an embeddable microarray sensor to sense oxygen and pH variation in cell culture media noninvasively. The oxygen and pH sensitive probes were incorporated into poly(ethylene glycol) diacrylate precursor solution which was polymerized in a functionalized PDMS mold.[9] Optical pH sensors are capable of continuous measurements. However, they also have some disadvantages. One of the most severe issue is the limited long-term stability due to dye leaching and/or photobleaching, which could be improved or avoided through the choice of right pH indicator dyes, the

sensing mechanism, and referenced or ratiometric sensing strategy. Temperature and ionic concentration also need to be taken into account for reliable measurements.

Basic components of an optical pH sensor include the sample, the transduction platform and signal processing element (electronics) which measures the optical signal and correlates it to the pH of the sample. The optical transduction mechanisms are mainly based on reagents that change their optical properties in a pH dependent way. The most commonly measured optical properties are absorption, fluorescence intensity, decay time and reflectance.

Optical pH sensors are usually prepared by trapping pH indicators which are typically weak organic acids or bases in a proton permeable matrix. The working principle of an optical pH sensor is that the pH indicators have distinct optical properties in their protonated and depronated forms, which is closely related to the pH of the sample. The theory behind the optical pH sensor is the Henderson-Hasseblbalch equation, taking activity into account, $pH = pK_a + \log\frac{[A^{-1}]}{[HA^c]} + \log\frac{f_{A^{c-1}}}{f_{HA^c}}$, where pK_a is the negative logarithm of the acid dissociation constant, $[A^{-1}]$ and $[HA^c]$ are the concentrations of the basic and acidic forms of the indicator, $f_{A^{c-1}}$ and f_{HA^c} are the corresponding activity coefficients, respectively. The activity coefficient f is only close to unity in dilute solutions, which makes optical pH sensors also cross-sensitive to ionic strength.

When designing an optical pH sensor, pH indicators and matrix need to be carefully considered. Until recently, there are various fluorescent and absorption pH indicators such as 8-hydroxypyrene-1,3,6-trisulfonic acid (HPTS), fluorescein, seminaphthorhodafluors and bromocresol green, bromophenol blue, methyl red and so

on.[10] Depending on the transduction mechanism, indictors with suitable optical properties, fluorescence (excitation and emission wavelengths), absorption (absorption wavelength) and life time (life time based measurements) should match the specificity of the instruments. The pH indicator should also have an appropriate pK_a value, which should be located at the center of the pH of interest. Because the pH indicator is of the highest sensitivity around its pK_a with a dynamic range of $pK_a \pm 1.5$. Fluorescent indictors with high photostability are usually desirable for preparing fluorescent pH sensors with long stability. Sometimes, the pH indicators should have some functional groups for further modifications so that they can be covalently bonded to the matrix which can eliminate the leaching issue. The matrix should also possess different properties, depending on the applications. They should be hydrophilic enough so that protons can diffuse in and out. The matrix should have good chemical, thermal and mechanical stability. They should be inert and nonreactive with pH indicators which may interfere or even destroy their sensing ability. The matrix should also be optical transparent so that the excitation and emission light could pass through without significant signal loss. Biocompatibility should also be considered if the sensors will be applied in biological systems. Several substrates such as polyurethane,[11] poly(vinyl alcohol),[12] ethyl cellulose,[13] silicate sol gels and organically modified silicate sol gels are commonly used as matrix for pH sensor construction.[14-16]

1.2.2 pH sensor films based on silicate sol-gel

Among all the sol-gel derived materials, silica is one of the mostly studied substrates for entrapping sensing molecules to improve sensor selectivity, sensibility and stability. Silicate sol-gels have several advantages which make them excellent matrix for optical pH sensor fabrication. They have desirable properties such as high chemical and thermal stability, good mechanical stability and biocompatibility, good proton permeability, negligible swelling in aqueous and organic solutions, and excellent optical transparency. Their properties such as hydrophobicity, thickness, porosity, and stability can be tuned by controlling the fabrication conditions, the type and size of the precursors and catalysts.[17]

Sol-gel silicate films were usually fabricated by dip-coating or spin-coating pH indicators doped sol gel onto different types of precleaned substrates such as silicon and glass. The sol gel solution is usually prepared by hydrolyzing a silanol precursor such as tetraethylorthosilicate in ethanol and water using acid (HCl) as a catalyst.[18] The hydrolysis and condensation reactions are as follows:

1) Hydrolysis: $Si - OC_2H_5 + H_2O \leftrightarrow Si - OH + C_2H_5OH$

2) Alcohol condensation: $Si - OC_2H_5 + HO \leftrightarrow Si - O - + C_2H_5OH$

3) Water condensation: $Si - OH + HO - Si \leftrightarrow Si - O - Si + H_2O$

The film properties such as film thickness, pore size and stability depend on the coating speed, water to precursor ratio, solvent, precursor ratio, sol gel aging time, humidity and pH.[17] In theory, water to precursor ratio of two is sufficient for complete hydrolysis and condensation. However, the reactions generally do not go to completion due to the formation of intermediate species. In order to achieve complete hydrolysis and

condensation, a ratio of 4 to 6 is usually used to prepare films with good stability.[16] The pH of the starting solution is one of the most important parameters in the sol-gel process. The isoelectric point of silica is approximately 2. When the pH of the solution is smaller than 2, it is considered as acid catalysis. Polycondensation in low-pH conditions is similar to the polycondensation of organic polymers and yields low-surface-area materials with small pore sizes. Hence, low water to precursor ratio and low pH are usually introduced for preparing silicate films for pH sensor development. The surface polarity and pore size of the films also depend on the properties of the precursors. Sol-gel films made from TEOS are highly porous, which is due to the hydrophobility of the materials and the negatively charge silanole groups caused repulsion force inside the network. In order to increase the stability and robustness of the sensor films, organically modified sol-gels were introduced to tune the pore size and polarity of the sensor films.

pH indicators are immobilized into the silicate films via three different strategies: impregnation, covalent bonding and doping. For impregnation method, the polymer film is dipped into a concentrated indicator solution and the solvent is then evaporated. The indicator is immobilized into the polymer matrix via physical absorption, chemisorption or electrostatic interaction. This method is easy and simple. However, pH sensor films prepared via this strategy usually have short term stability due to the leaching of the indictors. For covalent bonding, the pH indicator was covalently bonded to the precursor before polymerization. This method prevents the pH indicator from leaching, however, only a few pH indicators have appropriate functional groups for covalent bonding and the functionality of the indicators may be lost due to the conjugation. Doping is the most

common way to prepare silicate pH sensor film. The pH indicator is added to the starting solution and entrapped in the matrix during the polymerization process. This method is relatively simple and straightforward. However, the long term stability of the sensor film is an issue as the pH indicator leaches out from the polymer. The overall charge of the indicators, the hydrophobicity of the matrix and their interactions (e.g. electrostatic interaction) are important factors which affect the leaching processes. Different methods have been used to prevent leaching. One strategy is using organically modified silicates, by copolymerizing inorganic alkoxides with organo(alkoxy)-silanes containing a non-hydrolysable organic functional group such as $-CH_3\ and\ -C_2H_5$. Addition of organically modified silanols can tune the microstructure (increase the hydrophobicity) and improve the stability of the indicators.[19] For instance, Butler et al. compared the leaching of pH indicators from films prepared with TEOS and methyltriethoxysilane (MTES), respectively.[20] They found that the leaching rate of the indicator at pH 8 is much slower for the MTES derived film. 80% of the indicator was leached out from the TEOS derived film after being incubated for ~27 hours in buffer 8, while only 20% of the indicator was leached out for the MTES-derived film under the same conditions. Dietmar et al. developed a miniaturized optical reflectance pH sensor based on organically modified silicate which has the potential for continuous measurements of wound pH. The sensor film was prepared by doping pH indicators (bromocreosol green and bromocresol purple) into organically modified sol gel using a combination of TEOS and (3-glycidoxypropyl) trimethoxysilane (GPTMS). The sensor is reversible and responsive to pH from 5.5 to 8.6.[20] Wencel and coworkers designed a high performance optical pH

sensor by doping HPTS ion-paired with hexadecyltrimethylammonium bromide (CTAB) into a sol gel matrix prepared from GPTMS and ethyltriethoxysilane (ETEOS).[15] The indicator was completely entrapped in the sol gel film with no leaching for one month in pH 7 buffer solutions. The sensor film has an excellent reproducibility, reversibility and stability. It is responsive to pH ranging from 5.0 to 8.0, with a response time of 12 s. They attributed the long stability of the indicator to two factors. The first one is that HPTS was ion-paired with CTAB which reduces its solubility in water. The second one is that the combination of GPTMS and ETEOS generates a dense microstructure which prevents the indicators from leaching. In this thesis, the compositions of the sol gel were varied (types of silanols and their ratios) and studied to increase the pH sensor film stability, slow down the indicator leaching and tune the response time.

1.2.3 pH nanosensors for biological applications

pH is closely regulated in different compartments of cells via ATP-dependent proton pumps (vacuolar (H^+)-ATPases), which are important for different cellular processes, such as membrane transport, acid secretion and regulation of the activity of degradative enzymes.[21] In order to measure pH in different compartments with minimal perturbation, different strategies were introduced. In the 90s, fluorescent pH indicators were directly used to monitor pH inside cells. For instance, fluorescein isothiocyanate-labeled dextran was used to measure intralysosomal pH in living macrophages.[22] The pH in the lysosomes was determined to be ~4.7 under normal conditions. Although the small size of the fluorescent molecules does not physically affect the cells, there are still some

drawbacks. First, the intracellular environment is complex, there are various proteins which may bind to the fluorescent molecules and alter their response. Second, the fluorescent molecules may be toxic to the living cells. Third, the distribution of fluorescent molecules inside cells depends on their properties and they may accumulate at certain organelles.

In order to overcome these issues, optical fiber sensors were introduced for biological applications. For instance, Tan and coworkers developed optical fiber sensors with fiber tip sizes ranging from 0.1 μm to 1 μm by immobilizing fluorescent pH indicators to silanized fiber tip via photopolymerization. These submicrometer sensors were successfully applied for intracellular and intraembryonic pH measurements.[7] Optical fiber sensors minimize most of disadvantages by entrapping the indicator dyes in a protective polymer matrix. However, these optical fiber sensors are still bulky as compared to the size of cells and especially organelles and they cause significant biological perturbations which hinders their routine applications.

1.2.4 pH nanosensors

To further minimize the size effect on biological systems, pH nanosensors were designed and successfully applied to measure intracellular pH. Among them, probes encapsulated by biologically localized embedding (PEBBLEs) and silica-encapsulated pH nanosensors are the two most common types. PEBBLEs were proposed and extensively explored by Kopelman's group.[23] PEBBLEs are prepared via reversed microemulsion polymerization.[24] The aqueous phase of the polymerization solution

consisting of fluorescent indicators, acrylamide, N,N-methylenebis(acrylamide) and PBS was added into an organic phase containing hexane and surfactants which was initialized by sodium bisulfate or ammonium persuflaate together with N,N,N',N'-tetramethylethylenediamine. By varying the ratio of aqueous phase over organic phase and the surfactants, PEBBLEs with sizes ranging from 20 to 200 nm were prepared with good batch to batch reproducibility. PEBBLEs have several advantages which make them useful in biological systems. PEBBLEs are of small size as compared to the size of cells, which induces minimum perturbations to the cells. The PEBBLE matrix protects the fluorescent indicators from interference by proteins, which permits reliable *in vivo* calibration. The PEBBLE matrix is hydrophilic which leads to fast response time. PEBBLEs are also biocompatible with negligible biological side effects. Moreover, the surface of PEBBLEs could be functionalized with specific molecules to enhance targeting. For instance, Ray et al. designed both non-targeted and F3-peptide modified PEBBLE nanosensor for intracellular pH measurement of 9L cells.[25] The nanosensors without functionalization were mostly trapped in endosomes, by contrast, nanosensors functionalized with F3 peptide were able to escape the acidic compartments and distributed in the cytoplasm. In addition, several indicators can be simultaneously incorporated to PEBBLEs which makes multiplexing sensing and referenced sensors possible. Cao and coworkers developed a ratiometric nanosensor for measuring dissolved oxygen in human plasma.[26] An oxygen-sensitive dye (platinum octaethylporphine ketone) and an oxygen-insensitive dye (octaethylphorphyrin) were both incorporated into poly(decyl methacrylate) matrix to prepare the ratiometric nanosensors. Attributed to

these advantages, PEBBLEs have been effectively delivered to into cells for intracellular analytes measurement and they are delivered via gene gun bombardment, picoinjection and liposomes. PEBBLEs were used for measuring different intracellular analytes such as pH[25], Ca^{2+}[27], Mg^{2+},[28] oxygen,[26] and glucose[29].

Silica based matrix have also been used to prepare nanosensors for different applications. Similar to PEBBLEs, dye-doped silica nanoparticles also possess several advantages as compared to the free indicators. Silica nanopartices are easy to separate via centrifugation due to the relatively high density of silica (1.96 g/cm^3). Silica nanoparticles are also hydrophilic and biocompatible and they usually disperse well in aqueous solution. The incorporation of fluorescent molecules to silica can protect the fluorescent molecules from the surrounding environment, such as protein interference and microbial attack. For instance, Xu et al. developed an oxygen nanosensor by incorporating both oxygen sensitive and insensitive fluorescent dyes into silica nanoparticles and they found that the sol-gel matrix prevents BSA from interference.[30] By contrast, the free dyes were interfered by the BSA differently which makes the calibration curve unreliable. Tan's group also discovered that the silica network can improve the photostability of fluorescent molecules as compared to free dyes.[31] They found that there was no noticeable photobleaching for dye-doped silica nanoparticles when they were continuously illuminated for 1 h, whereas 85% of the initial signal was lost for the free dye molecules under identical conditions. In addition, many fluorescent indicators could be incorporated to the silica nanoparticles, hence, silica encapsulated fluorescent nanoparticles are very bright and they are excellent fluorescent probes for

biolabeling. It was estimated that more than 10,000 dye molecuelse can be doped inside a 60 nm nanoparticle. Attributed to these good properties, fluorescent dyes doped silica nanoparticles have had diverse biological applications.

Silica nanoparticles are generally prepared by reverse microemulsion and sol-gel methods. For the reverse microemulsion (water-in-oil) method, aqueous droplets were confined within surfactant controlled micelles and dispersed in a non-polar solvent to generate monodispersed spherical droplets. These nanoparticle syntheses were first extensively studied by Arriagada and Osseo-Asare in the 1990s and they were then extensively studied by Tan and coworkers for developing fluorescent nanoparticles in the mid-1990s.[32] In general, the water droplets with hydrophilic indicators are stabilized by a surfactant (e.g. Triton X-100) and a cosurfactant (e.g. hexylalcohol), and dispersed in a nonpolar organic solvent (e.g. cyclohexane). A small amount of ammonia hydroxide is used as a catalyst. The decomposition and nucleation of the silica are highly confined in the water droplets and the dyes are physically entrapped in the silica networks, generating highly monodispersed dye-doped silica nanoparticles. The size of the nanoparticles can be controlled by varying the water to surfactant ratio.[33]

Alternatively, dye-doped silica nanoparticles can also be synthesized via Stöber method, which was first studied by Stöber in 1968 to prepare monodispersed silica spheres.[34] This method was later modified to prepare dye-doped silica nanoparticles. In a typical reaction, a silica alkoxide precursor (e.g. TEOS) is hydrolyzed in a mixture of ethanol, dye molecules and water, using ammonia hydroxide as a catalyst. The hydrolysis of TEOS produces silicic acid and then undergoes a condensation process (forming Si-O-

Si bonds) to generate amorphous silica particles. By controlling the amount of precursors and the reaction time, monodispersed nanoparticles with diameters between 50 nm and 2 μm could be prepared.[34] The dye leaching could be avoided by covalently conjugating the dyes to a functional silane (e.g. APTES) agent and then cohydrolyze together with TEOS to form dye-doped silica nanoparticles without leaching. In addition, silica alkoxide precursors containing functional groups such as carboxylic acid groups (e.g. carboxyethylsilanetriol) and amine groups (e.g. APTES) could be subsequently coated onto the surface of dye-doped silica nanoparticles, which facilitates further bioconjugation such as protein (antibody) and folic acid conjugation.[31]

Dye-doped silica nanoparticles were introduced for different applications in bioimaging and bioanalysis.[35-36] Dye-doped silica nanoparticles can be used a signaling element in an immunoassay by conjugating them with an antibody which is specific to different targets such as proteins, cells and bacteria. By labeling Rubby-doped silica nanoparticles with a mouse antihuman CD10 antibody which has a high affinity to leukemia cell, Santra et al. successfully identified the leukemia cell using an optical imaging technique.[31] He et al. used similar strategy to distinguish liver cancer cells from other cells in a mixed sample by conjugating antihuman liver cancer monoclonal antibody HAb18 onto the surface of FTIC-doped silica nanoparticles.[37] Silica nanoparticles exhibit multiple colors were designed by Wang and coworkers.[38] By incorporating different amounts of three tandem organic dyes into a single nanoparticle, nanoparticles with multiple colors were prepared under a single wavelength excitation due to the different degree of fluorescent resonance energy transfer (FRET). These

multiple colored silica nanoparticles can be used as barcoding tags for multiplexed detection. By functionalizing these dye-doped silica nanoparticles with monoclonal antibodies specific for pathogenic bacteria species, they developed a sensitive method for detecting *Escherichia coli*, *Salmonella typhimurium* and *Staphylococcus aureus* simultaneously.[39] Wang et al. also have synthesized dual-luminophore-doped silica nanoparticles for detection of bacteria in a flow system. [40] Dye-doped silica nanoparticles have also been used as labels for bioanalysis to increase sensitivity and throughput. Zhao et al. have developed a sandwich-assay for DNA detection using dye-doped silica nanoparticles as signal reporters. [41] In specific, the unlabeled target sequence was first captured by the capturing DNA immobilized on a glass surface, and then hybridized with the probe sequence which was functionalized with tetramethylrhodamine (TMR)-doped nanoparticles.[41] With this method, detection limit of 50 fM was achieved which is 20 times lower than the conventional single phycoerythrin labeling method. Some other affinity molecules such as folic acid, peptides and aptamers are also conjugated to the surface of dye-doped silica nanoparticles for labeling different targets (e.g. cancer cells).[42] In addition, Santra et al. have successfully introduced TAT (a cell penetrating peptide) functionalized FITC-doped silica nanoparticles for labeling lung cancer cells in vitro and rat brain tissue in vivo. [43] However, the in vivo images were blurred. Hence, introducing the short wavelength excited dyes-doped silica nanoparticles for bioimaging in deep tissue is hindered due to the low penetration depth of the excitation source and emission signal, together with the autofluorescence background.

1.2.5 In vivo pH measurement methods

pH is a very critical parameter in biological systems. Monitoring pH variation of biological systems in situ (in tissue or through tissue) can provide important information for understanding physiological processes. For instance, tissue pH is an important physiological parameter that indicates both blood flow and cell metabolic state. It is well accepted extracellular tumor pH is more acidic than normal tissue, primarily due to the poorly organized vasculature which causes slow flow and poor tissue oxygenation. This situation causes anaerobic glycolysis producing lactic acid which is inefficiently removed. Low environmental pH has been shown to inhibit cell proliferation, survival and activity. Low pH has even been implicated in the induction of metastases.[44] Detecting and imaging pH *in vivo* is essential to biomedical field but challenging. Until recently, several techniques have been introduced to measure pH in tissue or through tissue.

Potentiometric microelectrode was first employed to measure tissue pH, however, it is invasive and requires bulky accessories such as battery which hinders long-term measurements.[45]

Magnetic resonance (MR) spectroscopy imaging has also been introduced to non-invasively measure tissue pH in vivo, based on endogeneous or exogenous agents. It measures tissue pH based on pH-dependent changes in chemical shift of the agents. Using ^{31}P MR spectroscopy, endogeneous inorganic phosphate can reflect the intracellular pH when the extracellular space is <55% as the intracellular concentration (2-3 mM) is higher as compared to extracellular concentration (1 mM). In order to

improve sensitivity, exogenous reagents are usually introduced. For instance, pH-sensitive molecules with ^{19}F and ^{1}H resonances were introduced to measure intra or extracellular tissue pH in vivo based on MR spectroscopy. MR based methods are capable of imaging pH with 1-2 mm resolution. However, there are still some intrinsic disadvantages. First, the sensitivity of MR spectroscopy is relative low which requires a large concentration of reagents for measurement. Second, very few of pH sensitive probes have large chemical shift. In addition, the accuracy of pH measurement relies on the distribution of the probes within the tissue. The presence of metallic substrates (e.g. metallic implant) may create artifact and interfere the analysis. Radioactive-labeled molecules such as ($^{11}CO_2$, carbon-11-labeled dimethyloxazolidinedione) were also used to measure brain pH via positron emission tomography. [46-47] However, this technique has a safety concern and the reliability of the measurement is closely related to the distribution of the radioactive-labeled molecules.

Schreml et al. developed a luminescent pH sensor film based on time-domain dual lifetime referencing method for imaging 2D pH in vivo.[48] The sensor was prepared by covalently attaching FITC to aminocellulose microparticles and incorporating ruthenium (II) tris-(4,7-diphenyl-1,10-phenanthroline) ($Ru(dpp)_3$) into polyacrylonitrile microparticles. Then, these two types of particles were embedded in polyurethane hydrogel and spread onto a transparent PVdC foil to form sensor foils. The pH sensitive indicator FTIC has a short lifetime (<5 ns), whereas the pH insensitive indicator $Ru(dpp)_3$ has a long life time of ~6 μs. pH calibration curve was generated by taking the ratio of luminescent intensity with the LED on (460 nm excitation wavelength) over the

luminescent intensity with LED off. These sensor foils were applied to image pH variation of the skin-graft donor sites (~400 μm) during cutaneous wound healing with good spatial resolution. It was found that pH continuously decreased during physiological healing, while heterogeneous pH was revealed in chronic wound healing which indicates inflammatory phase. Later, Wolfbeis group designed a sensor film to measure oxygen and pH simultaneously on the skin surface in vivo.[49] The sensor film design is very similar to Schreml's sensor film except that they incorporated both an oxygen-sensitive indictor and a pH indicator to different microparticles. A real-color RGB image of the sensor film was recorded and analyzed to visualize the spatial distribution of pH and pO_2. By depositing the sensor foils on the wound surfaces, high pH values and low oxygen were simultaneously visualized on the chronic wound. However, due to the autofluorescence background and tissue absorption and scattering effect, the ability of the sensor foils to image pH in deep tissue is limited. In addition, the spatial resolution is also limited by the tissue thickness as the senor foil embeds deeper in the tissue. In our dissertation, we developed two different techniques to monitor bacterial growth caused pH variation on the sensor film surface embedded in thick tissue (6 mm) using a combination of pH sensitive indicators and upconverting particles/radioluminescent particles.

1.3 Surface-enhanced Raman spectroscopy

1.3.1 Raman spectroscopy

The principal of inelastic light scattering was first theoretically predicted by Smekal in 1923.[50] In 1928, Raman and Krishnan first experimentally observed this phenomenon by analyzing the scattered light from several liquids.[51] This inelastic scattering effect is known as Raman scattering. Raman scattering occurs due to the inelastic collision of photons with molecules. The photons may lose or gain energy from the molecules. This change in the photon energy generates a change in frequency, according to this equation: $\Delta\nu=\Delta E/h$. The frequency of the scattered photons is shifted relative the excitation photons as shown in the scheme in Figure 1.1.[52] The scattered photons can have a lower energy (Stokes shift: $h\nu_S = h\nu_L - h\nu_M$, $h\nu_S$ is the energy of the Stokes shift scattering, $h\nu_L$ is the energy of the excitation light, $h\nu_M$ is energy between the two adjacent vibration states.) if the photons interact with a molecule in its vibrational ground state or a higher energy (anti-Stokes shift: $h\nu_{aS} = h\nu_L + h\nu_M$, $h\nu_{aS}$ is the energy of the anti-Stokes shift scattering) if the photons interact with a molecule in its vibrational excited state as shown in Figure 1.1. The intensity ratio of anti-Stokes shift over that of Stokes shift is determined by the Boltzmann distribution.

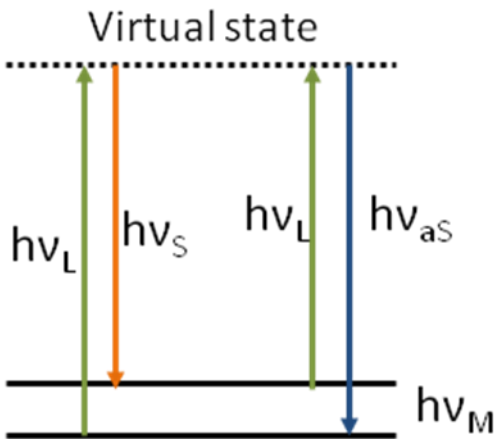

Figure 1.1 Schematic representation of energy transitions in Raman spectroscopy.

Ever since its discovery, Raman spectroscopy has been widely used to obtain vibrational information about molecular structure of different samples. Although Raman spectroscopy and infrared spectroscopy are both used to obtain vibrational information from molecules, Raman spectroscopy has several advantages. First, water has a very weak Raman signal so Raman spectroscopy can be introduced to analyze samples under ambient conditions in almost every environment. Second, the production of Raman signal is due to the changes in molecular polarizability as the molecular vibrations displace the constituent atoms from their equilibrium positions. Hence, molecules are all Raman active. Third, there is minimal sample preparation for Raman analysis. This technique is noninvasive and can be used for remote detection. The advent of lasers with monochromatic photons at high flux, the advancement in low noise, high quantum efficiency multichannel detectors (CCD arrays), together with the emergence of notch filters has led to the development of high-sensitivity Raman spectrometer.[53] Raman

spectroscopy has been used to analyze various samples. For instance, Raman spectroscopy is widely used for identifying potentially hazardous or illegal substances in the homeland security and defense arenas.[54] Day and coworkers used Raman spectroscopy to detect five drugs of abuse (codeine, phosphate, cocaine hydrochloride, amphetamine sulphate, barbital and nitrazepam) in latent fingerprints.[55] Raman spectroscopy has also been used to analyze pharmaceuticals. As a noninvasive and nondestructive technique, Fourier transform Raman spectroscopy has been applied to detect pigments and small artifacts and gemstones in paintings.[56-57] Despite all these advantages of Raman spectroscopy, it is considered to be more useful for structural analysis than for ultrasensitive detection. One of factors limits the even wide applications of Raman spectroscopy is that the Raman signal is very weak for most molecules. This is due to the small cross section of Raman scattering. The cross section for Raman scattering is usually in the range from 10^{-29} to 10^{-31} cm^2, which is about 14 orders of magnitude smaller than the cross section of fluorescence (~10^{-16} cm^2). This small scattering cross section greatly limits the sensitivity of this technique and also brings more challenges to the instrumentation such as the intensity of lasers and the optical collection efficiency of the setup.

1.3.2 The discovery and development of Surface-enhanced Raman spectroscopy

In 1974, Fleischmann and coworkers observed intense Raman signal from pyrindine adsorbed onto an electrochemically roughened silver electrode surface from aqueous solutions, which they attributed this increase in signal to the increase in the surface area.[58]

It was that until 1977 that Jeanmaire and Van Duyne, Albrecht and Creighton independently recognized that only a small fraction of the increased intensity could be accounted by the increase in the surface area (the increase in the number of adsorbed molecules) and proposed that there was an enhancement of the scattered intensity in the adsorbed state.[59-60] This enhanced scattering process is known as surface-enhanced Raman scattering (SERS). In general, two enhancement mechanisms are introduced to explain the enhancement. The first one is electromagnetic enhancement. It is generated when the localized surface plasmon resonance of a metallic substrate (usually silver, gold or copper) is excited by a light near or in the visible region. When the Raman scatter process is subjected to the intensified electromagnetic field, the magnitude of the induced dipole increases, hence the intensity of the inelastic scattering also increases. The other one is due to the chemical enhancement effect. This effect is associated with an electronic coupling between the molecule and metal, which increases the Raman cross section and leads to more efficient scattering process. In combination with these two types of enhancement mechanisms, typical enhancement factors of 10^5-10^8 have been reported, and factors as high as 10^{11} to 10^{12} for single dye molecule was also demonstrated.[61] SERS has overcome the low sensitivity problem of Raman spectroscopy and become an attractive tool in the field of biophysics and biochemistry due to its ability to provide structural information and high sensitivity.

As compared to fluorescence, SERS has several advantages. Firstly, SERS can provide unique molecular structure information of the sample, it can function as a molecular fingerprint; Second, SERS is commonly excited with visible or near visible

light which can be tuned to function in the tissue transparent window. Thirdly, SERS has a very small line width (For example, Aggarwal et al. measured the Raman line widths of benzenethiol assembled on the surface of silver film over nanosphere substrate using a 785 nm Ti: Sapphire laser as the excitation source. The fwhm of the Raman line at 1001 cm^{-1} is ~3 cm^{-1}, corresponding a fwhm widths of ~0.3 nm.[62]) which allows multiplexing measurements whereas the full wavelength at the half maximum for fluorescence is around 50 nm. Last but not least, with the introduction of metallic nanostructures, SERS has overcome the fluorescence interference of Raman spectroscopy and it is a very surface-sensitive technique. Since its discovery, different aspects of SERS have been greatly investigated.

Chemical sensors and biosensors based on SERS have been used to detect a wide variety of analytes.[63-66] Here, pH sensors based on SERS will be briefly summarized. Bukowska's group introduced SERS to study the effect of concentrations and the pH of the solutions on the orientation of 4-mercaptobenzoic acid (4-MBA) on silver and gold substrates.[67] They observed that the SERS spectrum of 4-MBA monolayer on the Au surface has a relatively intense band at 1370 cm^{-1} at alkaline pH (pH 10), corresponding to ν_s (COO^-). This peak varnished at acidic pH (pH 1). Similar changes were also seen from 4-MBA molecules on the silver surface. However, the pH sensitivity of this 4-MAB functionalized metallic surface was not discussed. Talley and coworkers designed a nanoscale pH sensor based on 4-MBA functionalized silver nanoparticles (clusters). The peak at 1430 cm^{-1} is attributed to the COO^- stretching mode, which is pH dependent. The peak at 1590 cm^{-1} mode is corresponding to the ring-breathing mode and it is pH

independent. Ratiometric pH nanosensors were designed by taking the ratio of these two peaks. The pH nanosensor is responsive to pH in the range of 6 to 8. The robustness of the pH nanosensor was tested by incorporating these nanosensors into living Chinese hamster ovary cells. However, the resolution of the nanosensor is ~1 pH unit and they attributed this variation to differences of the electrical double layer surrounding the nanoparticle cluster as SERS spectra were only obtained from aggregated particle clusters. Thereafter, various pH nanosensors based on SERS were designed with different strategies. For instance, Halas' group designed a standalone, all optical nanoscale pH meter by absorbing 4-MBA molecules onto Au nanoshell surface.[68] Their pH nanometer has an accuracy of 0.1 pH units throughout the working range of 5.8 to 7.6 with a satisfactory reversibility. However, their pH nanometers were covalently coated onto the silicon wafer surface which prevents their applications in measuring pH in biological systems on a microscopical scale. pH nanosensors based on 4-MBA functionalized silver nanoparticles with improved performance (better sensitivity) were constructed by different research groups for studying endosomal pH variation in living cells.[69-70] Different pH sensitive SERS reporters such as 2-aminothiophenol, 3-amino-

5-mercapto-1,2,4-triazole and 4-mercaptopyridine, were also introduced for pH nanosensor design.[71-73] Despite all these development, there is still more room for improvement. The most important one is the stability of these nanosensors. The nanosensors tend to aggregate randomly when they are introduced to different samples. The different degrees of aggregation create different "hot spots" which may jeopardize the pH measurements. The other issue is that the nonspecific interaction of the

surrounding molecules (especially large biological molecules) with the SERS reporters. This nonspecific interaction may affect the dissociation of the reporters, hence, influencing the accuracy of pH measurement in a complex environment. In this thesis, we designed a pH nanosensor based on SERS with high sensitivity and specificity by encapsulating 4-MBA functionalized silver nanoparticles with a thin layer of proton permeable silica shell.

SERS nanotags have also been used for a variety of applications especially for detecting analytes of interest in biological systems. SERS nanotags are created by labeling Raman reporters onto the surface of silver or gold nanoparticles.[74] In order to guarantee the signal stability and reproducibility, a protective layer or shell (silica shell, polymers or protein layer) is usually added. A specific recognition unit for the target of interest is also usually covalently bonded to the surface of SERS nanotags to increase specificity. One of the advantages of SERS nanotags as compared to fluorescent nanotags is that their spectral width is very small. Hence, it is capable of multiplexing detection. For instance, SERS nanotags have been used to determine the concentration of cardiac troponin I, C-reactive protein and myoglobin based on a single-line lateral flow immunoassay.[75] Multiplexing Raman signal was simultaneously obtained at a xenograft tumor site in living mouse by tail vein injecting three near infrared SERS nanotags.[76] Very recently, Dinish and coworkers successfully detected three intrinsic cancer biomarkers in a breast cancer model using three antibody-conjugated SERS nanotags.[77] The antibody-conjugated nanotags exhibited maximum signal at 6 hours while the nanotags without antibody conjugation showed no detectable signal after 6 hours. This

study demonstrated the potential of using SERS nanotags in monitoring tumor progression and therapy efficacy.

SERS has also been introduced to sense glucose concentration in vivo. Stuart and coworkers presented the first in vivo application of SERS for measuring glucose concentration. By subcutaneously implanting a substrate with silver over nanospheres self-assembled with monolayers of decanethiol and 6-mercapto-1hexanol to rats, the glucose concentration was measured in vivo with SERS, and the performance of their sensor was compared with a standard glucose meter at the same time. The performance of the vivo glucose was satisfactory.[78]

Another important development of SERS is called surface-enhanced spatially offset Raman spectroscopy (SESORS), which is a combination of SERS and spatially offset Raman spectroscopy (SORS). SORS spectra are collected at a location which is spatially offset from the excitation laser and it allows Raman signal to be collected through distinctly different layers within a diffusely scattering medium.[79-81] With SESORS, Stone and coworkers demonstrated that Raman signals can be noninvasively obtained from SERS nanoparticles embedded in 50 mm thick porcine tissue.[82] Later on, the same group imaged the distribution of biphosphonate-functionalized SERS nanotags on the bone surface through 20 mm porcine tissue, which demonstrated the great potential of SESORS for in vivo bisphosphaonate tracking.[83] Very recently, Van Duyne' group demonstrated the ability of SESORS to measure spectra through various thickness of bone (3-8 mm) with SERS nanotags.[84] This demonstration shows SESORS has the great potential to noninvasively image neurochemical distribution in the brain in vivo.

SESORS will become a very powerful technique to noninvasively obtain molecular information in biological systems in vivo, however, the spatial resolution of this technique is intrinsically limited by the light diffusion through tissue.

1.4 Upconverting nanoparticles

1.4.1 Upconversion mechanism

Upconversion is the process related to the emission of high energy light (shorter wavelength in the visible range) following the excitation of certain luminophores (doped) with a lower energy light (near Infrared). This process usually occurs in rare-earth doped solids. There are three mechanisms associated with this process known as excited state absorption (ESA), energy transfer upconversion (ETU) and photon avalanche (PA).[85] ESA as shown in Figure 1.2A is a process of sequential absorption of two or more resonant photons. The first photon absorption excites the ion to a metastable and long-lived level E1 and the absorption of second photon promotes the ion from E1 level to E2 level, where the emission from E2 to ground state (G) occurs. ETU process as shown in Figure 1.2B is the energy transfer between the two adjacent ions at E1 level, which leads the donor ion relaxes to the ground state and acceptor ion excited to the E2 level, accompanied by the emission process E2→G. PA as shown in Figure 1.2C is the most efficient process but could only occur when the pump density reaches a certain threshold and this process is power dependent. The sensitizing ion is first promoted to excited level 2 (E2) via ESA. This excited ion can interact with another neighboring ion in the ground

state to produce two ions in the intermediate level (E1) via cross relaxation. Then these two ions can then produce four, then eight and 2^n (n, the number of process). Hence, there is a reservoir of ions at the intermediate level and an avalanche of ion population in excited level 2 can be established, which leads to efficient luminescence emission.

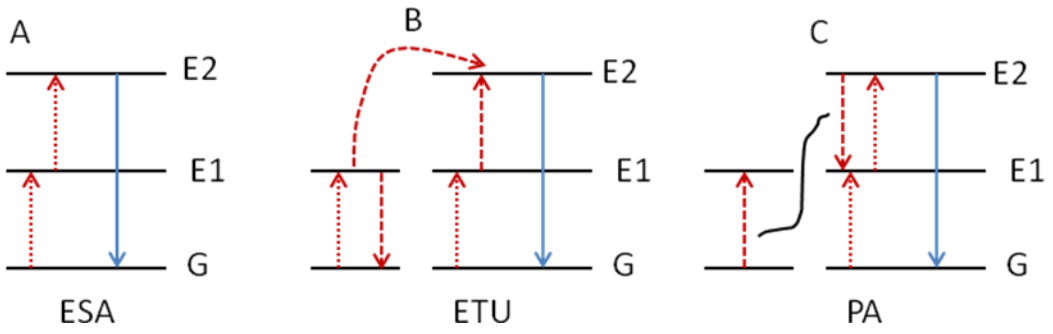

Figure 1.2 Schematic representation of the three processes causing upconversion in rare earth doped solids. A. Excited state absorption; B. Energy transfer upconversion. C. Photon avalanche. Dotted line: photon excitation, dashed line: non-radiative energy transfer, full arrow: emissive processes.

Since its discovery, upconversion process has been exclusively observed and studied in rare-earth-doped phosphors. For instance, Downing et al. designed a three-color, solid-state, volumetric display with rare-earth-doped heavy metal fluoride glass.[86] Upconversion has also been used as photon detectors and lasers.[87-88] In 2003, Heer et al. first observed photon-upconversion in transparent colloids, the emission of blue, green, and red light from Yb^{3+}/Tm^{3+} and Yb^{3+}/ Er^{3+} doped lanthanide phosphate nanoparticles when they were excited with near IR laser.[89] This discovery led to extensive research in upconverting nanoparticles from synthesis, surface modification to applications.

Upconverting nanoparticles (UCNPs) are generally prepared by doping sensitizer and activator into an inorganic host material. Sensitizer should be effectively excited by the excitation laser and efficiently transfer the energy to the activators which emit luminescence. Yb^{3+} ion, with a simple energy scheme and a large cross section in the near infrared region, is usually used as a sensitizer. Rare earth ions such as Er^{3+}, Tm^{3+} and Ho^{3+} have ladder pattern energy levels and are frequently used as upconverting activators. Various materials such as fluorides, oxides, heavy halides, oxysulfide, phosphates and vanadates are used as host substrates for preparing UCNPs. Fluorides are the most common host materials due to their low photon energies, good chemical stability and biocompatibility.

As compared to other anti-Stokes process such as simultaneous two-photon absorption and second harmonic generation, upconversion is an efficient process which can emit shorter wavelength light at relatively low excitation power. For instance, the two-photon-absorption process requires the simultaneous absorption of two photons which usually requires a high-density pulse laser with a power density of 10^6 to 10^9 W/cm^2, while upconversion process can easily occur at a power density of 1 to 10^3 W/cm^2. This low power density permits the use of low cost and compact laser devices.

Different synthetic routes such as hydrothermal synthesis,[90] coprecipitation,[91] thermal decomposition,[92-93] combustion[94] and microwave assisted synthesis[95] have been used to synthesize UCNPs of different sizes and different surface ligands. However, UCNPs synthesized with these methods usually have hydrophobic ligands on the surface which make them have poor stability in aqueous solution and hard to conjugate with recognition

molecules. Hence, post-synthesis surface modifications are usually needed to make the UCNPs have good stability in aqueous solution and facilitate further bioconjugatons. Ligand exchange,[96] ligand oxidataion[97] layer-by-layer assembly[98] and silica encapsulation[99-101] all have been introduced to make the surface of UCNPs hydrophilic and versatile for further bioconjugation.

As compared to common imaging probes such organic dyes and quantum dots, UCNPs have distinct advantages which make them excellent labels for biological applications. UCNPs can be excited with near infrared light which allows high tissue penetration depth and negligible autofluorescence background. For instance, Tm^{3+} doped UCNPs which have emission in the near infrared region were used for small animal imaging.[102] UCNPs also have high photostability. It has been shown that there was no luminescence intensity fluctuation when the UCNPs were continuously illuminated for hours.[103] Nam et al. continuously tracked (imaged) the movement of PEG-posholipids functionalized NaYF4: Er^{3+}, Yb^{3+} UCPs in living HeLa cells at a single vesicle level in real time for more than six hours.[104] By using NIR exciation, there was no autofluorescence or photoinduced damage. Organic dyes usually have low photostability which limits their applications in long term tracking. Quantum dots also have high photostability, however, their intermittent emission limits their use for labeling individual biological molecules. Attributed to the shielding effect from the completely filled $5s^2$ and $5p^6$ orbitals, UCNPs usually have narrow emission bands with fwhm of 10-20 nm with narrower fine structure of ~ 0.5 nm, which allows multiplexing labeling and detection.[105-106] However, organic dyes usually have broad absorption and emission spectra which

limit multiplexing. Quantum dots also have relatively narrow emission bands, with an fwhm of about 30-50 nm. UCNPs also have long lifetime as long as 0.1 ms due to the fact that f-f electron transitions are Laporte-forbidden, this long lifetime allows the use of time-resolved luminescence detection technique to avoid the interference from the undesired short-lived background fluorescence, which can greatly improve detection sensitivity and signal-to-noise ratios. The materials used in UCNPs possess high biocompatibility, while organic dyes and especially quantum dots contain toxic materials which bring concerns. These excellent properties of UCNPs make them widely used for bioimaging and sensing. The use of UCNPs as biolabeling and bioimaging, therapeutic and analyte detection tools will be discussed.

1.4.2 UCNPs as biolabels

UCNPs, excited by near infrared light source, are extensively used as labels for cell imaging and small animal imaging. Non-functionalized water soluble $NaYF_4$: Er^{3+}, Yb^{3+} For instance, the dynamic distribution of UCNPs inside Hela cells was studied using upconversion luminescence.[107] Lim et al. used UCNPs with sizes between 50 and 200 nm to visualize the digestive system of live C. elegans.[108] I*n vivo* imaging of UCNPs in small animals was first reported by Chatterjee and coworkers.[109] Visible luminescence was observed from the nanoparticles deeply injected in the rat body (up to 10 mm) when exposed to a 980 nm near infrared laser. Multi-color UCNPs functionalized with hydrophilic polymers were used to map lymph node in vivo via upconversion luminescence imaging.[110] The sensitivity of upconversion imaging was at least one order

of magnitude lower than quantum dot-based fluorescence imaging, which showed the great potential of upconversion imaging as a highly sensitive multiplexed biomedical imaging technique. By introducing a pinhole to a laser scanning up-conversion luminescence microscopy, Yu and coworkers successfully eliminated the interference of out-of-focus upconverting luminescence which improves the image resolution. Prasad and coworkers used Tm^{3+} and Yb^{3+} doped fluoride nanophosphors for in vivo cell and mouse imaging.[102] NIR luminescence with high signal to noise was obtained from both cells and mouse. Targeted imaging of specific cells (cancer cells) or tumors can be achieved by functionalizing UCNPs with specific recognition elements such as folic acid, antibody and peptides. For instance, Wang et al. used antibody conjugated UCNPs as a luminescent biolabels for the detection of a cancer biomarker carcinoembryonic antigen.[111] The nanoparticles were synthesized using a solvothermal method and then coated with a thin layer of SiO_2 via Stöber method, which were further modified with amine groups for the bioconjugation of anti-CEA8 antibodies. The functionalized UCNPs were successfully used to detect Hela cells with high specificity. Xiong et al. conjugated folic acid to the amine functionalized UCNPs and the resultant UCNPs have been used to target folate-receptor overexpressed Hela cells in vitro and Hela tumor in vivo using in vivo up-conversion luminescence imaging.[112] Yu and coworkers used neurotoxin-conjugated UCNPs for direct visualization of tumors in nude mice using laser scanning upconversion fluorescence microscopy.[113] The polyethylenimine-coated $NaYF_4$: Yb, Er/Ce nanoparticles were synthesized using hydrothermal method and then functionalized with recombinant chlorotoxin, a typical peptide neurotoxin that can bind to many types of

cancer cells with high specificity. The nanoprobes were demonstrated to have good biocompatibility and they selectively accumulated at the xenograft glioma tumor site. Functionalized UCNPs have also been used for targeted drug delivery. Silica encapsulated UCNPs functionalized with folic acid and siRNA were used for imaging and targeted delivery of small interfering RNA to cancer cells.[114] The successful delivery of siRNA was confirmed with a luciferase assay.

1.4.3 UCNPs as photodynamic therapy probes

UCNPs were also widely used as light source for developing photodynamic therapy probes. For instance, Zhang and coworkers designed a photodynamic therapy probe by loading a photosensitizer to silica encapsulated UCNPs.[115] An antibody, which can specifically bind to antigens expressed by the target cell, was covalently attached to the surface the silica-coated nanoparticles. The ability to kill target cells was confirmed. Qian et al. incorporated photosensitizer (Zinc phthalocyanine) into mesoporous silica encapsulated UCNPs for photodynamic therapy.[116] It was demonstrated that singlet oxygen was released when the functionalized nanoparticles were excited by a NIR laser. Idris et al. also designed a photodynamic therapy probe, using mesoporous-silica-encapsulated UCNPs as a nanotransducer to convert near infrared light to visible wavelengths and a carrier for photosensitizers.[117] UCNPs with a multicolor emission were used to activate two photosensitizers simultaneously. It was demonstrated that their design have a higher PDT efficacy as compared to a single photosensitizer loaded PDT probe. Their probes were successfully used to inhibit the tumor growth in a mice model.

1.4.4 UCNPs as sensors based on FRET

In 2005, Li et al. developed an avidin nanosensor based on FRET using biotinylated $NaYF_4$: Yb/Er UCNPs (diameter ~50 nm) as energy donors and biotinylated gold nanoparticles as energy acceptors.[98] The presence of avidin brings these two types of nanoparticles close enough to generate efficient energy transfer. The concentration of avidin is correlated to the energy transfer induced upconverting luminescence luminescence. Later on, this strategy has been used to design various chemical and biosensors for measuring different analytes of interest such as metal ions[118-119], biological molecules[120] and other small molecules[121-122]. For instance, Zhang et. al designed a nucleotide sensor based on FRET between UCNPs and fluorophore (carboxytetramethylrhodamine).[123] The two capture oligonucleotides were labeled with UCNPs and the fluorophore, respectively. The hybridization of target DNA between the two capture oligonucleotides brings the UCNPs and fluorophore in close proximity which leads to efficient energy transfer. Based on this strategy, they were able to detect perfectly matched target DNA with a detection limit of 1.3 nm and they were also able to distinguish target DNA from DNA with a single nucleotide variation. An oxygen sensor was designed by incorporating Ru(II) complex to the surface of $NaYF_4$:Yb^{3+},Tm^{3+} nanoparticles.[124] The blue emission from the UCNPs can excite the Ru (II) complex, which can be quenched by oxygen in a concentration dependent manner. A glutathione sensor based on a combination of lanthanide-doped UCNPs and manganese dioxide nanosheets was also developed and introduced to measure intracellular glutathione

concentration.[125] Manganese dioxide nanosheets were directly grown onto the surface of UCNPs with the addition of $KMnO_4$ in the presence of 2-(N-morpholino) ethanesulfonic acid buffer. This manganese dioxide sheets effectively quench the luminescence of UCNPs. Glutathione sensor is constructed by measuring the luminescence recovering caused by the addition of glutathione which reduces MnO_2 to Mn^{2+}.

1.4.5 UCNPs chemical sensors based on inner filter effect

Using UCNPs and chemical indicators, different chemical sensors have been designed based on inner filter effect. These sensors were primarily done by Wolfbeis' group. In 2009, their group designed the first optical pH sensor based on upconverting luminescent lanthanide nanorods and pH indicators.[126] $NaYF_4$: Er^{3+}, Yb^{3+} nanorods together with bromothymol blue (BTB) were incorporated into a biocompatible polyurethane hydrogel. A film was formed by spreading the cocktail onto an optically transparent polyester support. BTB has distinct absorption spectra at different pH values, which modulate the luminescence spectrum of the upconverting nanorods in a pH dependent way. In specific, the acidic form of BTB has a yellow color which has a larger absorption at green emission of the nanorods, while the basic form of BTB has a blue color which has a larger absorption at the red emission of the nanorods. The pH sensitivity of the film was shown by measuring the luminescence intensity at 548 nm (green) and 658 nm (red), respectively. Later, the same group also developed carbon dioxide and ammonia sensor films based on the same principle but slightly different substrates. For instance, a carbon dioxide sensor was constructed by incorporating NaYF4:Yb, Er nanoparticles, pH probe

BTB and tetrabutylammonium cation into a gas permeable polystyrene film.[127] By either taking the peak intensity at 542 nm or 657 nm, the sensor film is responsive to 1-3% CO_2 with a calculated detection limit of 0.11 %. Ammonia sensor films were constructed by immobilizing NaYF4:Yb, Er and phenol red into a polystyrene matrix.[128] Phenol red at its base form (pink) has a larger inner filter effect on the green emission of the nanoparticles while its acidic form (yellow) has negligible effect on the emission of the UCNPs. In contrast, the red emission of the nanoparticles is not affected by the filter effect from the phenol red at any pH. By taking the ratio of the green intensity over the red intensity of the UCNPs, an ammonia sensor film is designed. This is a big improvement as compared to their previous sensor films for pH and carbon dioxide as the performance of this ratiometric sensor film is not affected by the inhomogeneities of the sensor membrane, the concentration of the UCNPs, and the fluctuations of the laser intensity. The sensor is sensitive to 1 to 20 mM aqueous solutions of ammonia with a detection limit of 400 μM. Ever since then, this strategy was used to construct different chemical or biosensors based on upconverting nanoparticles and chemical indicators. For instance, by assembling a mercury sensitive dye (chromophoric ruthenium complex) to nanophosphors, a mercury ion sensor was constructed for sensing and imaging the distribution of mercury ions in cells.[118] The resultant luminescence spectrum changes with the concentration of mercury ions because the binding of mercury ions to the dye complex changes its absorption spectrum. This strategy works well in vitro where the green and red emissions of the UCNPs have the same power dependence.

However, upconversion process is a nonlinear process and its emission spectrum is related to the power of the excitation source. Suyver et al studied the power dependence of sensitized upconversion luminescence both theoretically and experimentally.[129] As in consistent with the theoretical model, it is shown that the power dependence of the upconversion emission from a state that needs n energy transfer steps is P^n (P is the excitation power) at low power limit (<60 W/cm^2). However, this power dependence decreases to P^1 at high-power limit, regardless of the actual number of energy transfer steps. Wang et al. studied the power density effect on the upconversion luminescence of β-$NaYF_4$: Yb^{3+}, Er^{3+} and they found that the intensity ratio of red over green is close to 1 when the excitation power density is low (<150 W/cm^2), however, this ratio increases significantly as the power density increases.[130] They attributed this effect to the existence of an intermediate level with nonradiative relaxation channels which affect the emission process in a power dependent way. The different power density effect on the intensity of green and red was also seen in other host materials doped with other rare earth ions.[131-132] Hence, the fluctuation in the excitation power may cause the ratios of the green emission over red emission to change which may affect the accuracy of measurements. In addition, tissue is composed of water, oxygenated hemoglobin, deoxygenated hemoglobin, intralipids and other particles which absorb and scatter different components of light differently. It is well characterized that tissue has a larger absorption and scattering effect on the visible spectrum as compared to the near infrared light. Even within the visible spectrum, tissue absorbs and scatters differently at different wavelengths, with a larger absorption and scattering effect on green light as compared to red light.[133] For instance,

the intensity ratios of green light over red light changes from 0.77 to almost zero as the injection depth of upconverting nanorods in a mouse leg varies from 2.5 mm to 10 mm.[134] Hence, when sensors constructed based on the intensity ratio of green over red are imbedded into tissue, the intensity ratios of green over red will be different regardless of the analyte concentrations. In order to overcome this issue, we designed a pH sensor film based on the inner filter effect between two closely spaced red emission peaks of the UCPs and the pH indicator (bromocresol green). Choosing two closely spaced red emission peaks not only avoids the power dependence of the green and red emission peaks but also minimizes the tissue effect on the peak ratio.

1.5. Radioluminescence

1.5.1 Radioluminescence process

X-rays have been widely used in biomedical field for structural imaging of bone, metal implants and microcavities in soft tissue since its discovery in 1895 by Wilhlm Conrad Roentgen. Radioluminescent materials (scintillators) are luminescent materials which can efficiently absorb high-energy radiation (X-rays) and convert it into photons with wavelengths in the visible and near infrared spectral region which can be detected by a photomultiplier or photodiode.[135] Scintillation process is usually divided into three parts. The first process is the conversion process where the energy of incoming radiation interacts with the material lattice and is converted into a large amount of electron-hole pairs via Compton and photoelectric effect. The second process is the transfer process where the energy of the electron-hole pair is transferred to the luminescent ions and

pumps them to the excited state. The third process is called the emission process where the excited luminescent ions return to ground state radiatively.

1.5.2 X-ray excited optical luminescence

Scintillators (phosphors) have been used in radiation detectors for a long time, and its application in biological systems is still in its infant. Among all the scintillators, gadolinium oxysulphide doped with Tb^{3+} or Eu^{3+} are most commonly used in biological applications due to their chemical stability, large X-ray absorption cross-section, high photon conversion efficiency (6000 photons per 100 keV X-ray photon) and visible to near infrared emission spectra. Carpenter et al. investigated the potential of nanosized inorganic phosphors as biological contrast agents for medical imaging applications using a combined X-ray/optical luminescence imaging instrument.[136] Different concentrations of gadolinium and lanthanum oxysulfide phosphors doped with terbium and europium were incorporated into a mimic tissue phantom. It was demonstrated that X-ray luminescence had a 430-fold greater contrast to background than x-ray fluoroscopy. Recently, X-ray luminescence computed tomography (XLCT) has been introduced as a new molecular imaging modality for imaging radioluminescent nanoparticles embedded in tissue. Pratx and coworkers first proposed and simulated the feasibility of imaging small subjects with XLCT.[137] Tomographic images are generated by irradiating the subjects with a scanning collimated X-ray beam and collecting the visible (near infrared) photons with a photon detector at each position. The X-ray excited optical luminescence is only generated in the path of the collimated X-ray beam as the X-rays could stay

focused after passing through several centimeters of tissue. The spatial resolution is primarily determined by the size of the X-ray beam. Carpenter et al. also introduced limited-angel XLT which has potential for image-guided surgical applications.[138] It was demonstrated both via simulation and phantom experiments that they were able to localize 2-14 mm diameter lesions embedded in 1 to 4.5 cm depth with a median error of 2.2 mm. XLCT system built and integrated with a dual source micro-CT system is able to recover a map of nanophosphor locations and different concentrations using tissue phantoms.[139] In addition, Cong et al. proposed a scanning method to induce luminescence from nanophosphors and reconstruct the three-dimensional distribution of these particles in a biological sample or a small animal using dual-cone beams of x-rays.[140]

In our lab, we developed several functional radioluminescent nanoprobes for drug loading, controlled release and release rate monitoring based on X-ray excited optical luminescence (XEOL). For instance, radioluminescent nanocapsules have been designed for monitoring pH-triggered drug release in vitro.[141] We have also introduced XEOL for measuring chemical concentration without tissue or through thick tissue with high spatial resolution. For instance, Chen et al. constructed a pH sensor film based on inner filter effect with a combination of pH stripes and radioluminescent films.[142] pH sensor with a dynamic range between pH 6-9 and noise level of 0.05 pH unites was developed based on XEOL. The ability to measuring silver film dissolution through 1 cm of chicken breast was also demonstrated.[143] In this dissertation, we described a technique to image pH on a surface through tissue with high spatial resolution.

1.6 Biofilms

1.6.1 Biofilm formation on IMDs

IMDs have greatly improved the life quality of patients and the total number of people with implants is increasing due to the advancement in technology and extended life expectancy. It is estimated that more than 5 million IMDs including prosthetic heart valves, orthopedic implants, intravascular catheters, urinary catheters, cardiac pacemakers and orthopedic implants are used in the United States every year. One concern for these IMDs is that they significantly increase the chance of bacteria invasion and colonization. For instance, it was shown that IMD decreased the minimal infection dose of *S.* aureus more than 100,000-fold.[144] Bacteria may colonize on the implant surface at the time of implantation. For instance, the bacteria on the patient skin can colonize an implant during surgery. They may also reach the implant by haematogenous spreading or through spreading from an adjacent infectious site.[145] Without being treated in time, the bacteria will produce biofilms, which are sessile bacterial cells encased in a self-produced extracellular polysaccharide matrix (mainly consists of polysaccharides, proteins and DNA). Biofilm formation on IMDs includes several stages.[146] First, the bacterium rapidly attaches to the surface of the devices via non-specific interaction forces such as hydrophobicity, van der Waals and electrostatic forces, surface tension and specific binding. Then, the bacterial cells adhere to each other and form a biofilm. The cells within the biofilm release cell-to-cell signaling molecules (quorum sensing) to induce the bacteria to respond in concert by changing patterns of gene expression (mature biofilm). Finally, the biofilms may disperse and colonize on new surfaces.

Depending on the time when the infections occur after surgery, implant infections can be classified to three stages, the early stage which happens within 3 months of implantation, delayed stage which occurs within 3-24 months and late stage which happens more than 24 months later.[147] For the early infection, the patient typically shows some systemic signs and symptoms such as fever, swelling and pain. Delayed infection is usually caused by less virulent microorganisms or mistreatment using a short-term course of non-curative antibiotics. It usually displays subtle signs and symptoms. To diagnose infection after surgery is very challenging as the patient may show these non-specific symptoms such as pain and elevation of C-reactive protein level. However, early diagnosis (within 3 weeks) is the key for successful treatment because the treatment is less invasive and usually antibiotic, or debridement together with antibiotic administration could eradicate infection. If infection was not treated in time, the bacteria will form biofilms and often more invasive treatments such as implant removal and reimplantation are necessary to completely remove the infection. Because bacterial cells within biofilm are much less susceptible to antibiotics than planktonic bacteria due to several different mechanisms. One hypothesis is that the presence of extracellular polymeric substances slows down the diffusion of antibiotics. A second hypothesis is that some cells within a biofilm are at a slow-growing state, which makes them more resistant to antimicrobial agents. A third hypothesis is that some cells within a biofilm adopt a distinct and protected biofilm phenotype, which makes them not susceptible to antimicrobial agents. Hence, it is very important to diagnose and treat bacterial infection early (within 3 weeks).

1.6.2 Biofilm detection methods

Until recently, different techniques have been used to detect bacterial cells and biofilms in vitro and in vivo. Leeuwenhoek first imaged biofilms, dental plaque of his own using his primitive microscope in the 17th century. By dyeing the bacteria with dyes like crystal violet or fluorochromes, optical microscopy was used for bacterial enumeration and imaging. For instance, Wirtanen et al. used epifluorescence microscopy together with acridine orange to study the efficacy of different disinfectants against the formation of biofilms.[148]

The advancement in scanning electron microscope (SEM) has allowed it to provide detailed structures of different types of biofilms. For instance, Mahmound and coworkers used SEM to study the surface topography of bacteria grown as biofilms on soft contact lenses.[149] However, the preparation of SEM samples requires extensive dehydration of the samples which may cause cell shrinkage and disrupt the original structures as natural biofilms contain a large amount of water and they are fully hydrated. The samples for SEM analysis have to be conductive. Hence, metal sputtering is often necessary. In addition, the image area for SEM is quite small.

Recently, confocal laser scanning microscopy (CLSM) and two-photon excitation microscopy (TPE) have been used to study the structure of biofilms in their native states. With the introduction of specific molecular probes, CLSM is capable of determining the identity (oligonucleotide probes) and the physiological state (live vs. dead) of the bacterial cells adherent on transparent or opaque surfaces. For instance, Burnett et al.

studied the attachment of GFP transformed E. coli on the surface and within the internal structures of apples under different conditions using CSLM.[150] However, the penetration depth of CLSM is limited to 20-60 μm. Similar to CLSM, TPE have also been introduced to study three dimensional structure of biofilms. With the utility of a high power pulsed near infrared laser, the penetration depth of TPE is larger due to the introduction of longer-wavelength excitation light but it is also limited to 300-400 μm. For instance, Vroom et al. studied the pH gradients in different types of biofilms using two-photon excitation microscopy based on fluorescence lifetime imaging.[151] However, the biofilms have to be stained with specific fluorochromes such as acridine orange and 4',6'-diamidino-2-phenylindole for being visualized with these two techniques. The staining process may interfere with the native structures of biofilms.

These techniques are capable of studying the structure, compositions and morphologies of biofilms, however, they are usually not used to diagnose bacterial infection (biofilm formation) on IMDs.

Routine blood tests such as C-reactive protein (CRP) or white cell count are inexpensive and noninvasive, and they are usually performed to diagnose bacterial infection as their abnormality may suggest infection. For instance, C-reactive protein and erythrocyte sedimentation rate are often obtained in subjects with orthopedic implants prior to implant removal to assess implant-associated infection.[152] However, they are not helpful after surgery as their concentrations are usually elevated for around 14 days after surgery. In addition, these tests usually have low specificity and their sensitivity depends on the predetermined cutoffs. Colony-forming plate count assays typically take about 48-

72 h but they are only capable of detecting planktonic cells. PCR techniques can shorten the test time but they also use body fluids (blood, saliva, urine) which do not represent the actual biofilm flora colonized on an implant. Microbiological methods such as agar culture of intraoperatively taken swabs or tissue samples are of best sensitivity and specificity, however, they have a larger variability, depending on the sites of sampling.[153] It is recommended that patients should stop receiving antibiotics for at least 14 days before diagnostic microbiological tests to achieve more reliable results. In general, five specimens are acquired at different sites using separated instruments. Then these specimens were cultured in vitro for 5 to 14 days, depending on the types of bacteria. Culturing of fluids from sonicated implants can provide high sensitivity and less culture-negative results, however, this method requires the removal of the implants. For instance, Piper et al. used sonication method to diagnose prosthetic shoulder infection and they found that sonicated fluid culture was more sensitive than periprosthetic tissue culture.[154]

Recently, image techniques have been used to detect implant loosening, tissue necrosis and sinus tract, which could be an indication for bacterial infection. Radiograph can be used to diagnose infection on the implant surface with a sensitivity of 84 % and a specificity of 57 %. However, radiography cannot distinguish between infection and aseptic loosening. A serial of radiographs maybe helpful as the changes occur faster in patients with infection. Radiography is usually not useful for early infection diagnosis. Radionuclide-based technique combines with leucocyte/marrow imaging is reported to have an accuracy of 88%-98%. However, it is complex and expensive to perform and it takes at least 24 h.

Computed tomography (CT) can detect joint effusion, sinus tracts, soft tissue abscesses and bone erosion. However, the infection has already lasted quite long when these symptoms display. The other concern is that the image quality may be deteriorated by the metallic implants due to interference.

Magnetic resonance imaging (MRI) can provide the information of soft-tissue abnormalities around the implant with great resolution. However, MRI can only be used in patients with non-ferrimagnetic implants and the similar to CT, the metal implants may create image artifacts.

Nuclear medicine may suffer from nonspecific tissue uptake of imaging agents and limited by the spatial resolution. Similar to other imaging techniques, it also has good sensitivity but low specificity. Schiesser et al. used positron emission tomography (PET) to study the metallic implant-associated infections in 22 patients with trauma using fluorine 18 fluorodeoxyglucose (FDG).[155] FDG accumulates in various infectious and inflammatory processes due to the increased glycolytic acitivity of granulocytes and mononuclear cells. It was demonstrated that FDG PET is capable of detecting infectious foci with high sensitivity but its reported specificity varies from 50% to 95%.

These imaging techniques are clinically introduced to diagnose bacterial infection noninvasively and indirectly. However, it is difficult to differentiate between fracture instability and an implant-associated infection with current imaging techniques. In addition, these techniques are not useful until the late stage of infection. Optical imaging techniques have also been introduced to detect bacterial infection in vivo. Xiong et al. developed a method for real-time monitoring of biofilm development and assess

therapeutic of various antibiotics in a rat model, using bioluminescent bacteria and an in vivo imaging system.[156] S. *aureus* were engineered to produce bioluminescence by inserting a complete *lux* operon. The bioluminescent signals were first studied in vitro by growing S. aureus in the presence and absence of catheters. Then, they studied the real-time antibiotic efficacy *in vivo* using a rat model of aortic infective endocarditis. Continuous increase in cardiac bioluminescent signals was observed in control animals (untreated), while significant reduction in bioluminescent signals was detected in treated animals (three days of antibiotic treatment). However, there was a threefold increase in bioluminescent signals after the discontinuation of antibiotic treatment for 3 days, which indicated relapsing of bacteria. These results suggest that bioluminescent imaging could be a useful technique to monitor bacterial infection and treatment efficacy in real time in vivo. Alternatively, multiphoton microscopy can also be used to detect fluorescent bacteria (generated using plasmid-borne system or chromosomal fusion) noninvasively in vivo. Recently, Oosten et al. developed a fluorescent method to noninvasively image bacterial infections in vivo in real time.[157] The ability of detecting Gram-positive bacteria caused infection was demonstrated in both a mouse myositis model and a human post-mortem implant model with fluorescently labeled vancomycin. Due to the specificity of vancomycin toward bacteria, this method is also capable of discriminating bacterial infections from sterile inflammation.

1.6.3 Chemical heterogeneity within biofilms

One of the properties of biofilms is their chemical, physical and biological heterogeneity on a microscale. The chemical heterogeneity within biofilms is mainly attributed to the metabolic activity of bacterial cells and the diffusion processes, which results in concentration gradients of metabolic substrate and product.[158] Oxygen distribution within biofilms is one of the parameters well studied. Oxygen concentration is usually measured with oxygen microelectrodes. Zhang et al. studied the competition for substrate and space within biofilms using a microelectrode technique and a micro-slicing technique.[159] They found that the oxygen concentration decreased with increasing depth and it was depleted completely at a depth of about 175 μm for a 220-μm-thick biofilm. In contrast to metabolic substrate (oxygen or nutrients), metabolic products have a higher concentration in the interior of the biofilm as compared to the exterior of the biofilm. For instance, Damgaard et al. studied the concentration distribution of methane in a 3.5-m-thick sewage outlet biofilm using a microscale biosensor. They found that the concentration of methane on the surface of the biofilm was only 10% of that at the depth of 2 mm. [160] The distribution of other solute within biofilm is determined by production, consumption and diffusion.

pH within biofilms is also highly heterogeneous due to the accumulation of waste products. pH within biofilms has been studied with different techniques. Microelectrodes have been used to measure pH in biofilms. However, the size of the microelectrodes is

not that small as compared to the thickness of bacterial biofilms. Generally, 100-μm tips have been used in studying dental plaque biofilms. In addition, the insertion of the probes into the biofilm may disturb the structure of the biofilms. In order to minimize these issues, optical methods were introduced to quantify pH gradients within biofilms. For instance, Vroom et al. measured pH gradients within a mixed culture of oral bacteria based on fluorescence life time imaging using two-photon excitation microscopy.[151] Both lateral and axial pH gradients within biofilms were observed on a microscopically scale with a more pronounced axial gradients. It was also revealed that distinct pH gradients formed after the biofilms were incubated with 14 mM sucrose. pH decreased below 3.0 for some small regions. Hunter et al. used another pH sensitive fluoroprobe (C-SNARF-4) to study pH microenvironment in *Pseudomonas aeruginosa* biofilm via confocal scanning laser microscopy.[161] pH ranging from 5.6 (within the biofilm) to pH 7.0 (bulk fluid) was revealed on a microscopically scale. One of the concerns about using free fluorescent indicators is that the components within biofilms may interact with the fluorescent indicators which may change their pH functionality. Hidalgo et al. studied the pH heterogeneity within both *E. coli* and wastewater biofilms with confocal fluorescence microscopy using ratiometric core-shell silica nanoparticles.[162] By incorporating both pH-sensitive dye (fluorescein) and pH-insensitive dye (Cy5) into a silica shell, pH nanosensors (10 nm) with minimal toxicity, high photostability and sensitivity were prepared. Distinct pH gradients within the biofilms were generated with high resolution. Wolfbeis' group measured the bacterial growth caused pH decrease in real time on agarose matrix.[163] The fluorescent pH-sensitive nanoparticles consisting of green-

emitting pH probe and red-emitting reference dye were incorporated into the agarose and pH measurements were achieved in real time by taking images at different time periods with a digital camera and analyzing the ratios of green over red channels. With this method, a pH decrease from 7.8 to 6.5 was observed over a course of 9 hours.

Based on these studies, we can infer that bacterial infection on IMDs may also create heterogeneous pH distribution. Conversely, bacterial infection on IMDs may be indirectly detected via measuring pH. Konttinen et al. used a sting pH electrode to measure the pH around a loosened total hip prosthesis and they found that interface between the implant and the tissue to be acidic.[6] In this thesis, two optical methods for measuring bacterial growth caused pH variation on surface through thick tissue will be discussed in more detail.

1.7 Photon propagation through tissue

Multiple absorption and scattering events occur as light propagates through biological tissue. The scattering and absorption properties of tissue are related to tissue morphology and tissue biochemistry, respectively. Tissue scatters strongly in the ultraviolet and visible spectral regions. The direction of propagation becomes randomized due to the multiple scattering events.[164] Mean free path (MFP) and transport MFP are usually used to describe the distance a photon can travel between two scattering events and several scattering events, respectively. MFP ($1/\mu_t$) is the average distance a photon can travel between two consecutive scattering events. μ_t is the sum of the tissue's absorption coefficient including absorption coefficient and tissue scattering coefficient, $\mu_t = \mu_a + \mu_s$,

usually $\mu_a << \mu_s$, hence, MFP=1/ μ_s. If considering several scattering events, the reduced scattering coefficient μ_s' is usually used. $\mu_s' = \mu_s (1-g)$, g is the anisotropic term, describing the probability of forward scattering. For photon scattering in tissue, g is usually between 0.8-1. The transport MFP is defined as 1/ μ_s'. Depending on the tissue type and photon wavelength, the MFP is on the order of 100 μm in tissue, while the transport MFP is usually around 1 mm.[165] Tissue optical properties (μ_a, μ_s) can be obtained with a combination of experimental methods and mathematical models. For instance, Farrell et al. have derived both absorption and transport scattering coefficients (μ_a, μ_s') by measuring reflectance using multiple small source-detector at different distances.[166]

Tissue scattering and absorption of photons restricted the imaging depth of the imaging techniques. Traditional microscopy is capable of providing relatively high image quality from tissue with a thickness of 10-20 μm as only a small portion of photons are scattered. Confocal microscopy can provide high-resolution images at depths of several tenths to hundreds of micrometers.[165] With introduction of high-energy laser (long excitation wavelengths) and gradient-index lenses, multiphoton microscopy was demonstrated to imaging beyond 1 mm depth.[167] Stimulated emission deletion fluorescence microscopy has broken down the diffraction limited resolution (~200 nm) and it is capable of provide high quality images with spatial resolution down to ~35 nm.[168] However, there is a tradeoff between spatial resolution and tissue depth. The stimulated emission depletion fluorescence microscopy was demonstrated to have a depth of 120 μm with a spatial resolution from 60-80 nm.[169]

Red to near infrared region (600-1100 nm) is considered as the tissue transparent optical window as the three primary absorbers in tissue (water, oxygenated hemoglobin and deoxygenated hemoglobin) have very weak absorption in this region. Near-infrared light can penetrate several centimeters into tissues. In this week, we make use of the high penetration depth of red to near infrared photons and designed two optical sensors which are capable of measuring localized chemical information (pH) through 6 mm porcine tissue noninvasively.

CHAPTER 2. SURFACE-ENHANCED RAMAN SCATTERING DETECTION OF pH WITH SILICA-ENCAPSULATED 4-MERCAPTOBENZOIC ACID-FUNCTIONALIZED SILVER NANOPARTICLES

2.1 Introduction

The ability to probe intracellular pH is important for understanding physiological processes because pH affects structure of biomolecules and activity of enzymes.[170] Recently, several pH nanosensors were developed based upon surface-enhanced Raman spectroscopy (SERS).[68-70,72,171-173] These nanosensors have been applied to studying pH in CHO cells[171] and HeLa cells,[70] as well as glioma cancer cells during photodynamic therapy.[173] As compared to fluorescent dyes, the SERS signal can be excited with near-infrared light, does not bleach, and displays narrower spectral peaks which allow for simultaneous detection of multiple analytes. In addition, the spectral peaks are separated by only several nanometers, which reduces spectral distortion due to absorption/scattering and chromatic aberrations in tissue. SERS relies on a noble metal surface to enhance the Raman signal of adsorbed molecules via electromagnetic and chemical enhancement mechanisms, with typical enhancement factors of 10^5-10^8, and factors as high as 10^{11} to 10^{12} for single dye molecule.[61] Recently, SERS has been introduced for tissue imaging and remote detection. For instance, Stone and co-workers were able to detect and image four different "flavors" of SERS nanolabels through 4 cm porcine tissue using 830 nm excitation light.[82] If similar sensitivity could be acquired for

pH nanosensors, this would be useful for non-invasive measurements of acidosis in tumors and nanoparticle endocytosis in the lungs of small animal models.[174-175]

A limitation of previous SERS pH nanosensors, however, is that adsorption of proteins and macromolecules could affect the measurements via interactions with the Raman indicator molecules. One strategy to reduce protein interference used in optodes and fluorescent nanoparticles is to encapsulate the indicators into a polymer or silica matrix with pores that exclude proteins and macromolecules and prevent them from interacting with the dye.[176-178] This strategy has been applied to SERS nanofibers optodes and polymer-coated silver electrodes to detect dopamine,[66,179] but has not been applied to designing pH nanosensors based on SERS. Silica encapsulation has also been applied to SERS nanoparticle labels to increase reliability and reduce aggregation.[180] However, the pH dependence of these silica-encapsulated labels has not been explored.

Herein, we demonstrate that SERS pH sensors based upon silver nanoparticles functionalized with 4-MBA (Ag-MBA) are susceptible to bovine serum albumin (BSA) interference at well below physiological concentrations. Encapsulating the particles in silica prevents this BSA interference due to size exclusion and also improves colloidal stability and sensor reliability. Improving the stability of nanosensors based on SERS is important for increasing their reliability because uncontrolled aggregations may cause large intensity variation due to creation of hot spots. This is especially the case when the nanosensors are introduced to biological systems such as intracellular measurements where the complex intracellular environment may induce different degrees of aggregation. We also show that sodium chloride (NaCl) does not significantly influence SERS spectra.

Finally we demonstrate that Ag-MBA@SiO_2 are endocytosed by macrophage cells and detect an intracellular pH drop after endocytosis.

2.2 Results and Discussions

Several groups have reported synthesis of pH sensor based on SERS by functionalizing polydispersed silver nanoparticles with pH sensitive SERS active molecules.[68-70,72,171] However, Zhang and coworkers found that the SERS signal of dyes molecules on silver nanoparticles was significantly attenuated in the presence of large proteins such as BSA.[181] Similarly, pH measurements might be influenced when the nanosensors are introduced to biological systems. We hypothesize that encapsulating Ag-MBA in a porous silica shell will prevent large biomolecules from interacting with SERS molecules but still allow proton ions to diffuse through, similar to other size exclusion sensors.[182] In order to test our hypothesis and reduce macromolecular interference, both silver nanoparticles and Ag-MBA@SiO_2 were synthesized via different methods to study SERS as described above. We characterized the shape and size of particles via SEM, TEM, and DLS. As shown in Figure 2.1A and 2.1B, silver nanoparticles are of various shapes and sizes ranging from 20-100 nm, while Ag-MBA@SiO_2 displayed in Figure 2.1E and 2.1F have an approximately total diameter of 70 nm with a 30 nm thick silica shell. Figure 2.1C and 2.1G show the number weighted hydrodynamic diameter distribution for silver nanoparticles and Ag-MBA@SiO_2, respectively. The plots show that the most common size of silver nanoparticles is around 35 nm, while the size of Ag-MBA@SiO_2 ones is around 70 nm, probably due to the silica shell thickness. Figure 2.1D and 2.1H present

the volume weighted hydrodynamic diameter distribution for silver nanoparticles and Ag-MBA@SiO_2, respectively. It could be observed that Figure 2.1D has a bimodal distribution of particles with a primary peak at around 35 nm and a much broader second peak at around 350 nm, while Figure 2.1H has a primary peak at around 70 nm and another weak peak at around 230 nm. The relative size of the second peak indicates a significant amount of aggregation for silver nanoparticles and far less for Ag-MBA@SiO_2. Additionally, Figure 2.2 shows Ag-MBA@SiO_2 have a strong absorption peak at around 440 nm, while silver nanoparticles have a relatively broader absorption peak at around 460 nm. The narrower absorption peak also supports that Ag-MBA@SiO_2 are less aggregated compared to silver nanoparticles.

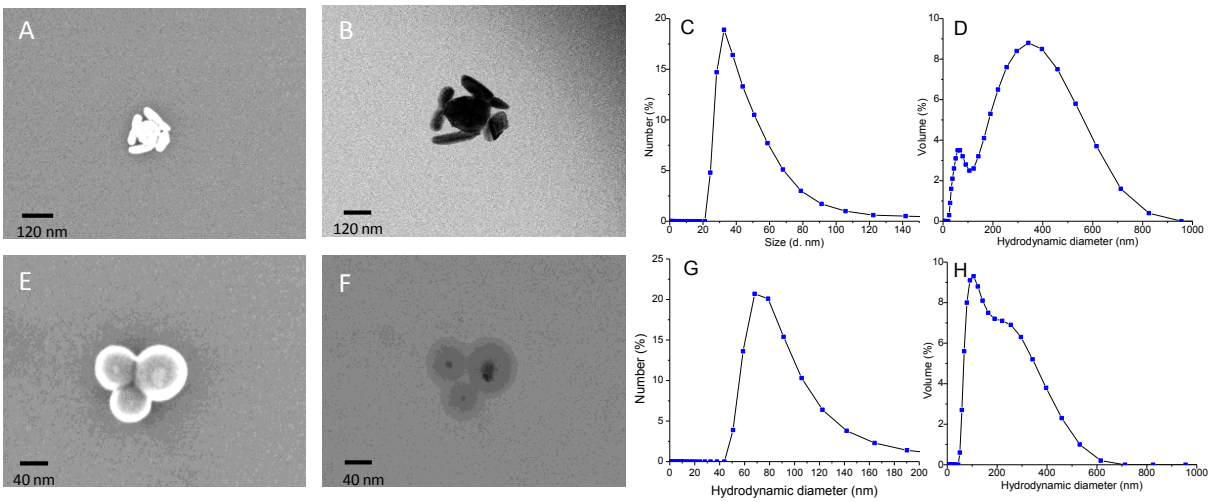

Figure 2.1 Characterization of silver and Ag-MBA@SiO_2 nanoparticles. SEM and TEM images of silver nanoparticles are shown in A and B, while D and E are SEM and TEM images of Ag-MBA@SiO2, respectively. C and G are the hydrodynamic diameter distribution plots by number for the silver nanoparticles and Ag-MBA@SiO2, respectively. D and H are the hydrodynamic diameter distribution plots by volume for the silver nanoparticles and Ag-MBA@SiO2, respectively. The connecting lines are added as a visual guide. Reprinted from Ref. 199 with permission from American Chemical Society.

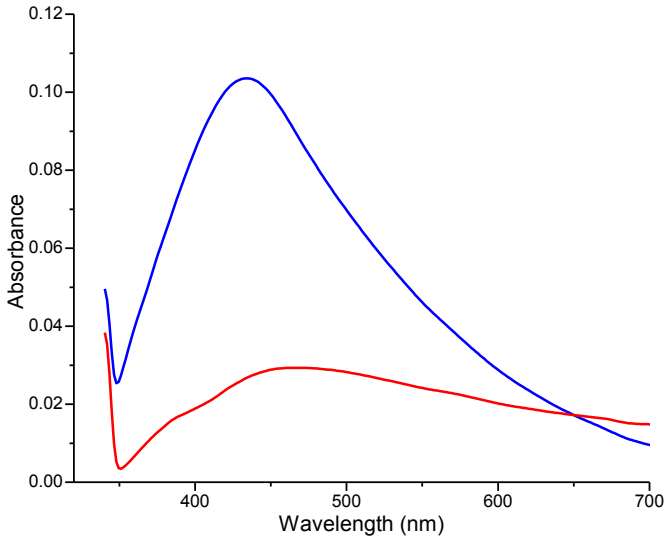

Figure 2.2 UV-vis absorbance spectra. UV-vis absorbance spectra of silver nanoparticles (red line) and Ag-MBA@SiO2 (blue line). Reprinted from Ref. 199 with permission from American Chemical Society.

Different SERS samples were prepared as described in the methods section and SERS measurements were obtained with the setup as displayed in Figure 2.3A. Typical SERS spectra in pH 4 and 7 are shown in Figure 2.3B and 2.3C for Ag-MBA and Ag-MBA@SiO_2, respectively. It is evident that both nanoparticles provide strong pH-sensitive SERS spectra for 4-MBA. These peaks have been assigned to different Raman modes of 4-MBA in detail previously.[67,70] The peak at around 1360 cm^{-1} is attributed to carboxyl stretching mode, which is pH sensitive. The two intense peaks at around 1100 cm^{-1} and 1590 cm^{-1} are attributed to the aromatic ring breathing mode. As is shown in

Figure 2.3, the peak intensity at 1360 cm^{-1} increased as pH increased for both Ag-MBA and Ag-MBA@SiO_2. The orientation of the MBA molecules on the substrate is concentration dependent. At low concentrations, MBA molecules may be flat oriented to the surface.[67] At high concentrations, the MBA molecules tend to stand up to have a high packing density.[68] In our system, there was a saturated coverage of MBA on the surface of silver nanoparticles, we expect the MBA molecules were densely packed with stand up configuration and there could be a tilt to the layer.[183] The π-π stacking interaction between the neighboring MBA molecules would also favor the stand up configuration.[101] In addition, the stand up configuration of the MBA molecules also minimizes the repulsion forces of the carboxylate groups at high pH. The increase in peak intensity at 1360 cm^{-1} indicates the MBA molecules are sensitive to pH variation which implies some of the MBA molecules were vertical to the surface of the silver surface. With addition of different standard buffers, calibration curves for both Ag-MBA and Ag-MBA@SiO_2 were obtained based on peak intensity ratio variation of 1360 cm^{-1} over 1590 cm^{-1}, and they are shown in Figure 2.4A and 2.4B, respectively. From the calibration curves, the pK_a for Ag-MBA is around 5.9, which is similar to previous reports.[68,171] The effective pK_a of our system was defined as the pH at which the intensity changes most. The pK_a for free MBA molecules is around 4.8. Several reasons might cause this pK_a shift. First, the electrostatic interaction between the neighboring MBA molecules might increase the effective pK_a.[184] As the molecules become dissociated, the electrostatic interactions (repulsions) between the neighboring molecules make the neighboring molecules difficult from deprotonating, that is, higher pK_a. Second, ion solvation energy (the energy needed

to break the proton associated with the protonated MBA molecules and becomes surrounded by water molecules) in the interfacial microenvironment may also affect the acid dissociation. The pK_a is around 4.0 for Ag-MBA@SiO_2 and the curve is stretched. As compared to Ag-MBA, the pK_a has shifted by 1.9 units for Ag-MBA@SiO_2. This shift is because the effective proton concentration in the silica shell is different from the proton concentration in the bulk solution. This type of matrix effect is well known in the optode literature. For example, Teramae and coworkers found that the pK_a of pH indicator dyes absorbed to trimethyl ammonium modified silica mesopores shifted 1.8 units.[185] Table 2.1and 2.2 shows value of the average ratios and the corresponding standard deviation of the nanosensos Ag-MBA and Ag-MBA@SiO_2 in response to different buffers, respectively. The stretched calibration curve for Ag-MBA@SiO_2 provides a lager dynamic range. The noise level corresponds to a sensitivity of less than 0.1 pH units from pH 3 to 6 and 0.2 pH units at pH 7 and 8, which makes it suitable in measuring relatively acidic pH in biological systems.

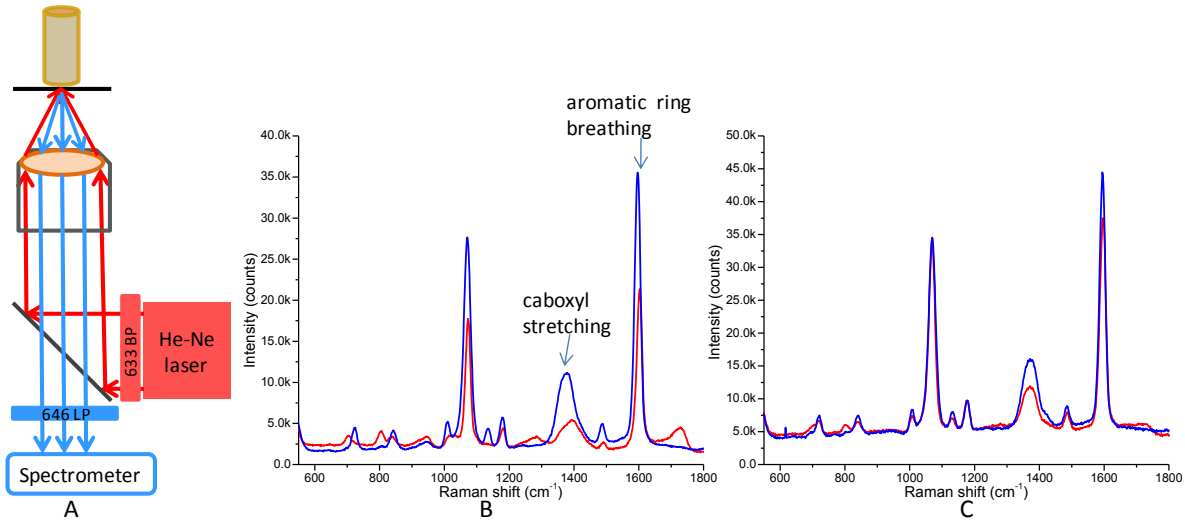

Figure 2.3 SERS setup and pH sensor concept. (A) Schematic diagram of SERS setup; (B) Typical SERS spectra of Ag-MBA in response to standard buffer 4 (red line) and buffer 7 (blue line); (C) Typical SERS responsive spectra of Ag-MBA@SiO_2 toward buffer 4 (blue line) and buffer 7 (red line). Reprinted from Ref. 199 with permission from American Chemical Society.

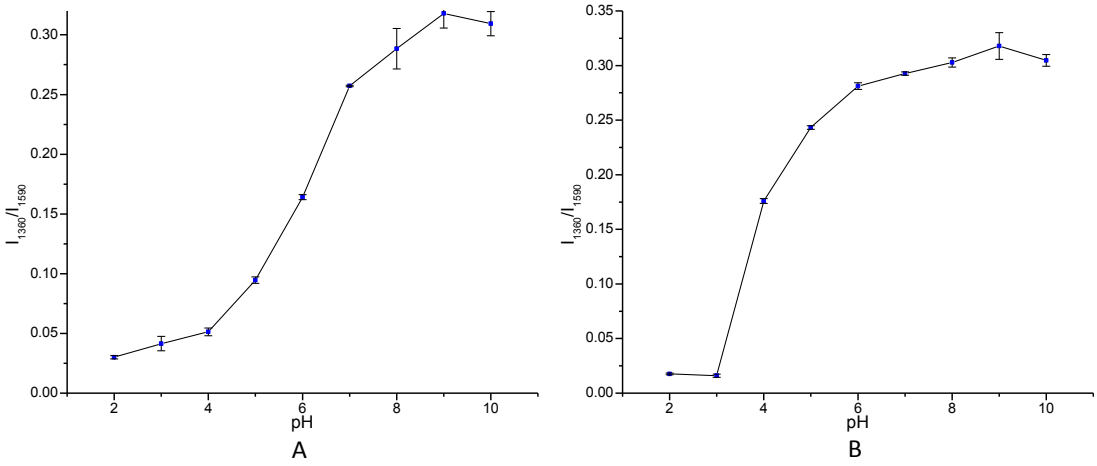

Figure 2.4 pH calibration curves obtained by ploting the ratio of 1360 cm^{-1} to 1590 cm^{-1} against different pH values. (A) Ag-MBA; (B) Ag-MBA@SiO_2. Error bars represent the standard deviation of five measurements at different positions in the same sample. The connecting lines are added as a visual guide. Reprinted from Ref. 199 with permission from American Chemical Society.

Table 2.1 The average and standard deviation of the ratios at different standard buffers for Ag-MBA. The standard deviations were defined as three different places within one sample. The experiments were repeated at least five times. Below are typical results from one of experiments.

Buffers	Average ratios	Standard deviation of ratios
2.0	0.0301	0.0014
3.0	0.0415	0.0060
4.0	0.0513	0.0032
5.0	0.0946	0.0027
6.0	0.1641	0.0021
7.0	0.2572	0.0007
8.0	0.2884	0.0170
9.0	0.3179	0.0122
10.0	0.3093	0.0101

Table 2.2 The average and standard deviation of the ratios at different standard buffers for Ag-MBA@SiO2. The standard deviations were defined as three different places within one sample. The experiments were repeated at least five times. Below are typical results from one of experiments.

Buffers	Average ratios	Standard deviation of ratios
2	0.0176	0.0008
3	0.016	0.0014
4	0.1759	0.0022
5	0.2433	0.0016
6	0.2812	0.0031
7	0.2927	0.0015
8	0.3028	0.0042
9	0.3179	0.0122
10	0.3047	0.0054

According to DLS results, the Ag-MBA@SiO_2 are more colloidal stable than the bare silver nanoparticles. In addition, we observed Ag-MBA@SiO_2 settled at a longer time. In order to investigate the settling time and determine whether settling affects the SERS spectra, we obtained the SERS signal kinetically for both Ag-MBA and Ag-MBA@SiO_2 as described in the experimental section (Section 2.4). Figure 2.5B and 2.5F show that it took a much longer time for Ag-MBA@SiO_2 to settle as compared to Ag-MBA (an approximately time constant of 6 h and 2 h, respectively). From Figure 2.5C and 2.5G, we could observe that the ratios of the two peaks did not change for both types of functionalized nanoparticles except that at the beginning when the SERS intensity was low, likely due to background peak. These results confirm that the Ag-MBA@SiO_2 have better colloidal stability.

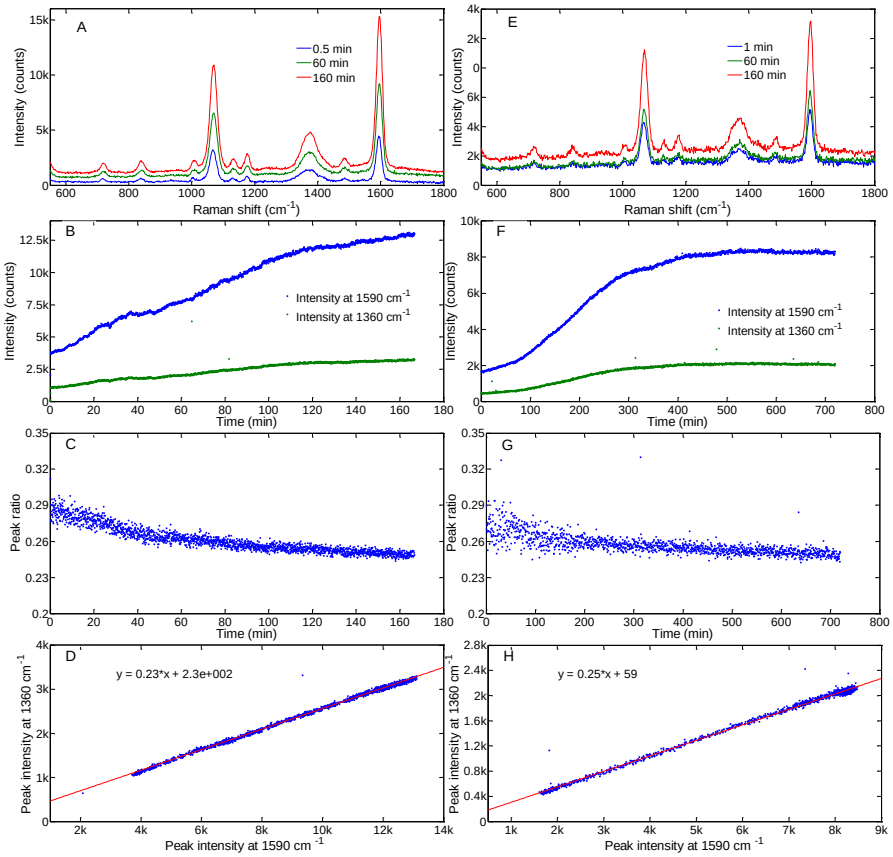

Figure 2.5 Plots for studying the settling effect on nanosensors performance for both Ag-MBA and Ag-MBA@SiO2. Plot A presents typical SERS spectra at different settling times (indicated in the legend) for Ag-MBA; B displays SERS intensity variation at 1360 cm^{-1} and 1590 cm^{-1} over time. C shows the ratio changes of the peak intensity at 1360 cm^{-1} over that at 1590 cm^{-1}; D shows the peak intensity change at 1360 cm^{-1} *vs.* that at 1590 cm^{-1} over time. The red line is the linear fitted line, and the inset is the corresponding linear equations. E, F, G and H are the corresponding plots for Ag-MBA@SiO_2. Reprinted from Ref. 199 with permission from American Chemical Society.

We next studied the selectivity of both pH nanosensors against NaCl. NaCl is an essential electrolyte in biological systems, and other groups have observed that chloride ion affects SERS spectra due to particle aggregation and analyte co-adsorption effects.[186] Figure 2.6A and 2.6B display the SERS spectra before and after adding NaCl to the prepared samples at the center of the calibration curve, pH 7 for Ag-MBA and pH 5 for Ag-MBA@SiO_2. It could be observed that NaCl addition with a final concentration of 50 mM did not affect the SERS signal of either type of functionalized nanoparticles. It is probable that all of the nanoparticles were precipitated to the bottom before adding NaCl, so it could not induce aggregation. Moreover, the silica shells around the Ag-MBA@SiO_2 prevent silver nanoparticles from direct contacting each other to form hot spots. Furthermore, the ratio of the peak for 1360 cm^{-1} and 1590 cm^{-1} remained unchanged, which indicated that NaCl addition would not influence the performance of both types of pH nanosensors.

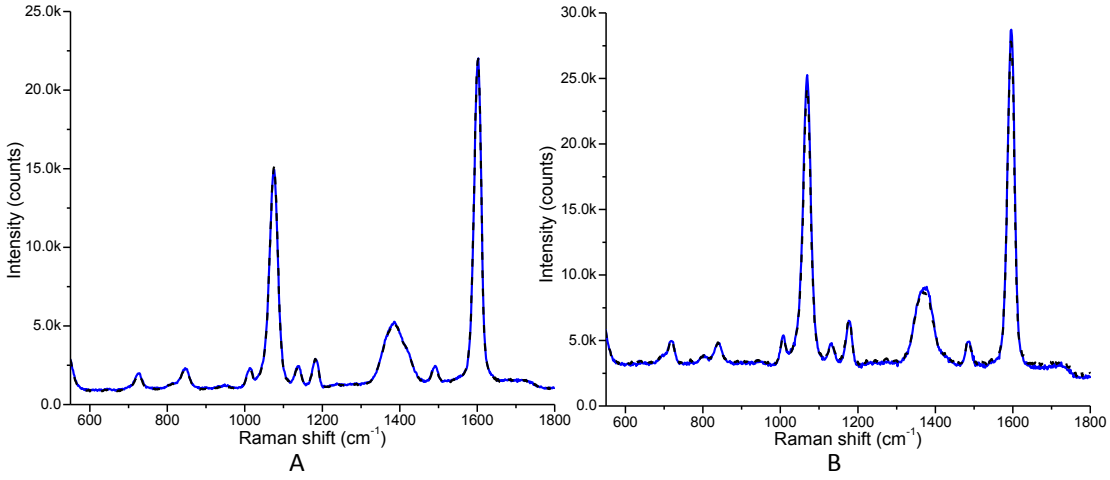

Figure 2.6 The influence of NaCl on the SERS spectra: (A) Ag-MBA at pH 7 before NaCl (blue line) and after adding NaCl with a final concentration of 50 mM (dashed black line); (B) Ag-MBA@SiO_2 at pH 5 before adding NaCl (blue line) and after adding NaCl with a final concentration of 50 mM (dashed black line). Reprinted from Ref. 199 with permission from American Chemical Society.

Proteins are common compounds in biological system that can interfere with sensor measurements. For example, albumin is the most abundant blood protein, accounting for about 60% of blood plasma protein. To test the robustness of the pH nanosensors, 0.2 mg/mL of BSA was added to both Ag-MBA and Ag-MBA@SiO_2. Because no effect was observed for Ag-MBA@SiO_2, we increased the BSA concentration to 55 mg/mL, approximately physiological concentration in blood. SERS spectra were obtained both before and after the addition of BSA. Figure 2.7A and 2.7B show the influence of BSA

on SERS spectra for functionalized silver nanoparticles at the center of the calibration curve, pH 7 for Ag-MBA and pH 5 Ag-MBA@SiO_2 (similar results are observed for Ag-MBA@SiO_2 at pH 7, data not shown). As is shown in Figure 2.7A, the addition of dilute BSA (0.2 mg/mL) to Ag-MBA decreases the ratio of peak intensity of 1360 cm^{-1} over 1590 cm^{-1}, corresponding to 0.6 pH units. This 0.6 pH unit difference is physiologically significant and large compared to reported sensitivity of 0.1 pH units by Halas and co-workers.[68] There are several potential mechanisms for the influence of BSA on the detection of pH for Ag-MBA. Zhang and co-workers observed that different proteins decrease the surface enhanced resonance Raman scattering (SERRS) intensity of several dyes, possibly due to the displacement of dyes by proteins.[181] Similarly, BSA could displace the 4-MBA on the surface of the nanoparticles. However, desorption of 4-MBA from silver nanoparticles would decrease the SERS intensity which was not observed. The BSA could also affect the local environment on the silver nanoparticle surface and decrease the dissociation of the carboxyl group of 4-MBA, which decreases the peak ratio. The spectral change is most consistent with the latter mechanism because no intensity decreases were observed upon BSA addition. BSA was chosen as a common representative protein, it is probable that other intracellular proteins also interfere with the pH measurement for Ag-MBA. To account for these protein effects, *in situ* calibrations can be performed within cells after permeabilizing the membrane to equilibrate with an external buffer. However, such calibrations are performed only at one time and cannot account for changes in protein concentration. The addition of BSA with a physiological concentration to the Ag-MBA@SiO_2 does not influence their

performances as is shown in Figure 2.7B. This is attributed to the presence of silica shell which has pores that are too small to allow BSA to diffuse to the surface of silver nanoparticles. Specifically, the hydrodynamic diameter of BSA is approximately 7 nm, while the pore size of the silica shells prepared by this method is typically around 1 nm.[187-188] Hence, Ag-MBA@SiO_2 provide more robust measurements, especially in complex media such as intracellular measurements in living cells.

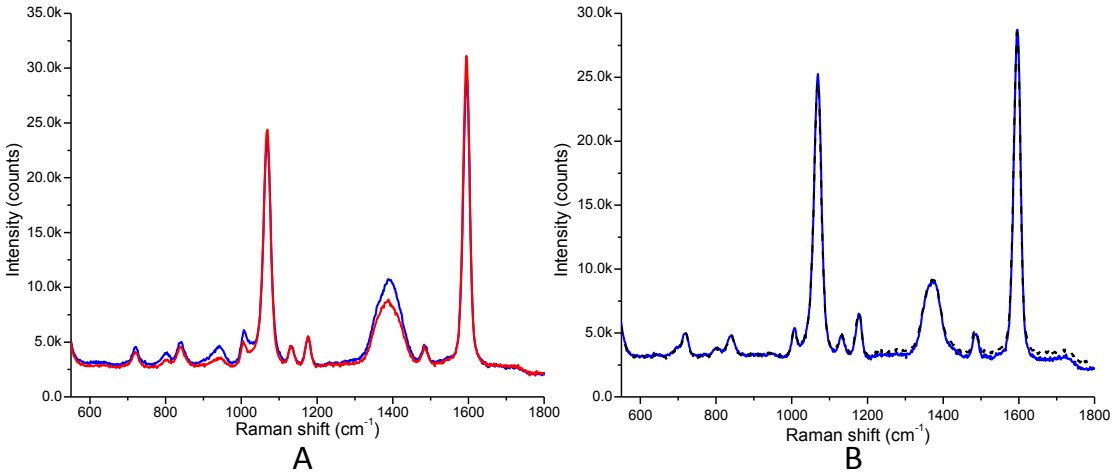

Figure 2. 7 The influence of BSA on SERS spectra: (A) Ag-MBA at pH 7 before adding BSA (blue line) and after adding 0.2 mg/mL BSA (red line); (B) Ag-MBA@SiO_2 at pH 5 before adding BSA (blue line) and after adding 55 mg/mL BSA (dashed black line). Reprinted from Ref. 199 with permission from American Chemical Society.

Macrophage cells are the primary defense cells in the body. They engulf and clear debris, dead cells, pathogens, and inhaled particulate matter.[174] The rate of uptake and clearance plays a role in disease resistance as well as inhalation drug delivery and long

term toxicity of particulate matter. After particles are endocytosed, the pH in the endosome rapidly drops to aid in degradation.[189] The rate of uptake is greatly retarded in patients with obstructive lung diseases, as observed *in vivo* via magnetic twisting cytometry measurements.[190] Developing SERS pH measurements offers an alternative methodology to study nanoparticle uptake that could in the future be spatially mapped via brochoscopy or lower resolution transdermal measurements.[82]

In order to show that Ag-MBA@SiO_2 are capable of detecting intracellular pH in living cells, the nanoparticles were added to the culture medium for 6 h to be ingested by the macrophage cells. The bright field and dark field images for one of the regions covered with cells are displayed in Figure 2.8A and 2.8B, respectively. Figure 2.8C is the corresponding SERS spectrum taken immediately after the images. The Ag-MBA@SiO_2 are clearly visible in the macrophage cells as dark regions under bright field microscopy, and as bright regions under dark field (scattering) microscopy. Macropinocytosis is the most effective mechanism for macrophage uptake of particles with diameter between 30 nm and 200 nm, and is the most likely mechanism of uptake for our silica-encapsulated nanosensors.[191] There were a relatively small number of macrophages on the coverslip, and some regions were covered with nanoparticles and no macrophages. The bright field, dark field and SERS spectrum of a nanoparticle-covered region is shown in Figure 2.8D, 2.8E and 2.8F. We acquired images and spectra from several regions either mainly covered by cells or by Ag-MBA@SiO_2. Intense SERS spectra were obtained from both the particles inside the cells and the particles outside the cells, as shown in Figure 2.8C and 2.8F. The pH in the macrophage is calculated to be 4.4 ± 0.3 from the calibration

curve. These values agree with typical pH in macrophage endosomes of 4.2-6.[22,189,192] Based on the calibration curve, the external pH is estimated to be around 7, which is the approximate pH measured via a pH meter. The dark field, bright field images and SERS spectrum for the control plate with no nanoparticles added are shown in Figure 2.8G, 2.8H and 2.8J. No SERS signal was obtained for the control plate.

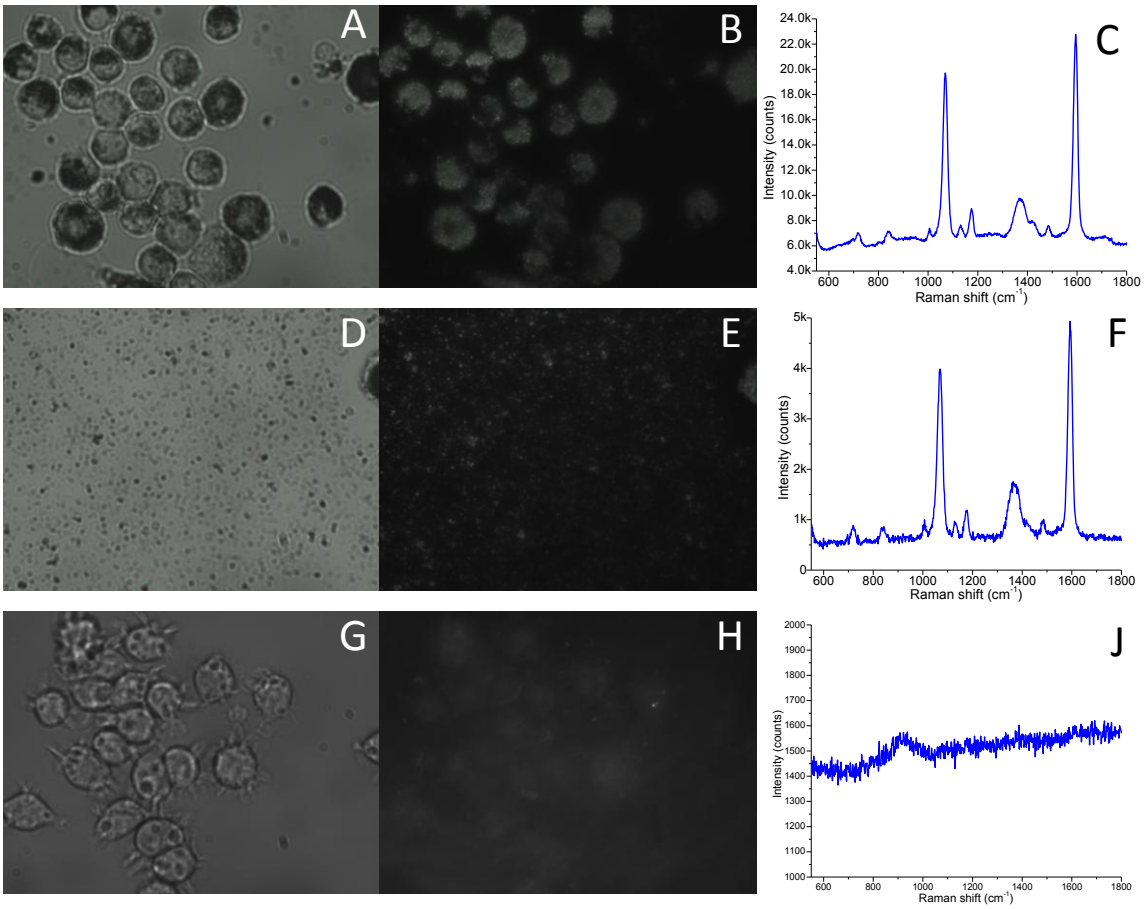

Figure 2.8 Images and spectra of J774A.1 macrophages incubated with SERS nanosensors. A and B are the bright field and epi-illumination dark field images of the macrophage cells incubated with Ag-MBA@SiO_2, C is the corresponding SERS spectrum. D and E are the bright field and epi-illumination dark field images of the regions mainly covered by Ag-MBA@SiO_2, F is the SERS spectrum taken after being imaged. G and H are the bright field and epi-illumination dark field images of macrophages cells without nanoparticles, J is the SERS spectrum taken after being imaged. Reprinted from Ref. 199 with permission from American Chemical Society.

2.3 Conclusion

In conclusion, silica encapsulation of 4-MBA functionalized silver nanoparticles preserves pH sensitivity of 4-MBA, although a pK_a shift was observed as compared to uncoated silver nanoparticles. It was also revealed that low concentrations of biomacromolecules (e.g. BSA) would influence the pH measurement of Ag-MBA. However, by encapsulating silver nanoparticles in silica shells via microemulsion system, the interference from BSA was avoided. A decrease in pH was measured when macrophage cells endocytosed these encapsulated nanoparticles. This strategy could also be applied for detecting other small biological molecules such as glycine and dopamine.[193-194] In future work, we will apply the sensors to non-invasively detecting the rate of endocytosis and acidification by lung macrophages in mouse models using a near infrared excitation laser.

2.4 Experimental Section

All reagents were purchased from indicated companies and used without further purification.

Synthesis of silver nanoparticles: Silver nanoparticles were synthesized using ascorbic acid (Spectrum Chemicals MFG., Gardena, CA) as a reducing reagent. Briefly, for a 10 mL solution, 1 mM silver nitrate (Spectrum Chemicals MFG., Gardena, CA) was reduced by 1 mM of ascorbic acid in the presence of 1 mM sodium citrate (Spectrum Chemicals MFG., Gardena, CA) in a five-dram glass vial. The reaction took place at room

temperature overnight. The obtained nanoparticles were centrifuged with distilled water for three times to remove the excess reagents. The nanoparticles were concentrated to 1 mL in distilled water and the concentration is estimated to be approximately 1 mg/mL, assuming all the silver nitrate was completely reduced. To prepare Ag-MBA, 100 μL 4-MBA in ethanol (3 mM) was also added to 1 mL silver nanoparticles (1 mg/mL).

Synthesis and characterization of Ag-MBA@SiO_2 nanoparticles: Ag-MBA@SiO_2 were synthesized via reverse microemulsion method according to literature with some modifications.[195-196] For a typical reaction, 1.5 mL Triton X-100 (Alfa Aesar, Ward Hill, MA), 7.5 mL cyclohexane (Alfa Aesar, Ward Hill, MA) and 1.6 mL hexyl alcohol (Sigma Aldrich, St. Louis, MO) were added to a 100 mL flask to form a transparent oil phase under stirring, then silver nitrate (1 mM), sodium citrate (1 mM), ascorbic acid (1 mM) and 100 μL 4-MBA (Sigma Aldrich, St. Louis, MO) in ethanol (3 mM) were added to the oil phase sequentially. 5 min later, 40 μL of tetraethyl orthosilicate (TEOS) (TCI America, Portland, OR) was added and then 60 μL of ammonium hydroxide (BDH, West Chester, PA) was added to initialize the silica coating process. The flask was sealed and stirred at room temperature for 24 h. After the reaction was completed, 10 mL ethanol was added to precipitate the nanoparticles and then the nanoparticles were washed and centrifuged with both ethanol and water for three times to remove excess reagents. The nanoparticles were also concentrated to 1 mL, dispersed in water and stored at room temperature. No settling was observed by eye for up to one month in water, while aggregation forms slowly in buffer solutions. The size and morphology of the nanoparticles were characterized with both SEM and TEM. One drop of either type of

nanoparticle solution was added to TEM grids and both the SEM and TEM images were taken with a HD-2000 (200 kV, Hitachi) with a magnification of 110 k. A Zetasizer Nano dynamic light scattering (DLS) instrument (Malvern, Westborough, MA) was also used to determine hydrodynamic size distribution of nanoparticles dispersed in water. UV-absorbance spectra of both kinds of nanoparticles dispersed in water were taken with a UV-2101pc spectrometer (Shimadzu, Torrance, CA).

pH calibration curves and interference studies: To calibrate the SERS sensors, a 100 µL solution of either Ag-MBA or Ag-MBA@SiO_2 was added to a small glass vial, then 400 µL different buffers were added and 300 µL distilled water was added afterwards. The pH values of all the samples were verified with a pH meter (Fisher Scientific, Pittsburgh, PA). The samples were left still overnight to let the functionalized nanoparticles precipitate to the bottom before further experiments. To study to effect of BSA on the functionality of the functionalized silver nanoparticles, 20 µL BSA (2 mg/mL) (Thermo Scientific, Rockford, IL) was added to Ag-MBA with a pH of 7. Both 20 µL BSA (2 mg/mL) and 100 µL of BSA (500 mg/mL) was added to Ag-MBA@SiO_2 with a pH of 5, respectively. SERS spectra were obtained both before and after addition of BSA. To study the effect of NaCl on the nanosensor performance, NaCl with a final concentration of 50 mM was added to either Ag-MBA in a pH 7 buffer, or Ag-MBA@SiO_2 in a pH 5 buffer. SERS spectra were also obtained before and after adding NaCl.

Settling effect on SERS intensity: To study the influence of nanoparticle settling on SERS signal and pH functionality, SERS spectra were kinetically obtained for Ag-MBA

at pH 7 and Ag-MBA@SiO_2 at pH 5. The samples were first dispersed by sonication and SERS spectra were kinetically obtained while the particles were settling down. For Ag-MBA, SERS measurements were obtained every 2s for 2.78 h with an integration time of 3s, while for Ag-MBA@SiO_2, SERS measurements were obtained every 27 s for 12 h with an integration time of 3 s. By the end of acquisition, both types of nanoparticles had settled to the bottom of glass vials.

SERS acquisition setup: The following setup was introduced for all the SERS signal acquisition. Samples were placed on the stage of an inverted microscope ((DMI 5000, Leica Microsystems, Germany). A 5 mW 632.8 nm He-Ne laser (Thorlabs, Newton, NJ), filtered with a 633 nm laser line excitation filter (Chroma Technology Corp, Bellows Falls, VT), was directed to a 10x or 50x objective lens and focused to the bottom of the glass vial. The scattered light was collected with the same objective and the Raman scattered light was passed through a 646 nm long pass emission filter (Chroma Technology Corp, Bellows Falls, VT) before being focused to a spectrometer (DNS 300, DeltaNu, Laramie, WY), equipped with a cooled CCD camera (iDUS-420BV, Andor, South Windsor, CT). SERS spectra were obtained with an integration time of 5 s unless otherwise indicated. The spectra displayed were recorded with the corresponding software without further normalization. For calculating the peak height, the SERS spectra were first smoothed with a second order Savitzky-Golay filter with a frame size of 19 pixels (28.3 cm^{-1}). The peak heights were calculated by deducting the minimum value near the peak from maximum peak intensity.

Intracellular pH measurement: The mouse macrophage cell line (J774A.1) was purchased from American Type Culture Collections. The cells were cultured in high glucose Dulbecco's modified Eagle medium (DMEM, Mediatech, Manassas, VA) supplemented with 10% heat inactivated fetal bovine serum (Thermo Scientific, Logan, UT), penicillin (100 units/mL) and streptomycin (100 μg/mL) as described by Fernando et al.[197] The cells were cultured on coverslips with diameter of 22 mm in 33 mm diameter-petri dishes at 37 ℃ in a humidified incubator with 5% CO_2. After being incubated overnight, 50 μL of Ag-MBA@SiO_2 was added to the culture medium and incubated for 6 h, as to the control plate, 50 μL of 1x PBS was added. The cell plates were rinsed with 1x PBS three times before SERS measurements. The coverslip was mounted to a small incubator in microscope stage, and 1 mL of 1x PBS was added to it. The temperature was set to 37 ^{o}C to mimic the culturing conditions for the cells. Before acquiring SERS spectra with a 50x objective lens, different regions of the coverslips were imaged with the microscope under both bright and dark fields.

CHAPTER 3. DEVELOPMENT OF LUMINESCENT pH SENSOR FILMS FOR MONITORING BACTERIAL GROWTH THROUGH TISSUE

3.1 Introduction and Background

The aging population and advances in biomedical devices are generating increased demand for implanted medical devices (IMDs), such as prosthetic heart valves, orthopedic implants and intravascular catheters.[198] Although IMDs bring substantial benefits to patients, usually several percent become infected, depending on the types of implants and patient population.[147,199-201] These implant infections are difficult to treat because bacteria could form biofilms on the implant surface, and these biofilms reduce antibiotic penetration and contain dormant bacteria especially in hypoxic and acidic regions.[146,158,202] Treatment usually requires implant removal, antibiotic treatment of residual infection, and device replacement, although at early stages more conservative treatments such as débridement become viable.[147,199] However, the bacteria are often localized near implant surfaces specifically at early stages, which brings challenges to the current detection methods. For instance, diagnosis based on symptoms (pain, swelling, and fever) are non-specific, while laboratory tests and radiography are also problematic at early stages since the biofilms are often localized to inaccessible regions on implant surfaces.[147,200-201,203-204] Magnetic resonance imaging (MRI) and computed tomography (CT) can detect bone resorption and sinus tracts but they are not helpful until later stage of infection.[147] Invasive diagnostic methods such as specimens from periprosthetic tissue may not provide reliable information due to the limited sample area.[147] Therefore, a local surface-sensitive and noninvasive sensor is needed to detect implant infections early and

monitor bacterial growth *in situ*. Herein, we demonstrate proof-of-principle for a novel technique to non-invasively detect local pH changes from bacterial growth on a luminescent pH sensing film.

Low pH on an implant surface could be an indication of bacterial infection. Indeed, acidosis is a well-known product of aerobic respiration and fermentation and was used in classic microbiology to classify bacterial species *in vitro* based upon what energy sources they metabolize, as determined by a change in the growth medium's pH. For example, Figure 3.1A shows a photograph of *Staphylococcus epidermidis* ATCC 12228 after overnight growth on a TSA plate supplemented with 0.0025% (w/w) phenol red dye and 1% (w/w) glucose. The phenol red turned yellow in regions where there were bacterial colonies, which indicates an acidic environment. This acidification is due to bacterial respiration and fermentation which generate weak acidic species (e.g. carbonic acid, lactic acid) as schematically illustrated in Figure 3.1B. Furthermore, this metabolic activity generates local acidic and hypoxic regions within biofilms, especially near the implant surface, which are believed to play a significant role in antibiotic resistance.[158] For instance, large pH gradients in the axial direction of oral bacterial biofilms were detected by combining fluorescence lifetime imaging with two-photon excitation microscopy (TPE).[151] In addition, three dimensional pH gradients within *E. coli* and mixed-culture wastewater biofilms were revealed via imaging ratiometric pH nanosensors with confocal fluorescence microscopy.[162] However, these detection methods could not be used to map pH profiles within biofilms on IMDs surface *in situ* due to optical scattering and background fluorescence from the tissue.

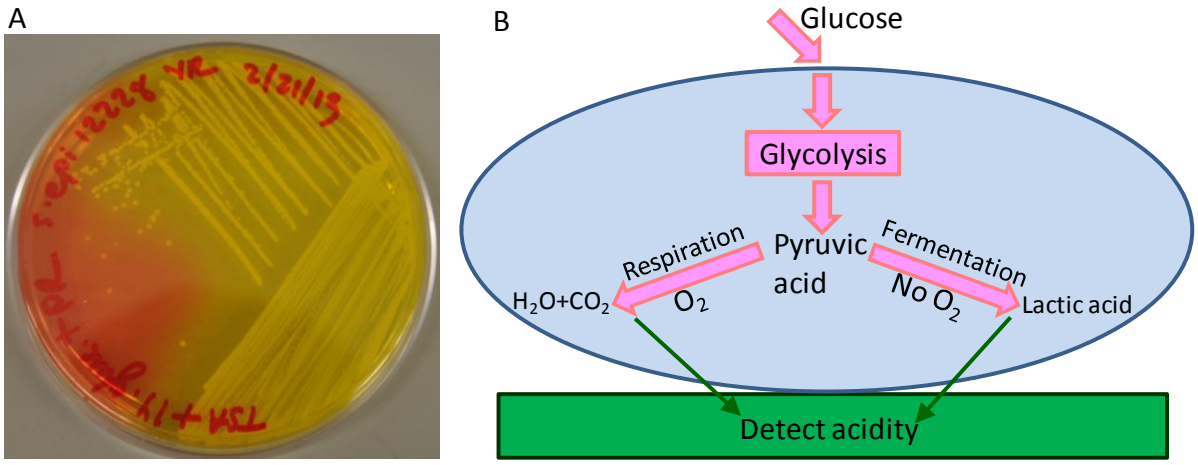

Figure 3.1 pH acidity due to bacterial metabolism. A. A photograph of pH change caused by *Staphylococcus epidermidis* 12228 growth on 1% glucose TSA plate supplemented with phenol red. The phenol red turns from red (neutral) to yellow (acidic) in regions with bacterial colonies; B. Schematic drawing of extracellular acidification caused by cellular glucose metabolism. Reprinted from Ref. 230 with permission from John Wiley and Sons.

Several methods are availble to measure tissue pH, however, they all have limitations, which hinder their ability to monitor pH variation on IMDs surface *in vivo*. For instance, microelectrodes could be used to measure tissue pH. For example, in patients with total hip replacement prosthesis, intraoperative pH measurements with microelectrodes observed a pH of 5.8 on the implant surface due to septic loosening, which is significantly lower than the nearby muscle pH 7.4.[6] However, non-invasive monitoring of a large surface on an implant through tissue would require large flexible electrodes, a power source and telemetry, which would bring manufacturing challenges.[205] MRI can

measure pH using ^{31}P or ^{13}C-carbonate contrast agents but the resolution and sensitivity are poor and it is not surface specific.[2] Positron emission tomography (PET) can measure pH based upon accumulation of ^{11}C- dimethyloxazolidinedione in acidic regions.[206] However, the technique is not surface-specific and has poor spatial resolution and sensitivity for this application. pH sensors based on optical methods have several advantages such as non-invasiveness, high specificity and better portability, which make them suitable for detecting pH in real time and *in situ*.[207-208] However, there are several requirements that would need to be fulfilled before they could detect pH on IMD surfaces through tissue. First, the excitation and emission signal must penetrate through the tissue and generate minimal autofluorescence background. Second, ratiometric pH sensors are necessary to account for variation in total signal intensity due to light attenuation in tissue. Third, these ratiometric pH sensors should be designed to minimize spectral distortion and calibration error caused by tissue absorption and scattering.

To address these issues, we designed a pH sensor with two components: an upconversion luminescence layer serving as a light source, and a layer of pH-sensitive dye that modulates the upconversion luminescence spectrum. We chose upconverting particles (UCPs) as the light source because they could be excited by absorbing multiple near infrared photons with low incident intensity, which allows deep optical penetration through tissue and generates bright luminescence essentially free from autofluorescence.[209-212] Additionally, UCPs have high photostability and low toxicity, which makes them useful for long time intracellular tracking *in vitro* and tumor imaging in animals *in vivo*.[104,213-215] UCP-based sensors have been designed to detect biological

molecules, metal ions, and pH.[118,123,125-126,216] For instance, Wolfbeis' group has designed several sensor films based on the different absorbance of the pH indicators on the green and red luminescence of UCPs for detecting carbon dioxide, ammonia and pH.[126-128] However, these sensors would not be applicable for measurements through tissue because the signal used to calculate pH (i.e. the ratio of green to red light intensity) would be strongly affected by absorption and scattering in the tissue.[134] In addition, the ratio of green to red upconversion luminescence also depends upon the incident light intensity which varies with tissue thickness.[131] To minimize these spectral distortions, our pH sensor films measure the absorbance of a pH indicator bromocresol green (BG) at two closely-spaced red luminescence peaks of UCPs (inner filter effect). The ratio between these closely spaced peaks is not dependent on the illumination power and the tissue attenuates both wavelengths similarly.

3.2 Results and Discussions

Our design employs two layers: a layer of UCPs in polydimethylsiloxane (PDMS) that serves as a background-free red light source and a sensing layer consisting of the colorimetric pH indicator, BG, encapsulated in silica. Upon irradiaiton with 980 nm light, the UCPs emit red luminescence with a spectrum that is modulated by the pH-dependent absorption from the BG-loaded sensing-layer. The luminescence layer is fabricated separately from the sensing layer in order to simplify the fabrication process and increase the flexibility of the design: for example, new types of sensors could be designed by changing the indicators using the same luminescent film. Below, we characterize the

luminescent upconversion layer and describe the pH sensor design, we then study the sensor film's reversibility, stability, and pH calibrations curves with and without a layer of tissue, and finally we apply the film for real time measurements of pH during bacterial growth.

3.2.1 UCPs characterization and pH sensor design

Our goal is to show the proof-of-principle for non-invasively detecting pH variation on IMDs in real time in order to monitor bacterial infection on IMDs. Figure 3.2 shows the concept of our pH sensor film. The pH sensor film comprises of a BG-doped silica layer and a film of UCPs encapsulated in a layer of PDMS as schematically drawn in Figure 3.2A. The size of the UCPs ranges from 200 nm to 300 nm with some degree of aggregation as shown in the TEM images in Figure 3.3. Although the size and morphology of the UCPs is not uniform, in this application, the particles are embedded within a polymer film and the shape does not directly affect the performance of the pH sensor. UCPs with brighter red luminescence emission bands will be used for chemical measurements through deeper tissue in the future.[217-218] The XRD patterns shown in Figure 3.4 match with the standard powder positions of Y_2O_2S hexagonal phase (JCPDS Card No. 24-1422) displayed in Figure 3.4B, which confirms the composition and structure of the host materials. All the luminescence spectra were obtained with the setup shown in Figure 3.2B. The red line in Figure 3.2C represents the luminescence spectrum of UCPs dispersed by a grating with 150 lines/mm. The inset shows the fine structure of red emission peaks of the UCPs resolved by a grating with 1200 lines/mm. These red

emission peaks are assigned to the $^4F_{9/2} \rightarrow {}^4I_{15/2}$ transition of Er^{3+}. The fine structure has been observed before and is attributed to 4f-electron crystal-field interaction.[131,219] The luminescence generated by the UCPs passes through the sensing layer which alters the spectrum in a pH-dependent manner. In order to compare the upconversion luminescence with the BG dye absorption, Figure 3.2C shows both the UCP luminescence spectrum (solid red line, plotted on the left axis and inset) and the absorption spectra of the BG film in standard pH buffer 3 and 7 (orange and green lines, respectively, plotted against the right axis). At high pH, the absorption spectra of the BG-doped silica film overlap with the red luminescence of UCPs. Figure 3.5A shows the absorption spectra in response to a larger range of standard pH buffers (from 3 to 10), and the presence of a clear isobestic point at ~500 nm indicates that there are only two forms of the dye, protonated and deprotonated, with pH-dependent concentration ratios. The 613 nm deprotonated absorption peak intensity increases with increasing pH (Figure 3.5B). More importantly, deprotonated BG absorbes more light at 661 nm than that at 671 nm. This effect is more clearly observed in Figure 3.2D, which shows the normalized luminescence spectra of the pH sensor film in response to standard buffer 4, 7 and 9. The shorter wavelength of red upconversion luminescence decreased more than the longer wavelength when pH increases. Therefore, a ratiometric pH sensor could be designed by taking the ratio of these two peaks. In addition, we note that without the BG sensor film, the upconversion luminescence spectrum of the UCPs is not pH dependent, especially after encapsulation in PDMS. For example, the normalized emission spectra of UCPs before (solid black line) and after (dotted red line) incubation in 1 M sulfuric acid for 5 days overlap almost

perfectly as shown in Figure 3.6, which indicates that the UCPs encapsulated in the PDMS layer are not sensitive to external pH.

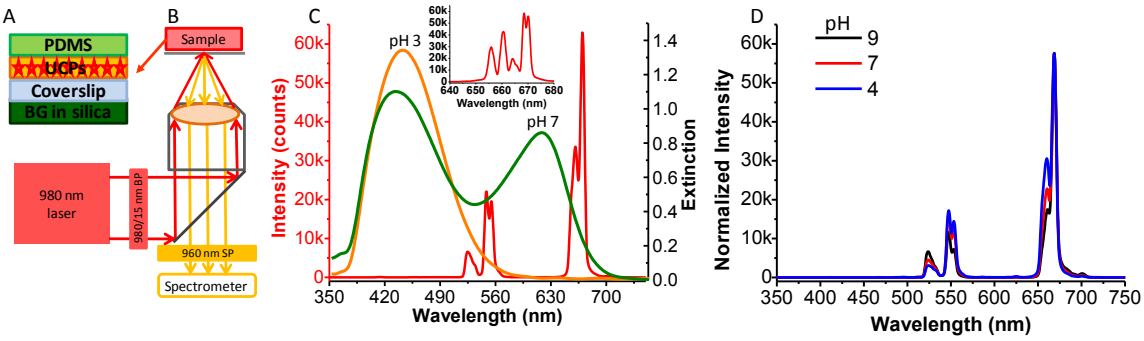

Figure 3.2 pH sensor film working principal. A. Schematic drawing of the side view of the pH sensor film; B. Schematic diagram of the setup for spectra acquisition; C. The overlap between the luminescence spectrum of UCPs (red solid line, plotted against the left y-axis) and the extinction spectra of BG-doped silica films in response to buffer 3.0 (orange, right y-axis) and buffer 7.0 (green, right y-axis). Inset: the red luminescence of UCPs dispersed with the higher resolution grating (1200 lines/mm); D. The luminescence spectra of UCPs dispersed with a lower resolution grating (150 lines/mm) in response to different standard buffers. The spectra were normalized to the peak intensity at 668 nm. Reprinted from Ref. 230 with permission from John Wiley and Sons.

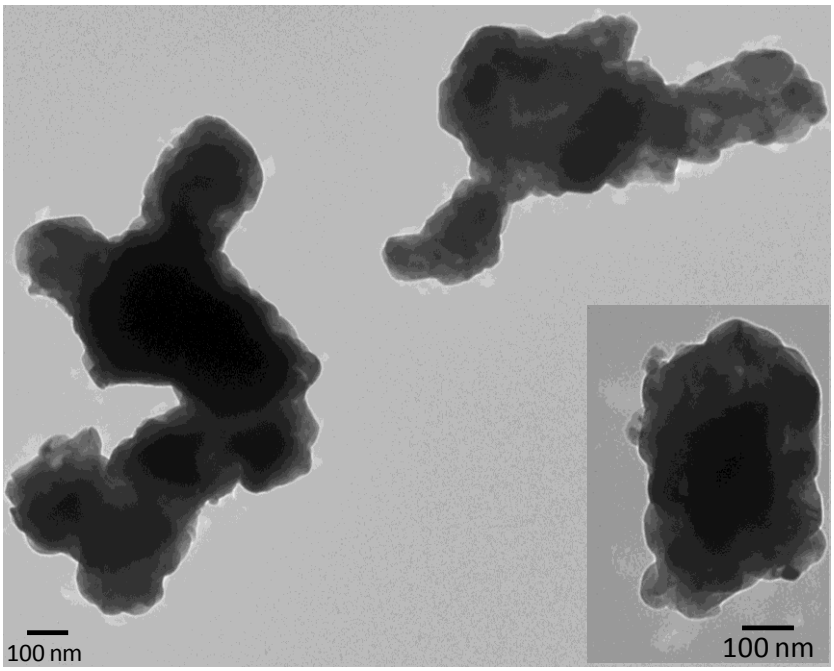

Figure 3.3 TEM images of the UCPs. The scale bars represent 100 nm. Reprinted from Ref. 230 with permission from John Wiley and Sons.

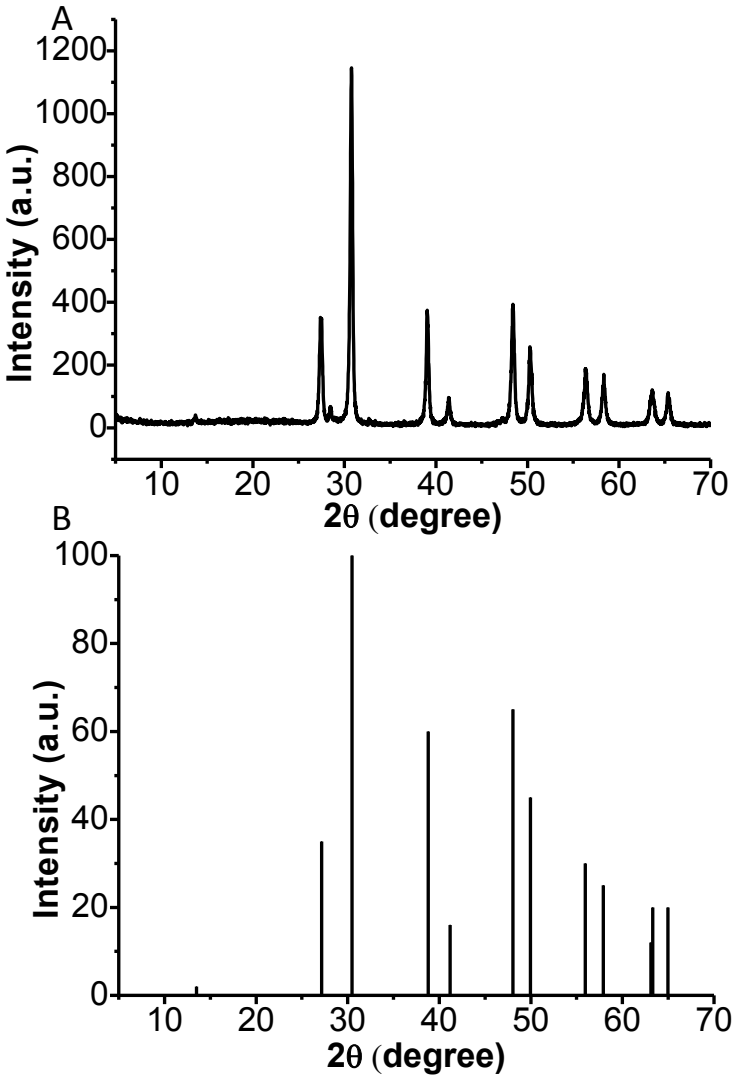

Figure 3.4 XRD of UCPs. A. XRD pattern of the UCPs; B. Standard positions of Y_2O_2S hexagonal phase (JCPDS Card No. 24-1422). Reprinted from Ref. 230 with permission from John Wiley and Sons.

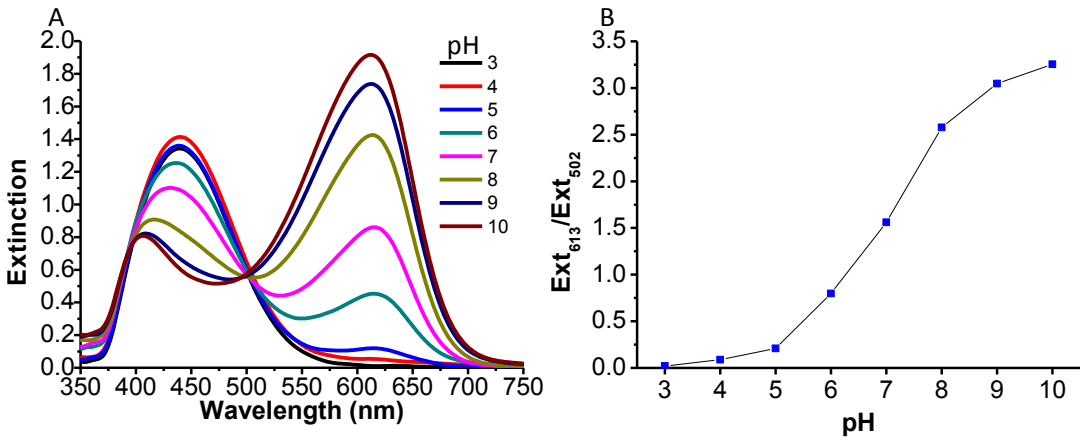

Figure 3.5 UV-vis spectra of pH sensor film. A. UV-vis absorbance spectra of the BG-doped silica film in response to different standard buffers range from pH 3 to pH 10; B. Ratio of absorbance at 613 nm over that at 502 nm as a function of pH. Reprinted from Ref. 230 with permission from John Wiley and Sons.

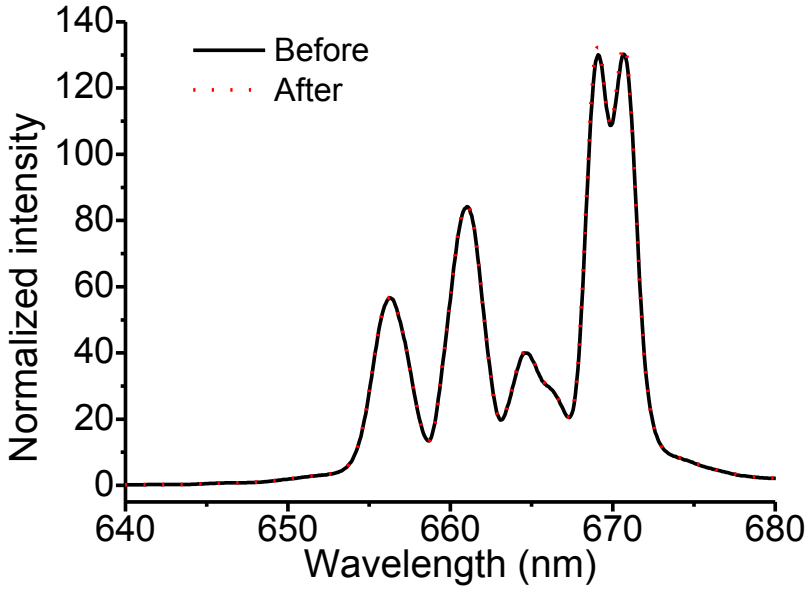

Figure 3.6 Stability of UCPs embedded in PDMS against strong acid. Normalized spectra for UCPs embedded in PDMS before being immersed in sulfuric acid (1M) (solid black line) and after being immersed into sulfuric acid (1 M) for five days (dotted red line). Reprinted from Ref. 230 with permission from John Wiley and Sons.

In order to minimize spectral distortion due to wavelength-dependent optical attenuation in the tissue, and also to minimize the power dependence of the UCP luminescence ratio, we generated a pH calibration curve based upon the ratio of two closely-spaced red emission peaks at 671 nm and 661 nm. To better resolve the spectrum at these wavelengths, we used a high-resolution grating with 1200 lines/mm. To test if these two closely-spaced red emission peaks had the same power dependence, the intensity of the two peaks was recorded as a function of laser intensity on a logarithmic

scale as shown in Figure 3.7A. The two linear fit lines had the same slope, indicating that these two emission peaks had the same power dependence. The slope was 1.35, attributed to a two photon process that begins to saturate at high power intensities.[131] In contrast, Figure 3.7B shows the intensities of the green and red emission peaks as a function of laser power on a logarithmic scale (in order to see both peaks in the same spectrum, we used a grating with 150 grooves mm^{-1}). The green and red peaks had different slopes, indicating that their ratio depends upon the incident light intensity. Specifically, the intensity ratio of green emission over red emission changed by 46 % when the excitation power changed by a factor of 8, while the intensity ratio of the two closely-spaced red emission peaks was unaffected (<1%) within experimental uncertainty. Therefore, the pH calibration curve based upon the two closely-spaced red emission peaks would not be affected by variations in excitation power intensity, while calibrations based on the red and green emission peaks would be strongly affected.

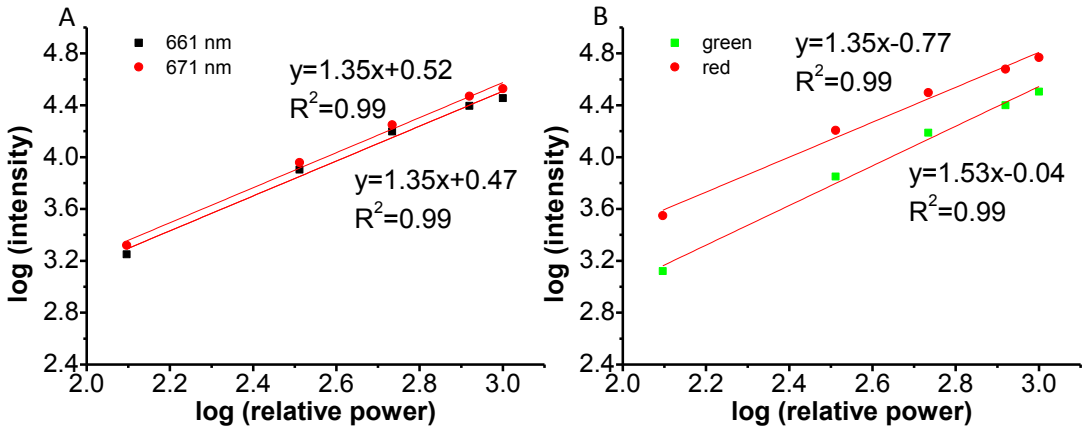

Figure 3.7 Power dependence of UCPs emission. A. Power dependence of the two closely-spaced red emission peaks, 661 nm (black square) and 671 nm (red dot) of the UCPs. B. Power dependence of the green and red emission of the UCPs in green square and red dot, respectively. Reprinted from Ref. 230 with permission from John Wiley and Sons

3.2.2 pH sensing layer reversibility, stability, and calibration curves with/without tissue

To apply these sensors for monitoring pH variation on IMDs, the sensor layer must be reversible with a response time shorter than the expected for pH changes due to bacterial growth. Figure 3.8A shows the real time response of the films to alternate PBS (pH 7.4) and standard buffer 5, repetitively. Nearly the same response was obtained for 6 repetitions with no evidence of degradation. This indicates the BG-doped silica films have good reversibility. The response time was about 10 min for a 90% change, which is

longer than the result reported from literature.[220] The response was relatively slow because our BG-doped silica films were spin-coated twice. Samples with a single coating responded within 1 min, however, double coatings increase the amount of BG and thus increase the sensitivity. Since a 10 min response time is still rapid compared to the time expected for pH changes due to bacterial growth, we used the double coatings in all the experiments.

We next measured sensor stability agaist leaching. The leaching curves for the BG-doped silica films in PBS (pH 7.4) and standard buffer 5 are shown in red squares and black dots in Figure 3.8B, respectively. In buffer 5, there was negligible BG leaching for more than a month. By comparision, in PBS, there was no significant BG leaching for about 5 days, followed by increasing BG leaching over the next 20 days. This leaching effect is probably due to the dissolution of silica at slightly basic pH 7.4. Indeed, the degradation of silica-based HPLC column due to silica dissolution in phosphate buffer pH 7.0 has been observed.[221] The stability of the BG-doped film is sufficient for testing the concept of principle here. In the future, we will covalently immobilize pH indicators in a poly(ethylene glycol) hydrogel to improve the stability and biocompatibility of the pH sensor.[222]

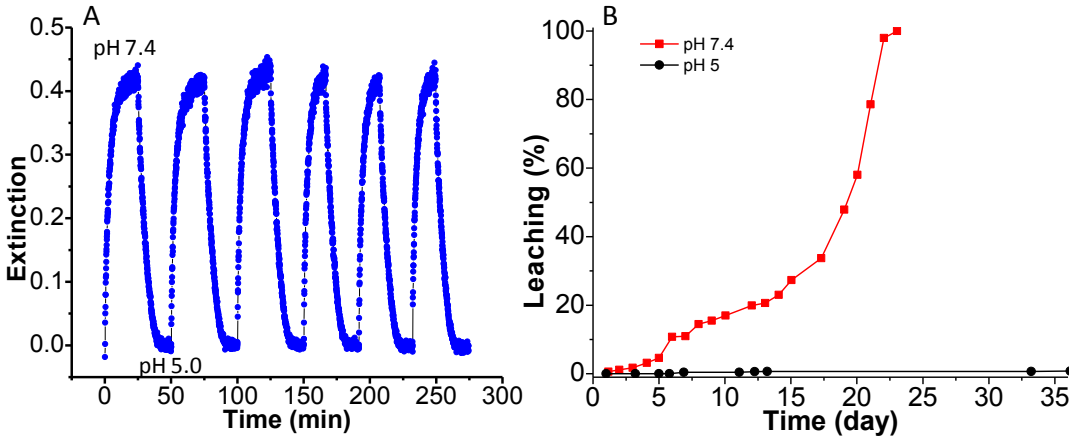

Figure 3.8 Characterizations of pH sensor film. A. Real-time reversibility of BG-doped silica film in response to pH 7.4 and pH 5.0, alternatively; B. Leaching study of BG-doped silica film in pH 7.4 (red square) and pH 5.0 (black dot). Reprinted from Ref. 230 with permission from John Wiley and Sons

To test if the presence of tissue would compromise the performance of our pH sensor film, pH calibration curves were acquired with the sample either embedded between two slices of porcine muscle tissue, or with no tissue. Figure 3.9A shows the luminescence spectra of the pH sensor film in standard buffers ranging from pH 3-10, while Figure 3.9B shows the luminescence spectra of the same pH sensor film in response to different standard buffers with the excitation and emission light passing through the porcine tissue. The corresponding normalized spectra are shown in Figure 3.9C and Figure 3.9D, respectively. As we can see from Figure 3.9A and Figure 3.9B, all the luminescence spectra are background free, which is attributed to the lack of tissue autofluorescence

generated by the 980 nm excitation source. It can also be seen from Figure 3.9C and Figure 3.9D that increasing the pH causes the luminescence intensity at 661 nm to decrease relative to the 671 nm intensity. This spectral change is expected because at higher pH, more of the BG indicator is deprotonated, and deprotonated BG absorbs more light at 661 nm than at 671 nm, as shown in Figure 3.2C and Figure 3.5. Figure 3.9E shows the effective extinction spectrum of the porcine tissue, defined as $\log_{10}(I_{\text{no tissue}}(\lambda)/I_{\text{tissue}}(\lambda))$, where I is the upconversion luminescence intensity at wavelength λ. Although the luminescence intensity decreases by a factor ranging from 30 to 300 after the light passes through the porcine tissue, the effective extinction spectra are quite flat, which means that the porcine tissue did not significantly distort the shape of the spectral in this region. Table 3.1 and 3.2 shows the actual values of the intensity ratio and standard deviations of the sensor film in response to different buffers without and with tissue, respectively. Figure 3.9F shows the intensity ratio of upconversion luminescence at 671 nm over 661 nm as a function of pH for an external sensor film and a sensor film placed between two pieces of porcine tissue, with the top slice about 8 mm thick and the bottom one 6-7 mm thick. It is shown that the pH sensor film is responsive to different pH range from 5 to 10. The pK_a of the pH sensor film is 7.0, while the pK_a of free BG is around 4.8. This pK_a shift agrees with what was reported in the literature and it is mainly attributed to the hydrophobic nature of the hybrid silica film.[220] More importantly, the two calibration curves are in good agreement, which means that the presence of thick porcine tissue does not substantially affect the pH calibration curve. Hence, it is possible to monitor pH variation through up to 6-7 mm tissue by referring to the pH calibration

curve generated without passing through tissue. This calibration robustness will be useful for *in vivo* pH measurement and this ability may provide useful information for early diagnosis and treatment of bacterial infection on IMDs.

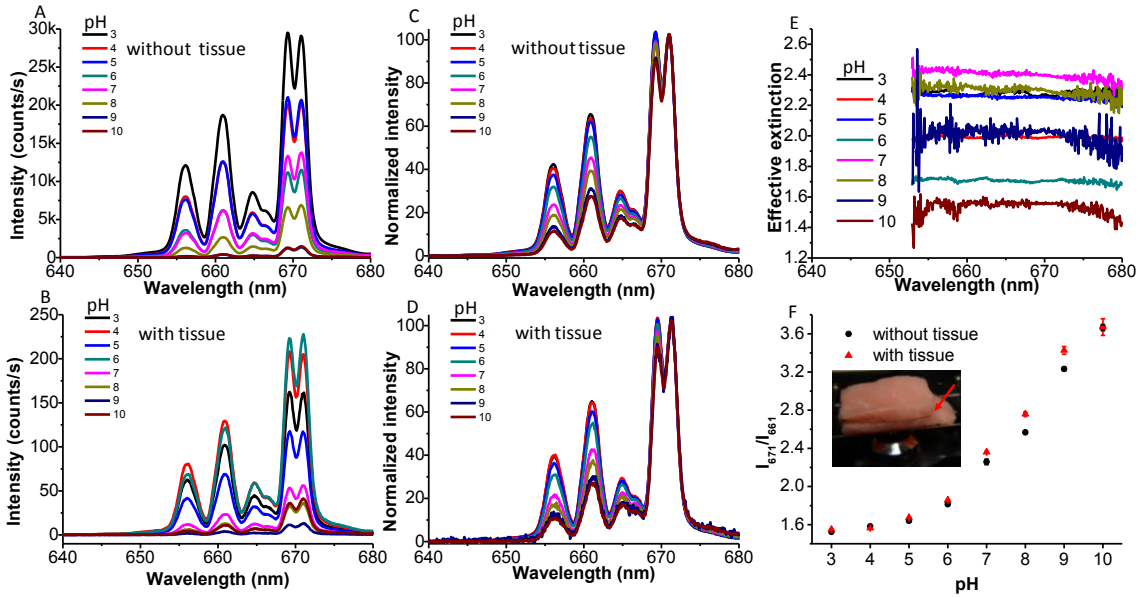

Figure 3.9 pH calibration curves without and with tissue. A. Upconversion luminescence spectra of the pH sensor film in response to different standard buffers range from pH 3.0 to pH 10. B. Upconversion luminescence spectra of pH sensor film in response to different standard buffers after passing through 6-7 mm porcine tissue. C and D are the spectra from A and B normalized to the peak at 671 nm, respectively. E. The effective extinction spectra of UCPs due to the presence of porcine tissue. F. pH calibration curves of the pH sensor film without (black dot) and with passing through porcine tissue (red triangle). Inset: Photograph of the pH sensor film sandwiched between two pieces of porcine tissue on the microscope stage for generating pH calibration curve through porcine tissue. The red arrow indicates that the pH sensor film was sandwiched between the two pieces of porcine tissue. Reprinted from Ref. 230 with permission from John Wiley and Sons.

Table 3.1 The average and standard deviation of the ratios of the film in response to buffers without tissue. The standard deviation is defined as one standard deviation of three different places within the same sample. The experiments were repeated at least five times. Below are typical results from one of experiments.

Buffers	Ratio average	Standard deviation of ratios
3.0	1.523	0.0117
4.0	1.582	0.0108
5.0	1.641	0.0141
6.0	1.814	0.0115
7.0	2.258	0.0278
8.0	2.568	0.0133
9.0	3.232	0.0171
10.0	3.665	0.0321

Table 3 2. The average and standard deviation of the ratios of the film in response to buffers through tissue. The standard deviation is defined as one standard deviation of three different measurements within the same sample. The experiments were repeated at least five times. Below are typical results from one of experiments.

Buffers	Ratio average	Standard deviation of ratios
3.0	1.549	0.0046
4.0	1.565	0.0017
5.0	1.674	0.0030
6.0	1.857	0.0042
7.0	2.360	0.008
8.0	2.759	0.0206
9.0	3.427	0.0407
10.0	3.671	0.0874

3.2.3 Real time pH monitoring through tissue

Having made and characterized the pH sensor film, we next tested if our pH sensor film could monitor the pH variation due to bacterial growth on a tryptic soy agar (TSA) plate through thick tissue. We chose *S. epidermidis* as the model bacterium because it is a common inhabitant of human skin and has been notorious for nosocomial infections.[198] The pH variation due to bacterial growth at the interface of the TSA plate and the pH sensor film was detected in real time through porcine tissue with a thickness of 6-7 mm. The red dots in Figure 3.10A represent the real time pH variation caused by *S. epidermidis* growth on a TSA plate supplemented with 1 % glucose as a function of time. The outliers were due to the cosmic spikes during the real time acquisition. The plot shows that the pH gradually decreased soon after the bacteria were inoculated onto the TSA plate. After the experiment concluded, the porcine tissue was removed and the TSA plate with the pH sensor film was photographed as shown in Figure 3.10B. *S. epidermidis* colonies were seen growing on the edges of the pH sensor film and the color of the BG-doped silica layer had changed from green to yellow indicating acidosis. This indicates that the presence of bacteria indeed induces pH variation, and this pH variation could be detected through thick porcine tissue with our pH sensor films. The black squares in Figure 3.10A are the control results by adding the same volume of PBS instead of bacterial culture. The ratios of the two chosen peaks are stable during the whole acquisition period, which indicates the pH was constant. This could be further verified through the photograph of the pH sensor film on the TSA plate taken by the end of the acquisition as shown in Figure 3.10C. The TSA plate was free of bacteria and the color of

the pH sensor film remained green at the end of the acquisition, which indicates neutral pH. Based on the pH calibration curve through tissue with the same thickness, the pH due to *S. epidermidis* growth was calculated to be around 5.7 by the end of acquisition, while the pH of the control was around 7.4. This result is similar to that of Wang and co-workers who used fluorescent pH sensitive nanosensors to measure pH during *E. coli* growth on agarose, and observed a pH decrease from 7.8 to 6.5 over the course of 9 hr.[163] However, the use of fluorescein as the pH indicator limits their ability to detect pH through tissue. Here our design allows pH detection through biological tissue and the results show a great potential for our pH sensor films to detect real time bacterial infection on IMDs *in situ*.

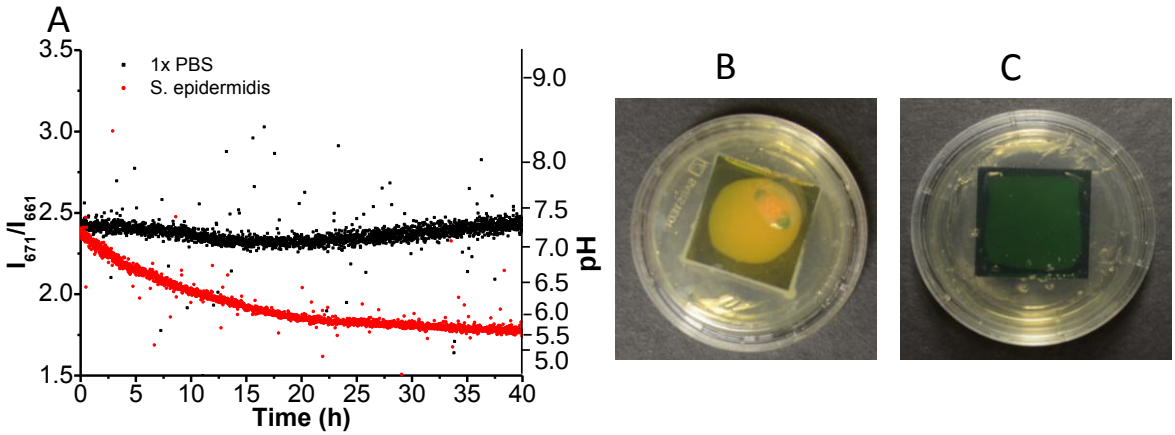

Figure 3.10 Real time pH detection with the pH sensor films passing through 6-7 mm porcine tissue. pH decreases due to the growth of *S. epidermidis* inoculated to the TSA plate (red dot), pH variation of the control sample, by adding the same volume of PBS (black square). The right axis is the corresponding pH calculated based on the calibration curve through 6-7 mm porcine tissue; B. Photograph of the pH sensor film by the end of acquisition innoculated with *S. epidermidis*; C. Photograph of the control sample by the end of acquisition. The UCPs are coated in an approximately circular region below the film. Reprinted from Ref. 230 with permission from John Wiley and Sons.

3.3 Conclusion

In conclusion, we constructed pH sensor films based on the inner filter effect between the BG-doped silica film and the two closely-spaced red emission peaks of the UCPs. The upconversion luminescence spectrum is essentially background-free when applied in biological tissues. Selecting two closely-spaced red emission peaks of the UCPs minimizes spectral distortion of the emission light caused by tissue absorption and scattering, and also minimizes the power dependence of the UCPs. Finally, the pH decrease due to the growth of *S. epidermidis* on the interface between the TSA plate and pH sensor film was monitored through thick porcine tissue in real time. These proof-of-principle experiments demonstrate the great potential of detecting bacterial infection on IMDs *in vivo* in biomedical field. In the future, we will improve the long term stability of the BG-doped silica films by changing the matrix to a more stable polymer and covalently binding the pH indicators. X-ray scintillator particles will also be introduced as an X-ray addressable *in situ* light source to construct images with higher spatial resolution.[142] Alternatively, photoacoustic spectroscopy could be used to detect pH through up to 5 cm thick tissue with our BG-doped silica film.[223-224] We will also try to coat the pH sensor films to the medical implants such as fracture fixators and apply them for *in vivo* pH monitoring in a rabbit model.

3.4 Experimental section

Materials: All chemicals were used as received without any further purification. Y_2O_3, Yb_2O_3, Er_2O_3, bromocresol green (BG), tetramethoxyl orthosilicate (TMOS), methyltrimethoxysilane (MTMOS), sodium fluoride (NaF) were purchased from Alfa Aesar (Ward Hill, MA). All the rare-earth nitrates were prepared by dissolving the corresponding oxides with an appropriate amount of nitric acid (6N) at elevated temperature. Carboxymethylcellulose (CMC) was purchased from Fisher Scientific (Pittsburgh, PA). D (+) Glucose was purchased from Sigma-Aldrich (Saint Louis, MO). PDMS base and its curing agent were purchased from Dow corning (Midland, MI). Hydrochloric acid (2 N), nitric acid (6 N), standard pH buffers and sulfuric acid (6 M) were all purchased from BDH (West Chester, PA). Reagent alcohol, tryptic soy broth (TSB) and tryptic soy agar (TSA) were ordered from EMD (Gibbstown, MJ). Urea was purchased from Amresco (Solon, OH). *Staphylococcus epidermidis* 35984 and *Staphylococcus epidermidis* 12228 were purchased from ATCC (Manasssas, VA).
Synthesis and characterization of UCPs: Upconverting particles Y_2O_2S: Yb^{3+}, Er^{3+} (UCPs) were synthesized according to literature with some modifications.[225] First, precursors were prepared using a homogeneous precipitation method. For a typical reaction, urea (6 g) was added to 100 mL solution, containing $Y(NO_3)_3$ (10 mM), $Yb(NO_3)_3$ (0.65 mM) and $Er(NO_3)_3$ (0.13 mM). Precipitates were generated by heating the mixture to 80 ^oC for 2 h. The precipitates were centrifuged for three times with

distilled water to remove the excess reagents. Then a slight amount of NaF was added to the particles before they were calcinated at 800 ^{o}C for 2 h. The sulfuration reaction was performed in a quartz tube furnace with sulfur powder at 700 ^{o}C for 1 h under argon protection. To acquire transmission electron microscopy (TEM) images, a drop of UCP solution was added to a TEM copper grid and dried at room temperature. The images were taken with an H-7600T (Hitachi) at an acceleration voltage of 120 kV. The composition and structure of the UCPs were confirmed by powder XRD patterns, which were obtained on a Rigaku diffractometer at 40 kV and 40 mA. The upconversion luminescence spectra of the UCPs were obtained with the setup displayed in Figure 2B. A 500 mW 980 nm diode-pumped solid state laser (Changchun New Industries Optoelectronics Technology, Changchun, China), filtered with a 980/15 nm band pass filter (Chroma Technology Corp, Bellows Falls, VT), was directed to a 5x objective lens and focused to the sample on the stage. The upconversion luminescence spectrum was collected with the same objective and passed through a 960 nm short pass emission filter (Chroma Technology Corp, Bellows Falls, VT) before being focused to a spectrometer (DNS 300, DeltaNu, Laramie, WY). The upconversion luminescence was spatially dispersed by a grating with 1200 lines/mm otherwise indicated and collected with a cooled CCD camera (iDUS-DU420A-BV, Andor, South Windsor, CT), set to 100 kHz transfer such that each digital count corresponded to 15 photoelectrons. The spectra were recorded with Andor's Solis software. For studying the spectral variation of UCPs in response to sulfuric acid, the coverslip deposited with only the UCPs, which were

encapsulated in a layer of PDMS, was immersed to sulfuric acid (1 M) for five days. The luminescence spectra were obtained before and after being incubated in sulfuric acid.

Preparation and characterization of BG-doped silica film: Organically modified silica films doped with BG were prepared according to literature with some small modifications.[220] The hybrid silica sol was prepared by combining TMOS with MTMOS in a molar ratio of 2:1. In a typical preparation, TMOS (320 μL) and MTMOS (138 μL) were mixed in reagent alcohol (228 μL), an appropriate amount of water was added to maintain the molar ratio of silane over H_2O to be 1:4, then HCl (166 μL, 0.1 M) was added to initiate the polymerization. Then, BG (30 mg) was added to the mixture. After being stirred for 24 h at room temperature, an aliquot of the sol (40 μL) was spread onto a precleaned microscopic coverslip (18 mm x 18 mm) for 30 s and then spun cast at 2500 rpm for 20 s to form a transparent, uniform silica film. These films were dried at room temperature under a relative humidity environment of ca. 40 % for 1 day. Then another layer was coated on the top of the first layer with another fresh sol, which was prepared with the same protocol as the first layer. The prepared films were dried at room temperature for at least 3 days before further experiments. To measure the absorbance spectra of BG-doped silica films in response to different pH, different standard pH buffers (20 μL) were added to the surface of a BG-doped film for 15 min. Then, the film was attached to a movable stage and UV-vis absorbance spectra were taken with a UV-2101pc spectrometer (Shimadzu, Torrance, CA). To study the reversibility of the BG-doped silica films, a BG-doped film was fixed to a Petri-dish bottom and placed onto the microscope stage. Absorbance variations in response to alternate pH 5.0 and PBS (pH

7.4) were recorded in real time with the microscope head lamp (tungsten filament) as the light source. The spectra were recorded with an acquisition time of 0.1 s in every 30 s for 20 min. For studying the leaching property of the BG-doped silica films, the films were incubated in 20 mL buffer 5 (pH 5.0) or PBS, respectively. 3 mL of the solutions were taken out at indicated time for UV-vis absorbance measurements with the corresponding buffers as references. After measurements, the solutions were put back to the samples. Standard calibration curves for free BG in buffer 5 and PBS (pH 7.4) were generated to quantify the BG leached out from the doped silica films.

pH sensor film preparation: pH sensor films were prepared according to the following procedures. First, UCPs were dispersed in 0.5 % CMC with a concentration of 3 mg/mL. Then 150 μL of the solution was added to the other side of the BG-doped silica films, a film of UCPs was formed after being dried at room temperature overnight. Then PDMS with a base to curing agent ratio of 10:1 was spread onto the surface of UCP film to keep the UCPs in position. The PDMS layer was cured at room temperature for 3 days.

pH calibration curves without and with porcine tissue: To generate calibration curves, a pH sensor film was immersed into a series of standard buffers, ranging from pH 3 to pH 10 for 15 min. The pH sensor film was sealed with plastic wrap before obtaining upconversion luminescence spectra with the setup described above. To generate the calibration curve without passing through porcine tissue, the film was sandwiched between two pieces of white paper and the acquisition time was 2 s. To generate the calibration curve with tissue, the film was placed between two pieces of porcine tissue

and the acquisition time was 20 s. pH calibration curves were obtained by plotting the peak intensity ratio of 661 nm over 671 nm as a function of time.

Bacterial culture and real time pH detection through tissue: Fresh culture of *Staphylococcus epidermidis* ATCC 35984 was prepared by inoculating sterile TSB (5 mL) with a single colony from a TSA plate streaked for less than one week. Bacteria were grown to the stationary phase under shaking conditions at 37 ^{o}C for 16-18 h. The number of bacteria was quantified by measuring the optical density at 600 nm (Smartspec 3000, Bio-Rad). The culture was diluted to 10^{8} CFU/mL with sterile PBS. Afterwards, 2 μL of this diluted culture was added to the center of a 1 % glucose TSA plate (35 mm in diameter). The pH sensor film immersed in PBS for 12 h was then laid on top of the TSA plate after the spotted bacterial culture evaporated. Then porcine tissue with a thickness of 6-7 mm was used to wrap the plate. The tissue-wrapped TSA plate was put into a larger Petri dish, which was placed onto the microscope stage. Upconversion luminescence spectra were obtained every 1 min with an acquisition time of 20 s for about 40 h. The porcine tissue was exposed to the 980 nm laser intermittently when data was being acquired with the introduction of a shutter in front of the laser. Sterilized PBS (2 μL) was added to the TSA plate for the control experiment. Spectra were also recorded in real time with the same parameters. Peak ratio variations as a function of time were obtained by analyzing the raw spectra without further normalization or smoothing. Images of the pH sensor films in the TSA plates were taken after the acquisition was terminated. For determining the real time pH variation, the calibration curve through 6-7 mm porcine tissue obtained above was fitted to a fourth power polymonimal curve.

CHAPTER 4. X-RAY EXCITED LUMINESCENCE CHEMICAL IMAGIMG OF BACTERIAL GROWTH ON SURFACES IMPLANTED IN TISSUE

4.1 Introduction

Although implanted medical devices (IMDs), such as fracture fixation devices, prosthetic joints, and pacemakers, have greatly improved patients' lives, the implant surface can be colonized by bacteria resulting in the formation of antibiotic-resistant biofilms especially in vulnerable populations.[198,226] For example, approximately 5% of the 200,000 fracture fixation devices implanted each year in the US become infected,[227] and 40% of battlefield injuries with internal fixation, due to increased wound trauma and increased likelihood of debris in the wounds.[228] While infections caught early can often be treated with a combination of debridement and antibiotic therapy, after approximately three weeks, the implants usually must be removed followed by antibiotic treatment and device replacement, with associated risks from prolonged hospitalization and surgeries.[147] In addition, it is difficult to monitor bacterial infection noninvasively during treatment. Hence, there is a need for developing methods to detect bacterial infections and monitor treatment in situ. Clinic diagnostic methods such as clinical symptoms and intraoperative tissue culture have limited specificity and sensitivity (e.g. intraoperative tissue culture has a sensitivity of 65-94%.), while MRI and CT of bone resorption and sinus tracts are only useful at late infection stages.[147] None of these techniques are good for monitoring the biofilm during treatment. Genetically engineered bioluminescent and fluorescent bacteria are promising for monitoring infection in animal studies but are limited exclusively to

research, and the signal depends upon many factors including cell count, metabolic rate, absorption and scattering in the tissue, and collection/emission optics.[229]

Herein we develop a technique to non-invasively image chemical concentrations on the surface of modified IMDs in order to detect, monitor, and study bacterial infections. We selected surface pH as our target analyte because infection and inflammation cause local acidosis, especially in dormant and poorly perfused regions near the implant surface.[158] For example, Hidalgo and coworkers used confocal microscopy together with ratiometric pH nanosensors to study pH gradients within both *E. coli* and wastewater biofilms.[162] Although the bulk pH was 7.2, the pH on the substrate surface was as low as 5.0 and varied with lateral position and depth. This heterogeneous pH is thought to play a strong role in antibiotic resistance, in part because the heterogeneous pH affects the antibiotic chemistry and bacterial metabolism, and in part because low pH is an indication of a poorly perfused region with likely lower antibiotic penetration and dormant bacteria.[230] Although quantitative pH images of the IMDs surface have not yet been acquired *in vivo*, indirect evidence strongly indicates a low surface pH. X-ray and MRI images show the effects of low pH on infected bone and teeth via erosion and formation of sinus tracts. In addition, spectroscopic techniques show the acid-generated change in mineral composition such as the presence of brushite and uncarbonated apatite materials in both cavities and infected bone.[231] Low pH *in vivo* is attributed to a combination of inflammation, osteoclast activity and bacterial metabolization.[6,232-234] For example, Konttinen and coworkers used pH microelectrodes to measure pH adjacent to a prosthetic hip implant intraoperatively.[6] For all measured patients, the pH in the nearby muscle,

gluteus medius was 7.39 +/-0.05. For patients with aceptic loosening, the pH was generally acidic and ranged between 5-7.5. This local acidosis is consistent with studies of collegen degradation, implant pitting, and metal ion release in patients with aseptic loosening.[232] The patient with septic loosening had a pH of 5.8 in the femoral stem and 4.4 in the femoral cavity. While these studies do not measure the average pH on the implant surface or generate pH images to study inhomogeneity, they do suggest significant drops in pH near an infected implant surface that should be measurable with our technique.

To study infections in situ, we designed a pH sensor film to non-invasively image through tissue the pH on the sensor surface with high spatial resolution using X-ray excited luminescence chemical imaging (XELCI). X-ray luminescence tomography (XLT) is a technique to image scintillators embedded in tissue at high resolution using a combination of X-ray excitation and optical detection.[137] By selectively irradiating the sample point-by-point or slice-by-slice, tomographic images of high quality could be constructed. Recently, the acquisition time for XLT has been greatly reduced via reconstructing high spatial image with mathematical methods, and the low background signal allows 3-dimensional reconstruction with as few as two angles.[235-237] Compared to XLT, XELCI provides more rapid measurements with surface-specific chemical sensing. The relatively thick and stable X-ray sensor film provides much greater luminescence than XLT for dilute nanoparticles and no background from out of focus slices. Our group has extended X-ray excited optical luminescence to spectrochemically measure pH without tissue and its high spatial resolution through tissue by irradiating two different

types of radioluminescent films embedded in tissue.[142] The ability of X-ray excited optical luminescence to study silver dissolution through tissue in one dimension was also demonstrated.[143] We also showed that hollow x-ray scintillators could be used to monitor drug release *in vitro* and the luminescent signal could be detected at one wavelength in living mice, however, luminescent signal was detected by only irradiating a single location in living mice (not a scanned or two dimensional image) and no in vivo drug release monitoring was achieved.[141]Herein, we extended our previous work and developed an XELCI technique to non-invasively map local pH variation due to bacterial metabolic activity in two dimensions through thick tissue with high spatial resolution. This is the first time that a 2D chemical image was acquired through tissue and the first time a reference region was used to account for the tissue induced spectral distoration. In the future, XELCI will be used to noninvasively monitor bacterial infection on implant surface in animal model with our own home-built system.

4.2 Results and Discussions

4.2.1 pH sensor film principle

Figure 4.1a shows the working principle of XELCI. The scintillators ($Gd_2O_2S:Eu^{3+}$ phosphors sealed in a PDMS layer) are excited by a narrow X-ray beam which generates a luminescent spot at a location and time controlled by the X-ray beam. The luminescence then passes through the pH indicator layer (silica containing bromophenol blue (BPB) dye), which alters the luminescence spectrum according to pH. The light finally passes through the tissue and is detected by an external spectrometer. A two

dimensional pH image is formed by scanning the sensor film in both x and y directions and determining pH from the luminescence spectrum at each position. The approach assumes that the tissue is relatively flat and homogeneous on the millimeter size scale. Figure 4.1b shows a photo of the X-ray source aiming at the sensor through porcine tissue. Figure 4.1c shows the luminescence spectrum (red line, plotted against the left y-axis). The intense peak at 620 nm is attributed to the $^5D_0 \rightarrow {}^7F_2$ transition of Eu^{3+}, while the near infrared emission at 700 nm arises from the $^5D_0 \rightarrow {}^7F_4$ transition of Eu^{3+}.[238] The BPB-doped silica film has a pH-dependent absorption spectrum, with an isobestic point indicating only two species, protonated and deprotonated (Figure 4.2a). Figure 4.2b shows a stretched calibration curve based on the absorption at the deprotonated peak, with a dynamic range between pH 4-9 indicating multiple environments within the film with different effective pK_as,[220,239] and 2-4% variation in absorbance at the deprotonated peak from film to film. As shown in Figure 4.1c, the absorption spectrum of the film at pH 7 overlaps more with the red (620 nm) luminescence of the scintillators than at pH 3, while the 700 nm peak is not absorbed by BPB at any pH and serves as an intensity reference to account for changes in X-ray intensity and optical collection efficiency.

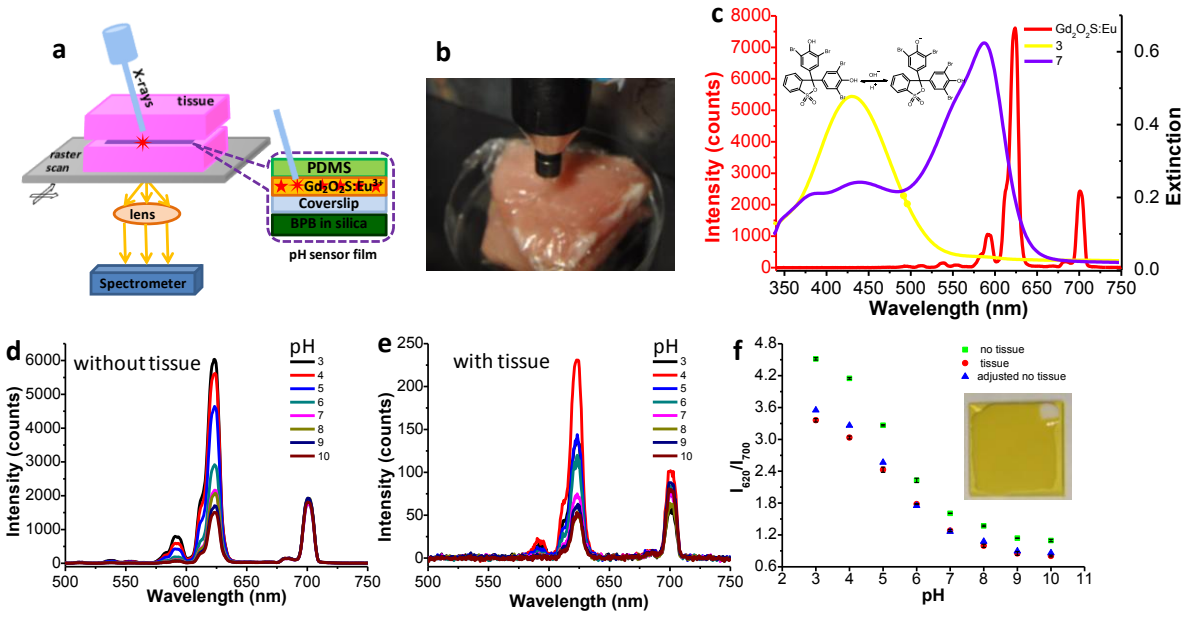

Figure 4.1 XELCI setup and pH calibration curves with and without tissue. (a) Schematic drawing of the XELCI setup. (b) Photograph of the setup. (c) Luminescent spectrum of scintillators (Gd_2O_2S: Eu^{3+}) (red line, left y-axis) and the extinction spectra of BPB-doped silica films in pH buffer 3.0 (yellow, right y-axis) and buffer 7.0 (purple, right y-axis). Inset: acidic and basic forms of BPB. (d) Luminescence spectra of pH sensor film in response to different standard buffers range from pH 3.0 to pH 10.0. (e) Luminescence spectra of pH sensor film in response to different pH buffers after passing through porcine tissue. (f) pH calibration curves without tissue (green squares), with tissue (red dots) and the adjusted no tissue calibration curve adjusted using the reference region (blue triangles). Error bars represent standard deviation of three different measurements. Inset: photograph of a pH sensor film with uncoated reference region (white region) on top right.

Table 4.1 The average ratio and standard deviation of the ratios for films without tissue. The standard deviation is defined as one standard deviation of three different measurements within one sample. The experiments were repeated at least five times. Below are typical results from one of experiments.

Standard buffers	Ratio average	Standard deviation of ratios
3.0	4.516	0.0238
4.0	4.146	0.0173
5.0	3.264	0.0118
6.0	2.228	0.0410
7.0	1.607	0.0037
8.0	1.370	0.0151
9.0	1.138	0.0049
10.0	1.095	0.0213

Table 4.2 The average ratio and standard deviation of the ratios for films with tissue. The standard deviation is defined as one standard deviation of three different measurements within one sample. The experiments were repeated at least five times. Below are typical results from one of experiments.

Standard buffers	Ratio average	Standard deviation of ratios
3.0	3.360	0.0332
4.0	3.034	0.0287
5.0	2.439	0.0488
6.0	1.782	0.0089
7.0	1.283	0.0220
8.0	0.9959	0.0288
9.0	0.8519	0.0357
10.0	0.8045	0.0167

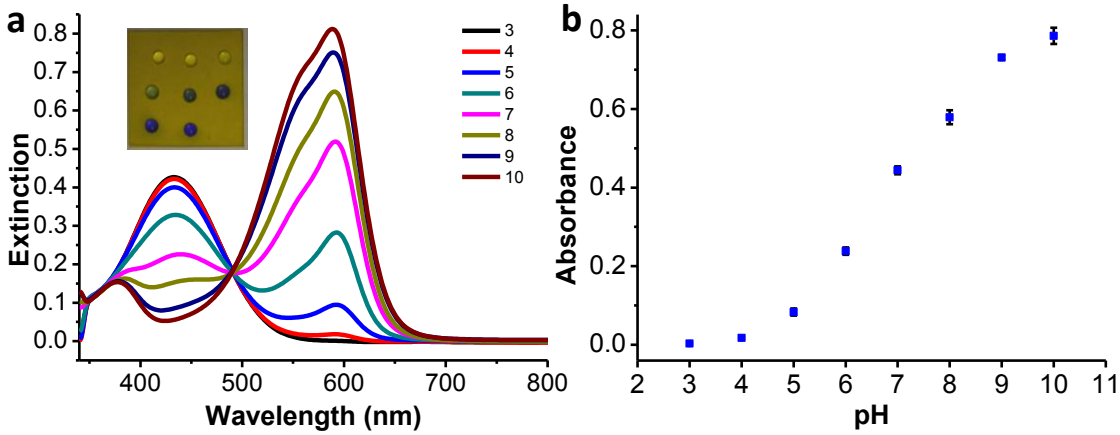

Figure 4.2. Absorbance spectra of BPB-doped silica film. (a) Typical UV-vis absorbance spectra of the BPB-doped silica film in response to standard buffers ranging from buffer 3.0 to buffer 10.0. Inset: A photograph of a BPB-doped silica film with different standard buffers. (b) Average absorbance of three different BPB-doped silica films at the deprotonated peak (595 nm) in response to different buffers. Error bars represent one standard deviation of of three different BPB-doped silica films.

4.2.2 pH calibration curves with and without tissue

We then studied how optical absorption and scattering in the tissue affect the luminescence spectra and pH calibration curves. Figure 4.1d shows the luminescence spectra of the pH sensor film in response to standard buffers ranging from pH 3.0-10.0. The same pH sensor film was then embedded between two slices of porcine muscle tissue and the experiment was repeated (Figure 4.1e). As is evident from Figure 4.1d and 4.1e, all the luminescence spectra are essentially background-free because tissue has a small X-

ray absorption cross-section and a very low radioluminescence conversion efficiency. The luminescence signal was attenuated 25 to 30 times after passing through tissue but still with an S/N between 10 and 28. A numerical analysis has demonstrated that nanoparticles with 0.4 pM concentration could be resolved in up to 2.25 cm tissue phantom using a 1 mm X-ray beam.[240] A numerical analysis has demonstrated that nanoparticles with 0.4 pM concentration could be resolved in up to 2.25 cm tissue phantom using a 1 mm X-ray beam.[240] Our sensor film consists of a much higher concentration of radioluminescent particles sealed in a robust PDMS layer. With an improved experimental setup and better optical collection efficiency, we believe XELCI will be capable of obtaining high spatial resolution image through soft tissue at least as deep as XLT does. Figure 4.1d and 4.1e also show that increasing the pH causes the luminescence intensity at 620 nm to decrease relative to that at 700 nm, as expected from the BPB absorption spectrum (see Figure 4.1c and Figure 4.2). Table 4.1 and 4.2 shows the actual values of the intensity ratio and standard deviations of the sensor film in response to different standard buffers without and with tissue. Figure 4.1f shows the 620 nm to 700 nm luminescence intensity ratio as a function of pH for a sensor film alone (green squares) and for the same film placed between two slices of tissue (red dots). The ratios decrease as pH increases for both without and with tissue, indicating that the pH sensor film is indeed pH responsive. However, at each pH, placing the sensor between the tissue slices decreases the 620 nm to 700 nm intensity ratio because the tissue absorbs more light at 620 nm than at 700 nm.[241-242] To determine how much the tissue distorts the spectrum, a region of the film was left without any pH-dye coating to serve as an in situ

spectral reference. A tissue factor of 1.27 was obtained for 700 nm/620nm light and this factor was used to correct the calibration curve without tissue (green squares). The corrected calibration curve (blue triangles in Figure 4.1f) overlaps well with the calibration curve acquired through tissue (red dots), indicating that the in situ reference accounted for most of the spectral distortion.

4.2.3 BPB-doped silica film characterization

To apply these sensors to monitor pH on IMDs, the sensor layer must be reversible with a response time shorter than the pH changes due to bacterial growth. Figure 4.3a shows the real-time response of the pH films to alternate cycled PBS (pH 7.4) and standard buffer 5. Nearly the same response was obtained for eight repetitions with no evidence of degradation, indicating good reversibility. The response time is about 30 s for a 90% change, which is similar to the result reported from literature for dye-doped silica films.[220] This response time is sufficiently fast to study bacterial growth mediated pH variation in real time which is expected to change over the course of hours.[239] We also studied the sensor stability against leaching. The leaching curves for the BPB-doped silica films in standard pH 5.0 buffer and in PBS (pH 7.4) are shown in black squares and red dots in Figure 4.3b. In pH 5 buffer, there was no BPB leaching for more than 20 days. However, in PBS, there was no significant BPB leaching (~1% or less) for the first three days (inset figure in Figure 4.3b), followed by increasing leaching over the next 10 days. This leaching behavior in PBS is probably due to the dissolution of silica at slightly basic pH 7.4. Indeed, the dissolution of silica-based HPLC column in phosphate buffer pH 7.0

has been observed before.[221] The stability of the BPB-doped film is sufficient to test the principle here, although not yet for long term in vivo detection. In future, we will incorporate the pH indicators to poly (ethylene glycol)-diacrylate hydrogels[9] or titania[243] to improve the sensor stability and biocompatibility.

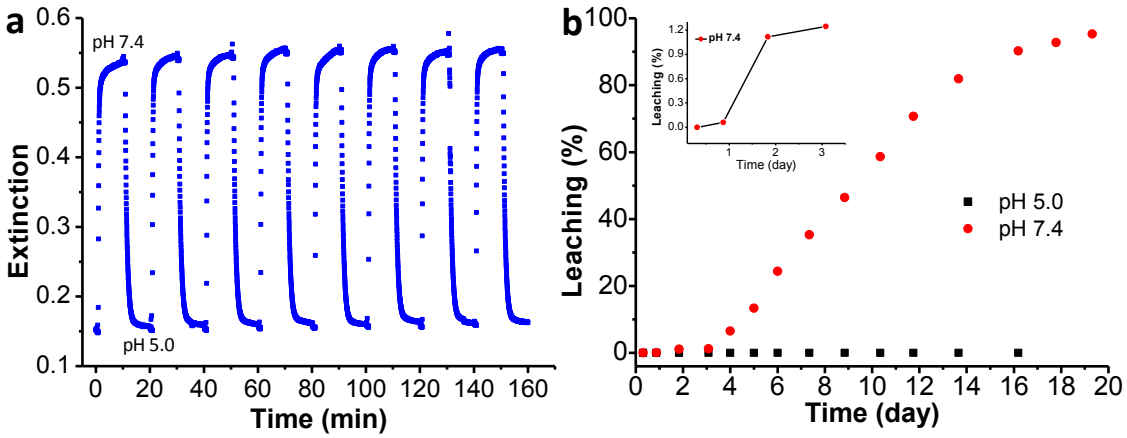

Figure 4.3 Characterization of BPB-doped silica film. (a) Real-time reversibility of BPB-doped silica film in response to pH 7.4 and pH 5.0, alternatively, by measuring the absorbance at 595 nm.(b) Leaching study of BPB-doped silica films in pH 5.0 (black squares) and pH 7.4 (red dots). Inset: First three days of the leaching results for the BPB-doped silica film in pH 7.4.

4.2.4 XELCI spatial resolution

Our goal is to use the pH sensor films to map pH variation caused by bacterial growth on the IMDs surface with high spatial resolution in situ. Our hypothesis, as shown in Figure 4.4a, is that the spatial resolution of XELCI is essentially limited by the X-ray beam size because a narrowly collimated X-ray source only generates light in the excited

spot. This is unlike a scanning fluorescence excitation mode where a large field of view is excited because the tissue scatters the excitation beam (typical photon mean free path is ~ 100 μm for red light).[164,242,244] After passing through tissue, a point light source will become approximately as large as the thickness of the tissue under optimal conditions.[165] By contrast, X-rays scatter far less by tissue than optical photons. The luminescence is generated only from the narrow path of the X-ray beam as X-rays have relatively small scattering coefficients in soft tissue (~0.14-0.87 cm^{-1}, depending on the X-ray energy), thus the beam maintains focus through several centimeters of tissue. For example, For 30 keV X-ray photons, the 1/e scattering depth (i.e. $1/\mu_s$) in soft tissue is 4.3 cm, which means that 87% of the incident photons travel ballistically through 6 mm of tissue. The other 13% scatter according to the Klein-Nishina equation, with about 6% back scattered and 7% forward scattered. The forward scattered X-rays irradiate the film as a diffuse halo over a ~ $(6\ mm)^2$ and create a background signal. For a 1.5 mm X-ray beam, the focused spot of ballistic X-rays will be approximately two hundred fold more intense over a smaller region than the background, thus the image contrast will not be significantly affected by scattering. In addition, ~10% of the photons that are absorbed by the tissue and do not reach the scintillators regardless of scattering. Higher energy X-rays will absorb and scatter even less. As shown in Figure 4.5, the illumination spots of the X-ray beam with or without passing through tissue are essentially identical in size. Hence, X-rays stay focused after passing through thick tissue and the spatial resolution is primarily dictated by the X-ray beam size.

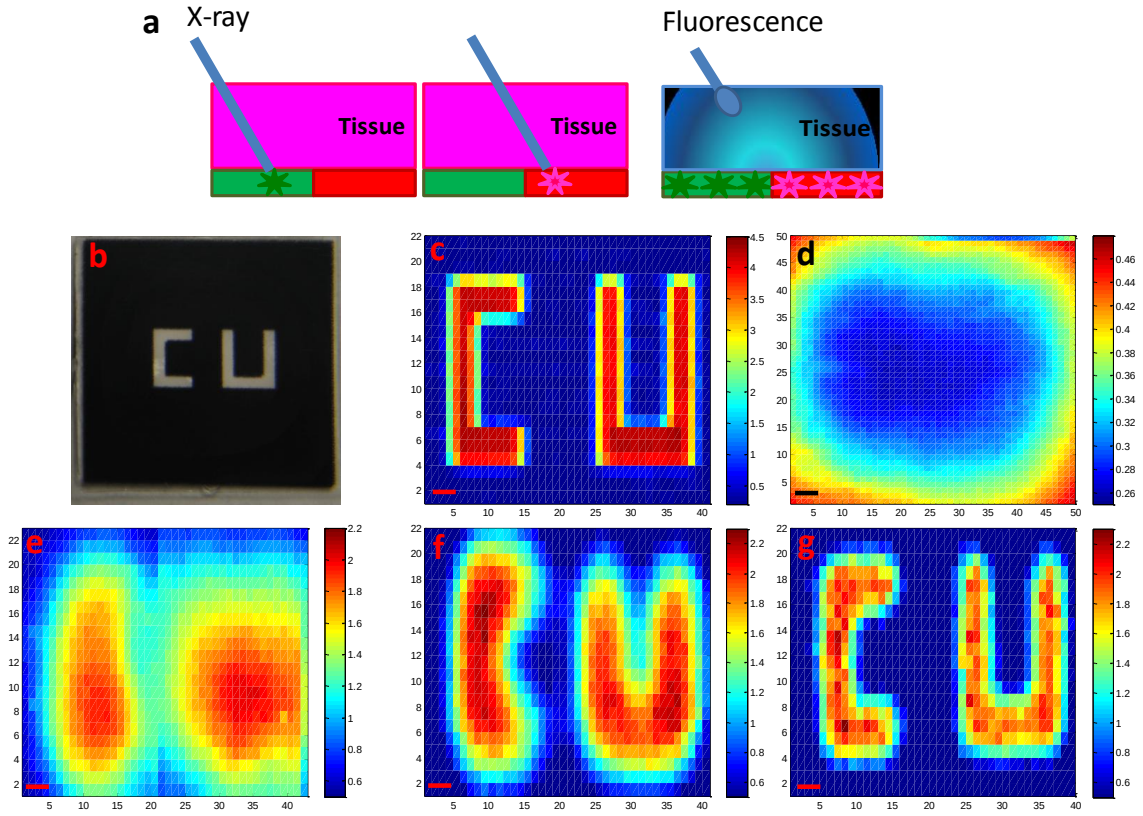

Figure 4.4 Spatial resolution of XELCI. (a) Working principle of XELCI versus fluorescence tomography. (b) Photograph of "CU" (target) on transparency. (c) Target mapping without tissue, irradiated with 1.5 mm X-ray beam. (d) Target mapped through tissue with white light as the illumination source. (e) Target mapped through tissue, irradiated with 3 mm X-ray beam. (f) Target mapped through tissue, irradiated with 1.5 mm X-ray beam; (g) Target mapped through tissue, irradiated with 1 mm X-ray beam. The color bars on the right are the ratios of the peak intensity at 620 nm over that at 700 nm. The x and y axis in c-g represent position. Step size=300 μm, scale bar= 1 mm.

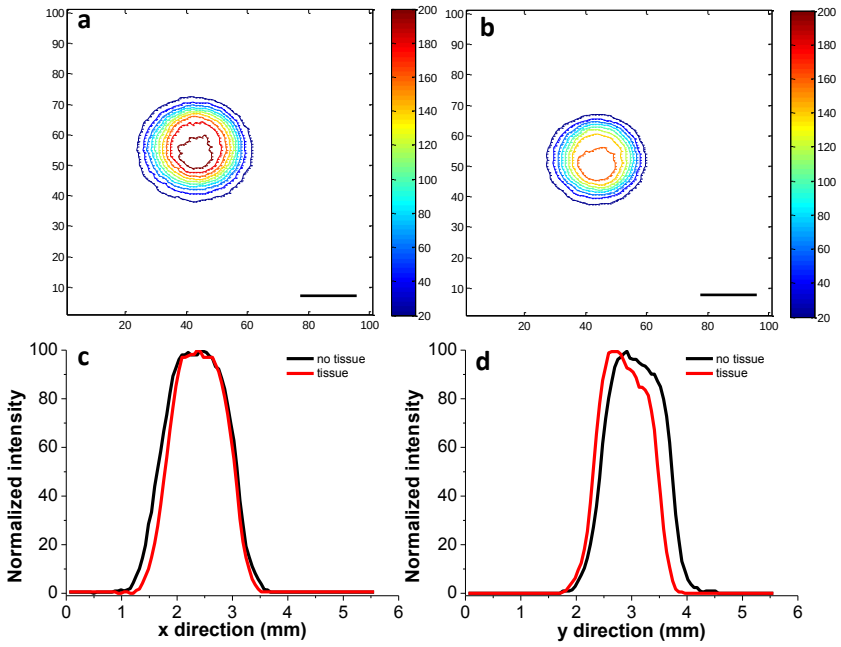

Figure 4.5 Size of the X-ray illuminated spot with or without passing through tissue. (a) Intensity contour plot of red X-ray excited optical luminescence, showing the size of luminescence spot on the Gd_2O_2S: Eu^{3+} film, irradiatated with a 1.5 mm X-ray beam. (b) Size of luminescence spot on the Gd_2O_2S: Eu^{3+} film, irradiatated with a 1.5 mm X-ray beam passing through 6 mm of porcine muscle tissue. (c) Intensity profiles of the illuminated spots in A and B along the x direction. (d) Intensity profiles of the illuminated spots in A and B along the y direction. Scale bar=1 mm.

4.2.5 "CU" target mapping

To further verify that our technique can detect the luminescence signal with high spatial resolution through tissue, primarily limited by the size of the illumination source, we used XELCI to map a target through tissue. The target was a transparency with a "CU" pattern (1 mm line width) printed in black ink that absorbs more light at 620 nm than 700

nm (see Figure 4.4b). We placed the target over a scintillator film and mapped the ratio of 620 nm to 700 nm X-ray excited luminescence. We first mapped the XELCI ratio without tissue using a 1.5 mm X-ray beam (Figure 4.4c), and then with the target embedded in tissue using nominal X-ray beam widths of 3 mm (Figure 4.4e), 1.5 mm (Figure 4.4f), and 1 mm (Figure 4.4g); these nominal widths were determined from the beam profiles (the width at 20 % of the maximum intensity) shown in Figure 4.6. Using a 3 mm beam, two objects are evident but their shape could not be resolved (Figure 4.4e). Mapping with a 1.5 mm X- ray beam could identify the two letters with a little image blurring while mapping with a 1 mm X-ray gave the best resolution. We chose 1.5 mm X-ray beam as the excitation source for the following experiments as a compromise between resolution, intensity and scanning time. To show the advantages of XELCI compared to conventional transmitted light imaging through tissue, we also acquired a ratio image of the same target but mapped through tissue using the microscope head lamp as the light source (Figure 4.4d). No indication of letters could be seen and only significant features come from light diffusing through from the edges of the target. The high spatial resolution of XELCI not only enables high resolution pH mapping, but also provides the ability to detect multiple analytes using different sensors at different locations and use local reference regions as intensity and spectral standards to account for spectral distortion in the tissue.

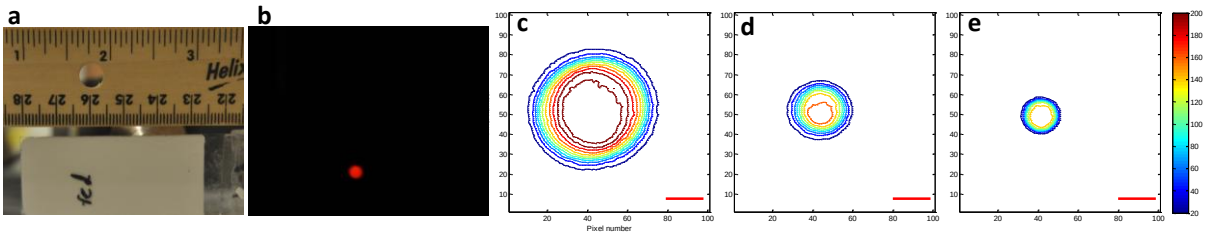

Figure 4.6 X-ray beam width. (a) Photograph of the setup for measuring X-ray beam sizes with room light on and X-ray off. (b) Photograph of the scintillator film, irradiated with a 3 mm X-ray beam with room light off. Red spot is from X-ray excited optical luminescence. (c) Zoom-in contour plot of red luminescence intensity from the scintillator film irradiated with a 3 mm X-ray beam. (d) Zoom-in contour plot of red luminescence intensity from the scintillator film irradiated with a 1.5 mm X-ray beam. (e) Zoom-in contour plot of red luminescence intneisty from the scintillator film irradiated with a 1 mm X-ray beam. Scale bar=1 mm.

4.2.6 pH imaging during bacterial growth

We then applied XELCI to map through tissue the pH decrease caused by bacterial growth on the interface between our pH sensor films and TSA plates (sensor surface). *Staphylococcus epidermidis (S. epid.)* was chosen as the model bacterial species as it is notorious for nosocomial infections.[198,226] We selected two strains, ATCC 12228 and ATCC 35984, to show generality. Figure 4.7a is a typical photograph of a pH sensor film on the TSA plate inoculated with *S. epid.* 12228. The sensor film turned from purple to yellow where there was growth. The color change was attributed to bacterial metabolism which generates acidic species and lowers the local pH.[158,239] Then, we mapped the

sample through tissue with XELCI. Figure 4.7c is the ratio image of the bacterial region after being grown for 2 h, and Figure 4.7d is the ratio image of the same region 3 h later. The pH was calculated by referring to the external pH calibration curve and the nearby reference region (Figure 4.7b). Specifically, the tissue effect on the 620 nm/700 nm peak ratio was first calculated by dividing the ratio of the 620 nm/700 nm of a bare luminescent film by the average of four points from the center of the reference region with a variance of 1-4% (Figure 4.7b). All the ratios were then adjusted with the tissue effect and the pH values were calculated by referring to the external pH calibration curve shown in Figure 4.1f (green square). For a control experiment, sterile PBS was added instead of the bacterial solution. Figure 4.8a is a photograph of the control plate. Figure 4.8b and 4.8c are the ratio images of the reference region and the sample region, respectively. The pH was calculated the same way as discussed above and the pH for the sterile film was 7.0 ± 0.2 throughout the image and the film was purple (neutral) after removal from tissue. We observed similar results using a different bacterial strain, *S. epid.*35984. Figure 4.9A is a photograph of the plate after being incubated with *S. epid.*35984 for 10 h and Figure 4.9b is the ratio image of the reference region. Figure 4.9c and 4.9d are the ratio images of the bacterial region mapped at different time points. A pH decrease over time was also seen through tissue with high spatial resolution. These results are representative of multiple experimental repetitions (at least 6), where pH consistently decreased to 5-6 within 4 h after culturing. Our approach is geared towards studying the biofilm rather than quantifying total number of colony forming units (CFU).

We hope to correlate pH with the concentration of bacteria and gene expression activity using bioluminescent transfected bacterial strain in the future.

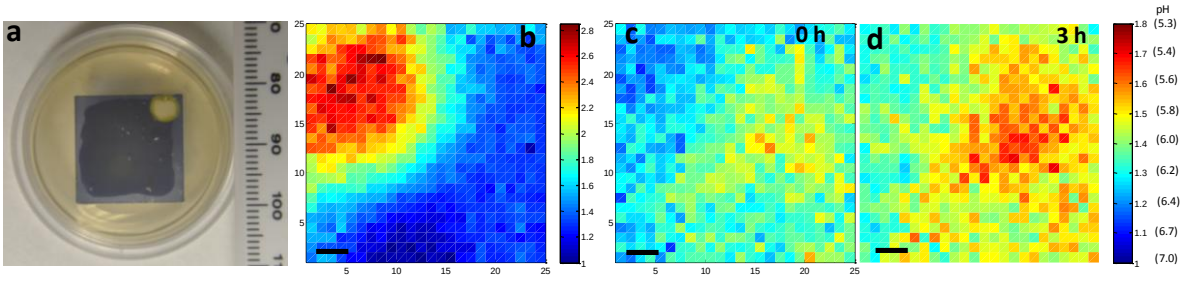

Figure 4.7 pH mapping of *S. epid.* 12228 growth through tissue. (a) Photograph of the sample after *S. epid.* 12228 grew for 2 h at the interface of the pH sensor film and the TSA plate at 37 ^{o}C. (b) Ratio map of the reference region. The XELCI images appear to be mirror images of the photographs because the XELCI images were viewed from below. (c) Ratio map of the sample region after 2 h growth. (d) Ratio map of the same region 3 h later. The color bars on the right are the ratios of the peak intensity at 620 nm over intensity at 700 nm. The x and y axis in b-d represent position. Step size=300 μm, scale bar=1 mm.

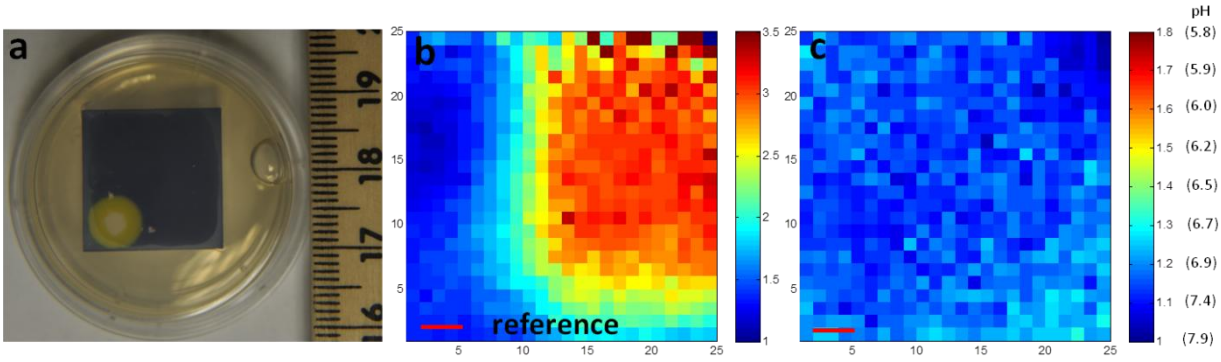

Figure 4.8 PBS control mapping. (a) Photograph of the TSA plate added with PBS as control before ratio mapping. (b) Luminescence ratio (620/700 nm) of the reference region, mapped through tissue. The XELCI images appear to be mirror images of the photographs because the XELCI images were viewed from below. (c) Ratio and pH map of the region where PBS was added, measured through tissue. Mapped area is 7.5 mm x 7.5 mm; step size=300 μm; scale bar=1 mm; color bar=620 nm/700 nm. The pH values are calculated by referring to the external pH calibration curve and adjusting using the reference region spectrum to account for spectral distortion in the tissue.

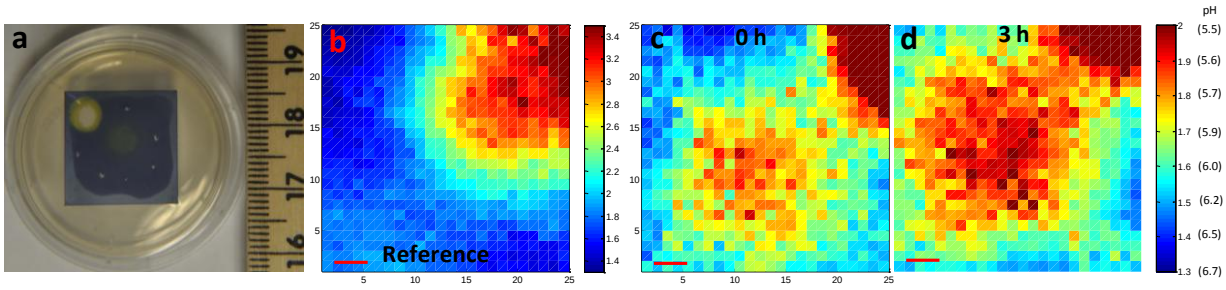

Figure 4.9 pH mapping of *S. epid.* 35984 growth through tissue. (a) Photograph of the TSA plate with *S. epid.* 35984 being grown at the interface of pH sensor film and TSA for 10 h before the first ratio mapping. (b) Ratio of the reference region, mapped through tissue. The XELCI images appear to be mirror images of the photographs because the XELCI images were viewed from below. (c) Ratio and pH map of the sample region where *S. epid.* 35984 has grown for 10 h at the interface of pH sensor film and TSA plate, measured through tissue. (d) Ratio and pH map of the same region 3 h later. The x and y axis in b-d represent position. The mapped area is 7.5 mm x 7.5 mm; step size=300 μm; scale bar=1 mm; color bar=620 nm/700 nm. The pH values are calculated by referring to the external pH calibration curve and correcting for spectral distortion using the reference region.

4.2.7 pH imaging during antibiotic treatment

We next exposed bacteria to antibiotics to watch their effect on the local pH. We chose *S. epid.* 12228 as a representative bacterial strain, and chose ciprofloxacin (cipro), a DNA gyrase inhibitor, as a typical antibiotic.[245-246] Figure 4.10b is a representative photograph

of *S. epid.* 12228 grown on the sensor surface; an acidic region is visible after 2 h of incubation. Figure 4.11a shows the luminescence ratio map of the film through tissue after 2h of bacterial growth. The color bar also indicates the corresponding pH calculated with the external calibration curve and the reference region (Figure 4.10a). Figure 4.11b, 4.11c and 4.11d are the ratio maps of the same region 3 h, 6 h and 18 h after cipro addition, respectively. We can see that the size of acidic region shrunk and the pH became more neutral, due to reduced metabolic activity and buffering from the agar gel. This was further verified through the photograph of the film after removal from tissue 18 h after cipro addition, Figure 4.10c. The yellow spot largely shrunk and the whole film returned to purple color, indicating neutral pH color. It is evident that the effect of antibiotics on local acidosis could be monitored through tissue with high temporal and spatial resolution. The effect of cipro on the growth of S. *epid*. 12228 was repeated multiple times (at least six), and a gradual pH restoration within 4 h after the addition was consistently observed.

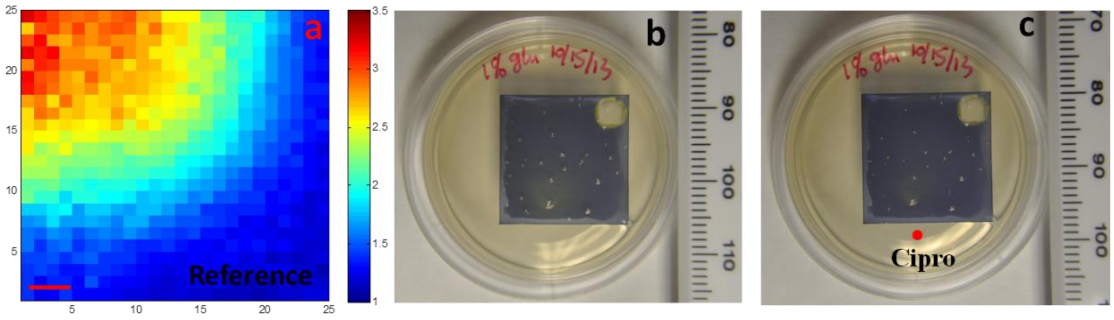

Figure 4.10 Reference region mapping and photgraphs of the sample before and after antibiotic addition. (a) Ratio map of the reference region for Figure 4.11. The color bar on the right is the ratio the peak intensity at 620 nm over that at 700 nm. The XELCI images appear to be mirror images of the photographs because the XELCI images were viewed from below. The scale bar represents 1 mm. (b) Photograph of the TSA plate with pH sensor film after *S. epid.* 12228 being grown for 2 h before the first ratio mapping in Figure 4a. (c) Photograph of the plate 18 h after ciprofloxacin (cipro) addition.

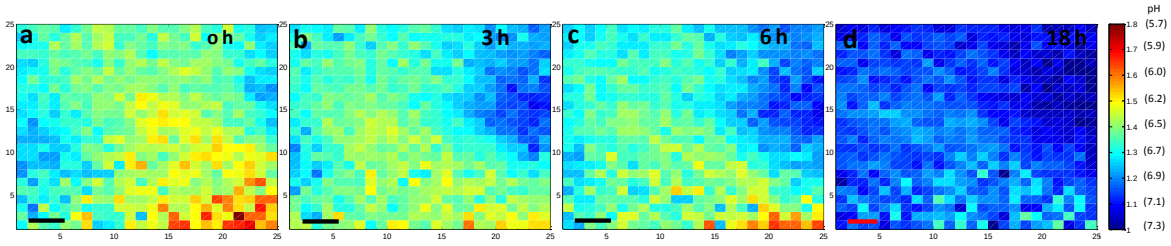

Figure 4.11 pH map of *S. epid.* 12228 during antibiotic treatment. (a) Ratio map of the sample region where *S. epid.* 12228 has been grown for 2 h at 37 ^{o}C before Cipro addition. (b) Ratio map of the same region 3 h after the Cipro addition. (c) 6 h after Cipro addition. (d) 18 h after Cipro addition. The color bars on the right are the ratios of the peak intensity at 620 nm over intensity at 700 nm. The pH values are calculated by referring to the external pH calibration curve and the reference region in Figure S7a. The x and y axis represent position. Step size=300 μm; scale bar=1 mm.

4.3 Conclusion

In conclusion, we constructed pH sensor films using a pH indicator dye to modulate the luminescence spectrum of X-ray scintillators. Employing X-rays as the excitation source provides high tissue penetration depth with minimum beam broadening and negligible autofluorescence background. By collimating the X-ray beam and scanning the sample point-by-point, an image mapping of the "CU" letter was obtained through thick tissue with high spatial resolution. Using XELCI, we imaged through porcine tissue the pH decrease during *S. epid.* growth and the pH restoration after application of antibiotics. These proof-of-principle experiments demonstrate the great potential of our technique in detecting bacterial infection and evaluating treatment on IMDs *in vivo* in biomedical

field. Future work involves developing a dedicated imaging system with higher spatial resolution, modifying dynamic compression plate surfaces for pH detection, and performing experiments on small animals.

4.4 Experimental Section

Materials: Bromophenol blue (BPB), tetramethoxyl orthosilicate (TMOS) and methyltrimethoxysilane (MTMOS) were all purchased from Alfa Aesar (Ward Hill, MA). Carboxymethylcellulose (CMC) and microcoverslips (#1, 18 mm x 18 mm) were purchased from Fisher Scientific (Pittsburgh, PA). Europium ions doped gadolinium oxysulfide scintillators (Gd_2O_2S: $Eu^{3+)}$ were purchased from Phosphor Technology (England). D (+) Glucose was purchased from Sigma-Aldrich (Saint Louis, MO). Polydimethylsiloxane (PDMS) base and its curing agent were purchased from Dow corning (Midland, MI). Porcine tissue (Smithfield boneless center, thick cut chops) was purchased from a local Walmart store and was sliced to 6 mm pieces using a meat slicer (Chef's Choice international, Graef 630). Hydrochloric acid (2 N) and standard pH buffers were purchased from BDH (West Chester, PA). Reagent alcohol, tryptic soy broth (TSB) and tryptic soy agar (TSA) were ordered from EMD (Gibbstown, NJ). *Staphylococcus epidermidis* 12228 (*S. epid.* 12228*)* and *Staphylococcus epidermidis* 35984 (*S. epid.* 35984) were purchased from ATCC (Manasssas, VA). Transparencies (3M, CG6000) were purchased from Amazon.

Preparation and Characterization of BPB-doped Silica film: Organically modified silica films doped with BPB were prepared according to our previous methods with minor modifications.[220,239] Specifically, TMOS (320 μL) and MTMOS (138 μL) were mixed in ethanol (228 μL). Then, an appropriate amount of distilled water was added to maintain the molar ratio of silane over H_2O to be 1:4, HCl (0.1M, 166 μL) was then added to initiate the polymerization. BPB (25 mg) was added subsequently. The mixture was sealed and stirred at room temperature for 24 h. Then, an aliquot of the mixture (40 μL) was spread onto a precleaned microcoverslip for 20 s and then spun cast at 2500 rpm for 15 s to form a transparent and uniform silica film. These films were dried at room temperature with a relative humidity of 40 % for 2 days. Then, the BPB-doped films were activated in 1x PBS overnight for further experiments. To measure the absorbance spectra of BPB-doped silica films in response to different pH, three films were immersed to different standard buffers ranging from 3.0 to 10.0 for 30 min. The absorbance spectra were taken with a UV-2101pc spectrometer (Shimadzu, Torrance, CA) with the respective standard buffers as references. The average absorbance at different pH was shown in Figure S1b and the error bars correspond to ± 1 standard deviation. To study the reversibility of the BPB-doped silica films, one of the BPB-doped films was fixed to a Petri-dish bottom and mounted to a Leica microscope stage (Leica DMI 5000M, Wetzlar, Germany). The absorbance variations in response to alternate pH 5.0 and 1x PBS (7.4) were recorded in real time with the microscope head lamp (tungsten filament) as the light source. The spectra were recorded with an acquisition time of 0.1 s in every 2 s for 10 min.

pH sensor film preparation: pH sensor films were prepared with the following procedures. First, Gd_2O_2S: Eu^{3+} (1 g/mL) was prepared by dispersing an appropriate amount of scintillators in 0.5 % CMC. Then, 100 μL of the solution was spread onto the other side of the BPB-doped silica films. After being dried at room temperature overnight, PDMS with a base to curing agent ratio of 10:1 was spread onto the surface of the scintillators to fix them in position. The PDMS layer was cured at room temperature for 2 d. To create a local reference region, a small square (~2 mm) of BPB-doped silica film was removed and then PDMS was spread onto the blank region.

Measurement of X-ray beam sizes: The sizes of the X-ray beams were measured with the setup shown in Figure S4a. Specifically, a scintillator film was irradiated with an X-ray beam amounted with different collimators and images were captured with a Nikon camera (D90, Japan). An image of a ruler was also taken with the same setup with room light on. The red components of the images were analyzed with Matlab and the widths at 20% of the maximum intensity were determined to be the X-ray beam widths. To study the tissue effect on beam broadening, a piece of porcine tissue (6 mm) was placed in front of the X-ray beam (1.5 mm) before it irradiated the scintillator film and an image was also obtained with X-ray on and room light off. All the images were analyzed with Matlab to calculate X-ray beam sizes.

Luminescence acquisition: The luminescence spectrum of Gd_2O_2S: Eu^{3+} was obtained with the setup displayed in Figure 1a. The sample was irradiated with a mini X-ray tube (Amptek Inc. MA, USA), operating at a tube voltage of 40 kV and a tube current of 99 μA. Different X-ray beam sizes were achieved by mounting different collimators (brass)

to the tip of the X-ray tube. The luminescence was collected with a 10x objective lens under dark field mode. The luminescence was then dispersed by a spectrometer (DNS 300, DeltaNu, Laramie, WY) with a 150 lines/mm grating and collected with a cooled CCD camera (iDUS-DU420A-BV, Andor, South Windsor, CT), set to 100 kHz transfer such that each digital count corresponded to 15 photoelectrons. The spectra were recorded with Andor's Solis software with an acquisition time of 1 s otherwise indicated.

Target mapping: The target, "CU" letters in white, with a line width of 1mm and a space of 2 mm between lines in an 18 mm x 18 mm black background, was printed onto the rough side of a transparency twice with ink jet ink (photo black, Nano Digital), using an epson stylus photo R200 ink jet printer. The target was then attached to one side of a microcoverslip with PDMS. The other side of the microcoverslip was deposited with 100 µL of Gd_2O_2S: Eu^{3+} (1 g/mL in 0.5 % CMC) and PDMS sequentially. The target was first mapped without tissue, irradiated with a 1.5 mm X-ray beam. Then, it was sandwiched between two pieces of porcine muscle tissue and mapped with 3 mm, 1.5 mm and 1 mm X-ray beams as excitation sources, respectively. For collecting luminescence spectra point-by-point, the target was first placed onto the microscope stage and moved with a step size of 300 µm horizontally and vertically in a raster mode. The movement of the stage was controlled with an HCI image software. The luminescence was collected kinetically at the same time with an Andor software. The synchronicity was achieved by correlating the HCI image with the Andor acquisition software. For mapping the target with white light source, no scintillators were deposited on the other side of the target and the microscope head lamp (tungsten filament) was used as the illumination source. To

create a ratio-mapping image, the data acquired were analyzed with a written Matlab script. Specifically, the peak intensity at 620 nm and that at 700 nm was obtained from all the spectra and then the ratios of the peak intensity at 620 nm over that at 700 nm were calculated. The ratios were then plotted with the pcolor function built in Matlab.

Bacterial culture and pH mapping through tissue: Fresh cultures of *S. epid.*12228 and *S. epid.* 35984 were prepared according to our previous procedure.[239] Specifically, a single *S. epid.*12228 or *S. epid.* 35984 colony from a TSA plate streaked less than a week was inoculated to sterile TSB (5 mL). Bacteria were grown to the stationary phase under shaking at 37 ^{o}C for 16-18 h. The fresh culture was then washed with sterilized PBS twice and dispersed in sterilized PBS (5 mL). The number of bacteria was quantified by measuring the optical density at 600 nm (Smartspec 3000, Bio-Rad). The concentration of bacteria was then diluted to 10^7 cells/mL with sterilized PBS. This bacterial solution (2 μL) was spotted to a small TSA plate supplemented with 1 % glucose. Glucose concentrations between 0.25%-4% (w/w) are widely used for culturing biofilms in the absence of a circulatory or flow system.[247-248] The pH sensor film was then laid on top of the TSA plate after the bacterial spot dried. The plate grown with *S. epid.*12228 was left grown at 37 ^{o}C for 2 h, while the plate inoculated with *S. epid.* 35984 was grown for 10 h at 37 ^{o}C. A photograph of the TSA plate was taken with a Nikon camera (D90, Japan) before it was sandwiched between two pieces of tissue (6 mm) for radioluminescence acquisition. Both the region where the bacteria were spotted and the reference region were mapped sequentially with the same setup described in the target mapping section. The region with bacteria was also mapped again 3 h later. For a control study, sterilized

PBS (2 μL) was added instead of bacterial solution. After incubation at 37 ^{o}C for 10 h, the region where PBS was added and the reference region were mapped through tissue using the same method. The ratio of the peak intensity at 620 nm over that at 700 nm was calculated with the same Matlab script as in the target mapping section. The corresponding pH was calculated by referring to the external pH calibration curve and the reference region to account for the tissue effect.

Antibiotic effect study: *S. epid.* 12228 was chosen as a model to study the effect of antibiotic on the bacterial growth. A fresh culture of *S. epid.*12228 was prepared as described above. The culture was also washed with PBS twice and diluted to a concentration of 10^7 cells/mL. Then, this bacterial solution (2 μL) was spotted to a TSA plate (1% glucose). A pH sensor film was placed after the spot dried. The whole TSA plate was incubated at 37 ^{o}C for 2 h for the bacteria to grow. A photograph of the TSA plate was obtained before the bacterial spot was mapped through porcine tissue (6 mm) with the method described in the above bacterial culture and pH mapping through tissue section. The whole mapping area was 7.5 mm x 7.5 mm (a 25x25 pixel field) with an increment of 0.3 mm. Then the reference region was also mapped with the same way. Afterwards, ciprofloxacin (1 μL, 1 mg/mL) was added onto the TSA plate at a distance of about 5 mm to the bacterial spot without in contact with the pH sensor film. The same bacterial spot was mapped again in 3 h, 6 h and 18 h, respectively. A photograph of the TSA plate with the pH sensor film was obtained after the last mapping. Data analysis was done the same way as in the above section.

CHAPTER 5. CONCLUSIONS AND FUTURE DIRECTIONS

In summary, we have described three different types of optical pH sensors based on nanoparticles and implantable films in this dissertation. These sensors were introduced to measure intracellular pH in living cells, monitor bacterial growth caused pH decrease through thick tissue and image bacterial growth and antibiotic treatment induced pH variation through thick tissue. These sensors have great potential to study pH-related cellular events and noninvasively monitor bacterial infection on IMDs in vivo.

In Chapter 2, we developed a pH nanosensor for detecting intracellular pH based on SERS. SERS based sensors are attractive because they have narrow, vibrationally specific spectral peaks that can be excited using red or near-infrared light which can avoid photobleaching and reduce autofluorescence. We described a SERS based pH nanosensor with high specificity and sensitivity by encapsulating 4-MBA functionalized silver nanoparticles in a 30 nm proton permeable silica shell. The pH nanosensor was demonstrated to be responsive to pH in the range of 3-6 with a noise level of less than 0.1 pH units. The silica-encapsulated 4-MBA functionalized silver nanoparticles (Ag-MBA@SiO_2) were taken up by J774A.1 macrophage cells and measured a decrease in local pH during endocytosis. One promising extension of this strategy is developing a sensor for measuring other small molecules (e.g. dopamine) with high specificity in complicated biological systems in situ. The detection of dopamine based on SERS has been studied using polymer coated silver electrodes and polymer coated fiber-optic probes.[66,179] The protein absorption interference was minimized with the introduction of polymers However, the size of the silver electrodes and fiber-optic probes, and the

requirement of other accessories make these sensors difficult for measuring dopamine concentrations noninvasively in situ. It is promising to design a nanosensor based on silica encapsulated silver nanoparticles for measuring dopamine concentrations in vivo. By tuning the silica pore size and thickness, a nanosensor with desirable response time, selectivity and sensitivity can be constructed. Another attractive application of our pH nanosensor is monitoring pH variation during cell (targeted) apoptosis. By coating another thin layer of APTES, the surface of the pH nanosensor could be functionalized with specific molecules such as folic acid to target cancer cells. The pH variation of these cancer cells in response to different weak acid, bases and metabolic inhibitors (ammonia, acidic ionophores X537A and nigericin) can be monitored in real time.[22] The pH change in response to different treatments such as chemotherapy could also be recorded in real time. This pH variation may provide useful information for studying cell apoptosis pathways and evaluating cancer treatment efficacy.

In Chapter 3, we developed an optical sensor film to detect local acidosis on a surface embedded in thick tissue. The sensor film was composed of both upconverting particles (UCPs) that served as a light source and a pH indicator that altered the luminescence spectrum. When irradiated with 980 nm light, the UCPs produced deeply penetrating red light emission, while generating negligible autofluorescence in the tissue. The basic form of the pH indicator absorbed more of upconversion luminescence at 661 nm than at 671 nm and consequently the spectral ratio indicated pH. pH calibration curves without and with 6-7 nm of porcine tissue overlapped very well because the two peaks are closely

spaced. Furthermore, the growth of *Staphylococcus epidermidis* caused local pH decrease on the sensor surface was noninvasively monitored in real time through 6-7 mm tissue.

In Chapter 4, we developed a pH sensor film that can be coated on an implant surface and imaged using a combination of X-ray excitation and visible spectroscopy to monitor bacterial infection and treatment on IMDs through tissue. The introduction of X-ray as a scanning excitation source allowed this technique to have high spatial resolution through thick tissue. The radioluminescence in the pH sensor film first passed through a layer containing pH indicator that modulated the spectrum according to pH, then passed through tissue where it was detected by a spectrometer. A reference region on the film was successfully used to account for spectral distortion from wavelength-dependent absorption and scattering in the tissue. pH images were acquired by moving the sample relative to the X-ray beam and collecting a spectrum at each location, with a spatial resolution limited by the X-ray beam width. Using XELCI to map pH through porcine tissue, we detected a pH drop during normal bacterial growth on the sensor surface, and a restoration of the pH to the bulk value during antibiotic treatment over the course of hours with millimeter resolution. Overall, XELCI provided a novel approach to noninvasively image surface pH to diagnose implant infection and assess treatment. The future directions of Chapter 3 and Chapter 4 are of several aspects.

The stability of the pH indicators doped silicate layer will need to be further improved. Currently, the silicate layer is stable for the first three days with minium dye leaching in PBS, however, there is an increased dye leaching after the first few days due to the dissolution of silica by PBS. The stability of these films were sufficient for test the proof

of principle of the projects developed in this dessertation. However, the long term stability of the pH sensitive layer is very important for future studies (animal models). Several approaches could be introduced to minimize or avoid indicator leaching. For instance, organically modified silicate sol gel together with ion-paired molecules were introduced to minimize the indicators from leaching and extend the sensor stability in PBS.[249] By adjusting the composition of organically modified sol gels, more stable and robust pH-responsive films could be prepared. Here are some preliminary results. First, pH-responsive films were prepared by doping pH indicators (bromocresol green) into organically modified sol gel. The sol gel was prepared by hydrolyzing GPTMS and MTMOS (1:1, mole ratio) in ethanol using HCl as the catalyst. pH-responsive films were fabricated by spin-coating the aged sol gel onto precleaned coverslips (#2, Fisher Scientific). The films were aged at room temperature for 24 h and then cured in an oven (105 ^{o}C) for 3 h. Figure 5.1 shows the reversibility of the films in response to alternating PBS and buffer 5, and the leaching stability of the films in both PBS and buffer 5. As shown in Figure 5.1A, the-pH responsive film was highly reversible. The response time from PBS to buffer 5 (90% response) was within 1 s, while the response time from buffer 5 to PBS (90% response) was calculated to be ~12 s. As shown in Figure 5B, the pH sensor films had an initial burst leaching within the first day for both buffer 5 and PBS. Then the leaching rate was very small for buffer 5, however, there was continuos diffusion caused indicator leaching in PBS. Then, pH responsive films with good reversibility and small leaching rate were prepared by increasing the ratio of MTMOS over GPTMS to 7:3. The film preparation processures were similar to the films prepared

with GPTMS and MTMOS in a 1:1 ratio. By increasing the amount of MTMOS, the hydrophobicity of the films increased, hence, the leaching rate decreased. Figure 5.2 shows both the reversibility and leaching stability studies. As shown in Figure 5.2A, the response time from PBS to buffer 5 and buffer 5 to PBS both increased to 30 s. This response time is still fast enough to study bacterial infection caused pH variation in vivo. As can be seen from Figure 5B, the film stability was greatly improved. Although there was a burst leaching within the first two days, there was only a 3% leaching from day 3 to day 12. These films can be preleached and used to monitor bacterial infection using an animal model.

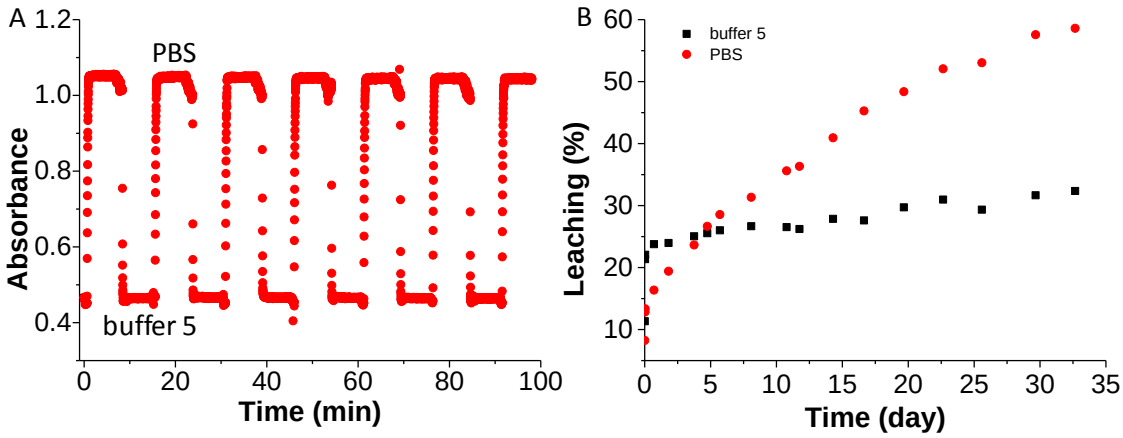

Figure 5.1 Characterization of pH sensor films (GPTMS:MTMOS=1:1, molar ratio) A. Real-time reversibility study of the pH sensor films in response to PBS and buffer 5, alternatively. B. Leaching study of the pH sensor film in PBS and buffer 5,

respectively.

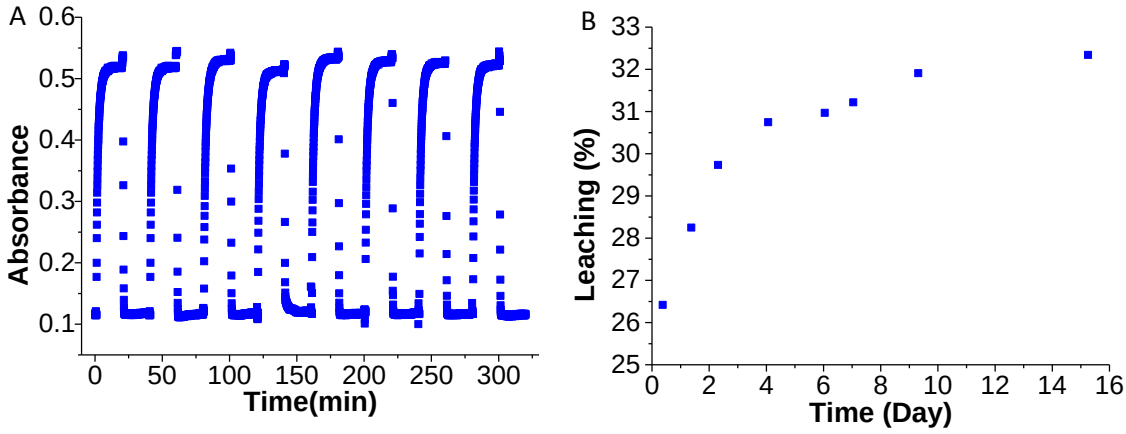

Figure 5.2 Characterization of pH sensor films (GPTMS:MTMOS=3:7, molar ratio) A. Real-time reversibility study of the pH sensor films in response to PBS and buffer 5, alternatively. B. Leaching study of the pH sensor film in PBS.

The film sensor stability could be further improved by introducing an proton ion selective membrane and polymeric matrix.[250] Another strategy to prevent indicator from leaching is covalently bonding the indicator to the polymer backbone. pH indicators such as bromocresol green were conjugated to functional silanes, which can be incorporated to the silicate films to prevent indicator from leaching. In addition, Hu et al. designed several types of pH sensor films based on PEG hydrogel. pH indictors (cresol red, 6,8-dihydroxypyrene-1,3-disulfonic acid) were covalently conjugated to methacrylic anhydride, which was then copolymerized with polyethylene glycol diacrylate monomer to form PEG hydrogel.[251] These pH sensor films were demonstrated to have minimum indicator leaching and PEG hydrogel based sensors films also have great

biocompatibility. These strategies could be introduced to prepare robust pH sensitive layers and avoid indictor leaching.

The biocompatibility of the pH sensor films will be evaluated with cells according to standard protocols before we implant our pH sensor films into animal models. The ability of the sensor film to monitor bacterial infection on the sensor surface in vivo will be investigated with an animal model. Briefly, the pH sensor films will be attached onto mimic implants using PDMS or biocompatible glues. Then, the modified implants will be implanted into an animal model to study bacterial infection in vivo. The luminescence signal will be collected using an in vivo imaging system. Here are some preliminary results we obtained using a rat carcass. The pH sensor films were prepared using a combination of radioluminescent particles and bromocresol green doped organically modified sol gel films (GPTMS:MTMOS=1:1). The pH sensor films were preleached in PBS for 24 h and then attached to a titanium disk (5 mm diameter) with radioluminescent particles using PDMS as a glue. The modified Ti disk was inserted into the biceps femoris region of the rat subcutaneously. The modified implant disk was excited with a collimated X-ray beam. Luminescent images were captured via an IVIS Lumina-XR imaging system (Caliper Life Sciences, Hopkinton, MA, USA) with two different filters, DsRed (575 nm-650 nm) and Cy5.5 (695 nm-770 nm). Figure 5.3 shows a typical set of images without or with rat acquired with the IVIS after the modified implant disk was incubated in standard buffer 7 for 10 min. Strong luminescent signals were obtained without or with rat. By taking the ratio of the luminescence signal obtained with DsRed filter over that obtained with Cy5.5 filter, a pH calibration curve was generated. Table 5.1

and 5.2 shows the actual values of the intensity ratio and standard deviations of the sensor in response to different buffers externally and subcutaneously implanted in a hind leg of a rat ex vivo. Figure 5.4 shows the calibration curves for the modified implant disk without rat or subcutaneously implanted into the rat. As is shown in Figure 5.4, pH calibration curves with small standard deviations were obtained both without and with rat. The modified implant disk was responsive to pH in the range of 4 to 7. In addition, the two calibration curves overlap well with a pH difference of ~0.2 units, which might be further improved with a reference disk consisted of radioluminescent particles only.

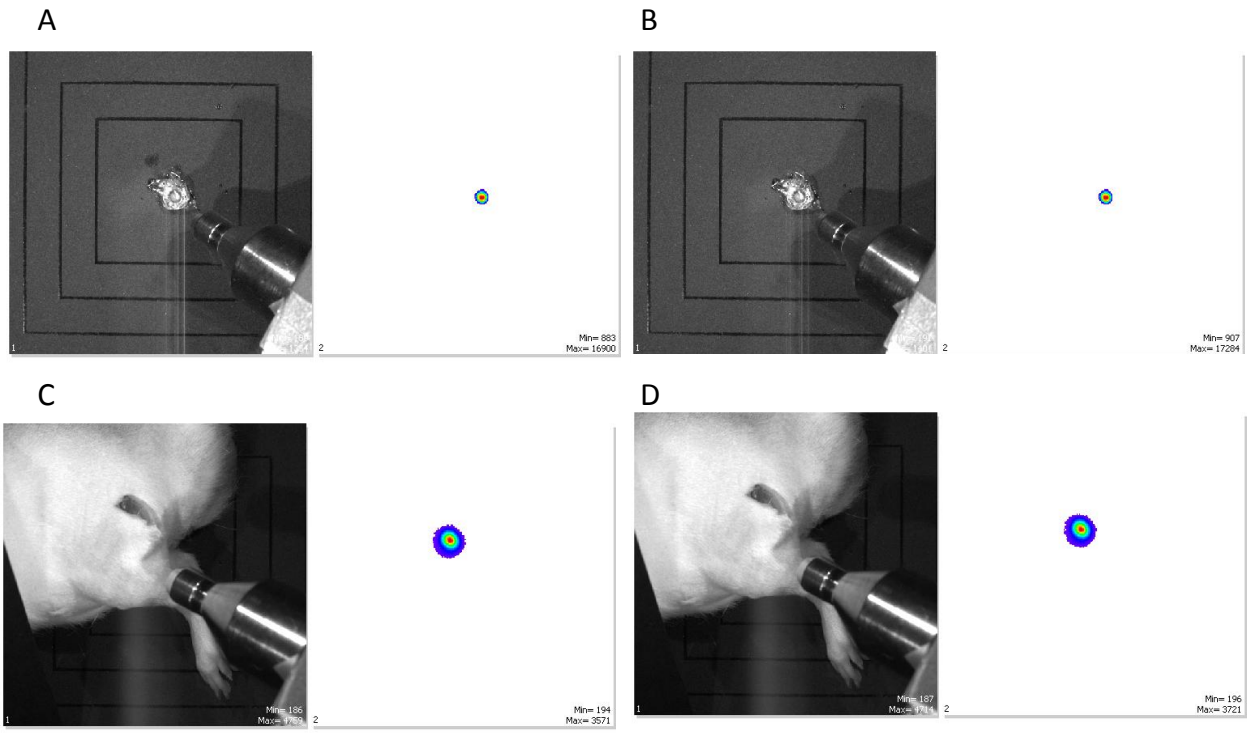

Figure 5.3 Typical IVIS images without or subcutaneously implanted into rat after modified implant disk was incubated at standard buffer 7. A. Photograph and luminescent images (with DsRed filter) without rat. B. Photograph and luminescent images (with Cy5.5 filter) without rat. C. Photograph and luminescent images (with DsRed filter) of the modified disk implanted in rat. D. Photograph and luminescent images (with Cy5.5 filter) of the modified disk implanted in rat.

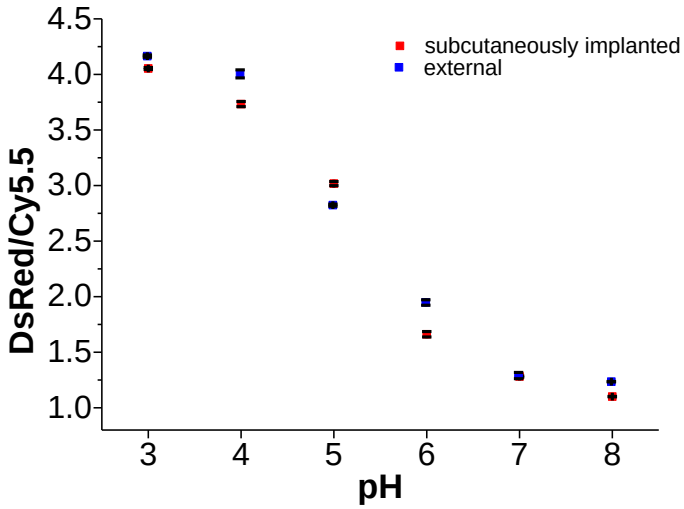

Figure 5.4 External pH calibration curve and pH calibration curve when the sensor film was subcutaneously implanted.

Table 5.1 Average and standard deviation of the ratios in response to buffers without tissue. The standard deviation is one standard deviation of three repetitive measurements of one sample. The experiments were repeated at least three times. Below are typical results from one of experiments.

Standard buffers	Ratio average	Standard deviation of ratios
3.0	4.176	0.0010
4.0	4.016	0.0361
5.0	2.834	0.0010
6.0	1.959	0.0242
7.0	1.301	0.0282
8.0	1.245	0.0022

Table 5.2 Average and standard deviation of the ratios of the film in response to buffers subcutaneously inserted. The standard deviation is defined as one standard deviation of three repetitive measurements within the same sample. The experiments were repeated at least three times. Below are typical results from one of experiments.

Standard buffers	Ratio average	Standard deviation of ratios
3	4.053	0.0089
4	3.733	0.0233
5	3.017	0.0184
6	1.662	0.0242
7	1.281	0.0060
8	1.100	0.0017

With these preliminary results, we believe a sensor modified implant could be designed to monitor pH variation on the surface using an animal model (rat) in vivo. In the future, a more dedicated home-built imaging systems will be designed to map bacterial effection and monitor treatment on modified implants in vivo with better signal collection effciency and good spatial resolution. Both upconverting and radioluminescent particles will be introduced as light sources to facilitate different data acquisition modes.

One challege for using pH as an indictor to monitor bacterial infection on IMDs is to distinguish imflammation from bacterial infection. Both imflammation and bacterial infection can cause local pH variation.[6,252] Multiplexing sensing strategies may increase the specificity of diagnosis. Niinikoski et al. studied the fluctuation of pH, CO_2 and O_2 using a standard wound infection model. They found that there was a distinct oxgen tension difference between the controls and the infected wounds.[253] Oxygen sensors and protease sensors will be designed with similar strategies to study oxgyen fluctuation and protease concentration on IMDs surface. The integration of different sensors (pH, oxygen, protease) may be capable of specifically detecting bacterial infection on IMDs.

Overall, with further improvements in sensor construction and instrumentation, we expect our SERS nanosensors and pH luminescent sensor films to provide useful information (infection diagnosis and treatment) for biomedical field.

APPENDICES

Appendix 1: Copyright Permission from the American Chemistry Society

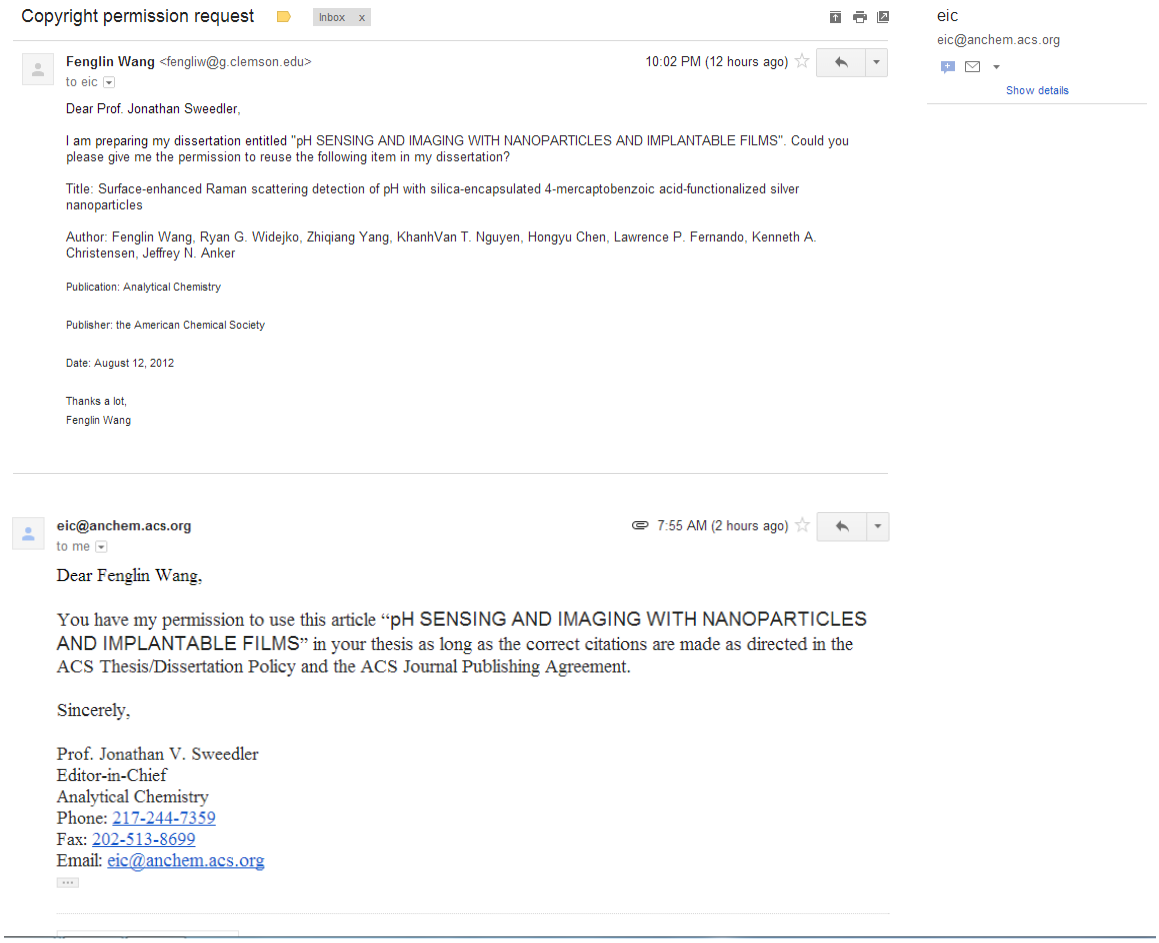

Copyright permission request Inbox x

Fenglin Wang <fengliw@g.clemson.edu> 10:02 PM (12 hours ago)
to eic

Dear Prof. Jonathan Sweedler,

I am preparing my dissertation entitled "pH SENSING AND IMAGING WITH NANOPARTICLES AND IMPLANTABLE FILMS". Could you please give me the permission to reuse the following item in my dissertation?

Title: Surface-enhanced Raman scattering detection of pH with silica-encapsulated 4-mercaptobenzoic acid-functionalized silver nanoparticles

Author: Fenglin Wang, Ryan G. Widejko, Zhiqiang Yang, KhanhVan T. Nguyen, Hongyu Chen, Lawrence P. Fernando, Kenneth A. Christensen, Jeffrey N. Anker

Publication: Analytical Chemistry

Publisher: the American Chemical Society

Date: August 12, 2012

Thanks a lot,
Fenglin Wang

eic
eic@anchem.acs.org
Show details

eic@anchem.acs.org 7:55 AM (2 hours ago)
to me

Dear Fenglin Wang,

You have my permission to use this article "pH SENSING AND IMAGING WITH NANOPARTICLES AND IMPLANTABLE FILMS" in your thesis as long as the correct citations are made as directed in the ACS Thesis/Dissertation Policy and the ACS Journal Publishing Agreement.

Sincerely,

Prof. Jonathan V. Sweedler
Editor-in-Chief
Analytical Chemistry
Phone: 217-244-7359
Fax: 202-513-8699
Email: eic@anchem.acs.org

Appendix 2: Copyright Permission from John Wiley and Sons

JOHN WILEY AND SONS LICENSE TERMS AND CONDITIONS

Nov 19, 2014

This is a License Agreement between Fenglin Wang ("You") and John Wiley and Sons ("John Wiley and Sons") provided by Copyright Clearance Center ("CCC"). The license consists of your order details, the terms and conditions provided by John Wiley and Sons, and the payment terms and conditions.

All payments must be made in full to CCC. For payment instructions, please see information listed at the bottom of this form.

License Number	3512491329357
License date	Nov 19, 2014
Licensed content publisher	John Wiley and Sons
Licensed content publication	Advanced Healthcare Materials
Licensed content title	Development of Luminescent pH Sensor Films for Monitoring Bacterial Growth Through Tissue
Licensed copyright line	Copyright © 2014 WILEY-VCH Verlag GmbH & Co. KGaA, Weinheim
Licensed content author	Fenglin Wang,Yash Raval,Hongyu Chen,Tzuen-Rong J. Tzeng,John D. DesJardins,Jeffrey N. Anker
Licensed content date	Jul 5, 2013
Start page	197
End page	204
Type of use	Dissertation/Thesis
Requestor type	Author of this Wiley article
Format	Electronic

REFERENCE

1. Kurkdjian, A.; Guern, J., *Annu. Rev. Plant Biol.* **1989,** *40*, 271-303.

2. Gillies, R. J.; Raghunand, N.; Garcia-Martin, M. L., et al., *IEEE Eng. Med. Biol.* **2004,** *23*, 57-64.

3. Liu, S. Q., *Int. J. Food Microbiol.* **2003,** *83*, 115-131.

4. Rousk, J.; Brookes, P. C.; Bååth, E., *Appl. Environ. Microbiol.* **2009,** *75*, 1589-1596.

5. Ziegler, C.; Göpel, W.; Hämmerle, H., et al., *Biosens. Bioelectron.* **1998,** *13*, 539-571.

6. Konttinen, Y. T.; Takagi, M.; Mandelin, J., et al., *J. Bone Miner. Res.* **2001,** *16*, 1780-1786.

7. Tan, W.; Shi, Z.; Smith, S., et al., *Science* **1992,** *258*, 778-781.

8. Holobar, A.; Weigl, B. H.; Trettnak, W., et al., *Sensor Actuat. B-Chem.* **1993,** *11*, 425-430.

9. Lee, S.; Ibey, B. L.; Coté, G. L., et al., *Sensor Actuat. B-Chem.* **2008,** *128*, 388-398.

10. Han, J.; Burgess, K., *Chem. Rev.* **2009,** *110*, 2709-2728.

11. Liebsch, G.; Klimant, I.; Krause, C., et al., *Anal. Chem.* **2001,** *73*, 4354-4363.

12. Zhang, Z.; Zhang, Y.; Ma, W., et al., *Anal. Chem.* **1989,** *61*, 202-205.

13. Hakonen, A.; Hulth, S., *Anal. Chim. Acta* **2008,** *606*, 63-71.

14. Wang, E.; Chow, K.-F.; Kwan, V., et al., *Anal. Chim. Acta* **2003,** *495*, 45-50.

15. Wencel, D.; MacCraith, B. D.; McDonagh, C., *Sensor Actuat. B-Chem.* **2009,** *139*, 208-213.

16. Butler, T. M.; MacCraith, B. D.; McDonagh, C., *J. Non-Cryst. Solids* **1998,** *224*, 249-258.

17. Lev, O.; Tsionsky, M.; Rabinovich, L., et al., *Anal. Chem.* **1995,** *67*, 22A-30A.

18. McDonagh, C.; Sheridan, F.; Butler, T., et al., *J. Non-Cryst. Solids* **1996,** *194*, 72-77.

19. Ismail, F.; Schoenleber, M.; Mansour, R., et al., *Analyst* **2011,** *136*, 807-815.

20. Puchberger-Enengl, D.; Krutzler, C.; Vellekoop, M. J. Sensors, 2011 IEEE, 2011, 679-682.

21. Nishi, T.; Forgac, M., *Nat Rev Mol Cell Biol* **2002,** *3*, 94-103.

22. Ohkuma, S.; Poole, B., *Proc Nat Acad Sci USA* **1978,** *75*, 3327-3331.

23. Monson, E.; Brasuel, M.; Philbert, M. A., et al., PEBBLE nanosensors for in vitro bioanalysis. In *Biomedical Photonics Handbook*, Vo-Dinh, T., Ed. CRC Press 2003.

24. Clark, H. A.; Hoyer, M.; Philbert, M. A., et al., *Anal. Chem.* **1999,** *71*, 4831-4836.

25. Ray, A.; Koo Lee, Y.-E.; Epstein, T., et al., *Analyst* **2011,** *136*, 3616-3622.

26. Cao, Y.; Lee Koo, Y.-E.; Kopelman, R., *Analyst* **2004,** *129*, 745-750.

27. Si, D.; Epstein, T.; Koo Lee, Y.-E., et al., *Anal. Chem.* **2011,** *84*, 978-986.

28. Park, E. J.; Brasuel, M.; Behrend, C., et al., *Anal. Chem.* **2003,** *75*, 3784-3791.

29. Xu, H.; Aylott, J. W.; Kopelman, R., *Analyst* **2002,** *127*, 1471-1477.

30. Xu, H.; Aylott, J. W.; Kopelman, R., et al., *Anal. Chem.* **2001,** *73*, 4124-4133.

31. Santra, S.; Zhang, P.; Wang, K., et al., *Anal. Chem.* **2001,** *73*, 4988-4993.

32. Arriagada, F. J.; Osseo-Asare, K., *J. Colloid Interface Sci.* **1995,** *170*, 8-17.

33. Santra, S.; Tapec, R.; Theodoropoulou, N., et al., *Langmuir* **2001,** *17*, 2900-2906.

34. Stöber, W.; Fink, A.; Bohn, E., *J. Colloid Interface Sci.* **1968,** *26*, 62-69.

35. Wang, L.; Wang, K.; Santra, S., et al., *Anal. Chem.* **2006,** *78*, 646-654.

36. Yan, J.; Estévez, M. C.; Smith, J. E., et al., *Nano Today* **2007,** *2*, 44-50.

37. He, X.; Duan, J.; Wang, K., et al., *J. Nanosci. Nanotechnol.* **2004,** *4*, 585-589.

38. Wang, L.; Tan, W., *Nano Lett.* **2005,** *6*, 84-88.

39. Wang, L.; Zhao, W.; O'Donoghu, M. B., et al., *Bioconjugate Chem.* **2007,** *18*, 297-301.

40. Wang, L.; Yang, C.; Tan, W., *Nano Lett.* **2004,** *5*, 37-43.

41. Zhao, X.; Tapec-Dytioco, R.; Tan, W., *J. Am. Chem. Soc.* **2003,** *125*, 11474-11475.

42. Chen, X.; Estévez, M. C.; Zhu, Z., et al., *Anal. Chem.* **2009,** *81*, 7009-7014.

43. Santra, S.; Yang, H.; Dutta, D., et al., *Chem. Commun.* **2004,** 2810-2811.

44. Turner, G. A., *Experientia* **1979,** *35*, 1657-1658.

45. Jähde, E.; Rajewsky, M. F.; Baumgärtl, H., *Cancer Res* **1982,** *42*, 1498-1504.

46. Buxton, R. B.; Wechsler, L. R.; Alpert, N. M., et al., *J Cereb Blood Flow Metab* **1984,** *4*, 8-16.

47. Tyler, J. L.; Diksic, M.; Villemure, J.-G., et al., *J. Nucl. Med.* **1987,** *28*, 1123-1126,NP-NP,1129-1133.

48. Schreml, S.; Meier, R. J.; Wolfbeis, O. S., et al., *Proc Nat Acad Sci USA* **2011,** *108*, 2432-2437.

49. Meier, R. J.; Schreml, S.; Wang, X.-d., et al., *Angew. Chem. Int. Ed.* **2011,** *50*, 10893-10896.

50. Smekal, A., *Naturwissenschaften* **1923,** *11*, 873-875.

51. C.V. Raman, K. S. K., *nature* **1928,** *122*, 169-169.

52. Kneipp, J.; Kneipp, H.; Wittig, B., et al., *Nanomed. Nanotech. Biol. Med.* **2010,** *6*, 214-226.

53. Kneipp, K.; Kneipp, H.; Itzkan, I., et al., *Chem. Rev.* **1999,** *99*, 2957-2976.

54. Mogilevsky, G.; Borland, L.; Brickhouse, M., et al., *International Journal of Spectroscopy* **2012,** *2012*, 12.

55. Day, J. S.; Edwards, H. G. M.; Dobrowski, S. A., et al., *Spectrochimica Acta Part A* **2004,** *60*, 563-568.

56. Edwards, H. G. M.; Brooke, C. J.; Tait, J. K. F., *J. Raman Spectrosc.* **1997,** *28*, 95-98.

57. Vandenabeele, P.; Verpoort, F.; Moens, L., *J. Raman Spectrosc.* **2001,** *32*, 263-269.

58. Fleischmann, M.; Hendra, P. J.; McQuillan, A. J., *Chem. Phys. Lett.* **1974,** *26*, 163-166.

59. Jeanmaire, D. L.; Van Duyne, R. P., *J. Electroanal. Chem. Interface Electrochem.* **1977,** *84*, 1-20.

60. Albrecht, M. G.; Creighton, J. A., *J. Am. Chem. Soc.* **1977,** *99*, 5215-5217.

61. Etchegoin, P. G.; Le Ru, E. C., *Phys. Chem. Chem. Phy.* **2008,** *10*, 6079-6089.

62. Aggarwal, R. L.; Farrar, L. W.; Greeneltch, N. G., et al., *Appl. Spectrosc.* **2012,** *66*, 740-743.

63. Han, X.; Wang, H.; Ou, X., et al., *J. Mater. Chem.* **2012,** *22*, 14127-14132.

64. Chen, J.; Jiang, J.; Gao, X., et al., *Chem. Eur. J.* **2008,** *14*, 8374-8382.

65. Bantz, K. C.; Meyer, A. F.; Wittenberg, N. J., et al., *PCCP* **2011,** *13*, 11551-11567.

66. McGlashen, M. L.; Davis, K. L.; Morris, M. D., *Anal. Chem.* **1990,** *62*, 846-849.

67. Michota, A.; Bukowska, J., *J. Raman Spectrosc.* **2003,** *34*, 21-25.

68. Bishnoi, S. W.; Rozell, C. J.; Levin, C. S., et al., *Nano Lett.* **2006,** *6*, 1687-1692.

69. Kneipp, J.; Kneipp, H.; Wittig, B., et al., *J. Phys. Chem. C* **2010,** *114*, 7421-7426.

70. Pallaoro, A.; Braun, G. B.; Reich, N. O., et al., *Small* **2010,** *6*, 618-622.

71. Jensen, R. A.; Sherin, J.; Emory, S. R., *Appl. Spectrosc.* **2007,** *61*, 832-838.

72. Wang, Z.; Bonoiu, A.; Samoc, M., et al., *Biosens. Bioelectron.* **2008,** *23*, 886-891.

73. Piotrowski, P.; Wrzosek, B.; Krolikowska, A., et al., *Analyst* **2014,** *139*, 1101-1111.

74. Doering, W. E.; Piotti, M. E.; Natan, M. J., et al., *Adv. Mater.* **2007,** *19*, 3100-3108.

75. Noble, J.; Attree, S.; Horgan, A., et al., *Anal. Chem.* **2012,** *84*, 8246-8252.

76. Maiti, K. K.; Dinish, U. S.; Samanta, A., et al., *Nano Today* **2012,** *7*, 85-93.

77. Dinish, U. S.; Balasundaram, G.; Chang, Y.-T., et al., *Sci. Rep.* **2014,** *4*.

78. Stuart, D. A.; Yuen, J. M.; Shah, N., et al., *Anal. Chem.* **2006,** *78*, 7211-7215.

79. Matousek, P.; Clark, I. P.; Draper, E. R. C., et al., *Appl. Spectrosc.* **2005,** *59*, 393-400.

80. Stone, N.; Baker, R.; Rogers, K., et al., *Analyst* **2007,** *132*, 899-905.

81. Matousek, P.; Morris, M. D.; Everall, N., et al., *Appl. Spectrosc.* **2005,** *59*, 1485-1492.

82. Stone, N.; Kerssens, M.; Lloyd, G. R., et al., *Chem. Sci.* **2011,** *2*, 776-780.

83. Xie, H.-n.; Stevenson, R.; Stone, N., et al., *Angew. Chem. Int. Ed.* **2012,** *51*, 8509-8511.

84. Sharma, B.; Ma, K.; Glucksberg, M. R., et al., *J. Am. Chem. Soc.* **2013,** *135*, 17290-17293.

85. Wang, F.; Liu, X., *Chem. Soc. Rev.* **2009,** *38*, 976-989.

86. Downing, E.; Hesselink, L.; Ralston, J., et al., *Science* **1996,** *273*, 1185-1189.

87. Pelc, J. S.; Ma, L.; Phillips, C. R., et al., *Opt. Express* **2011,** *19*, 21445-21456.

88. Joubert, M.-F., *Opt. Mater.* **1999,** *11*, 181-203.

89. Heer, S.; Lehmann, O.; Haase, M., et al., *Angew. Chem. Int. Ed.* **2003,** *42*, 3179-3182.

90. Feng, W.; Dev, K. C.; Zhengquan, L., et al., *Nanotechnology* **2006,** *17*, 5786.

91. Yi, G.; Lu, H.; Zhao, S., et al., *Nano Lett.* **2004,** *4*, 2191-2196.

92. Boyer, J.-C.; Vetrone, F.; Cuccia, L. A., et al., *J. Am. Chem. Soc.* **2006,** *128*, 7444-7445.

93. Boyer, J.-C.; Cuccia, L. A.; Capobianco, J. A., *Nano Lett.* **2007,** *7*, 847-852.

94. Vetrone, F.; Boyer, J.-C.; Capobianco, J. A., et al., *J. Appl. Phys.* **2004,** *96*, 661-667.

95. Wang, H.-Q.; Nann, T., *Acs Nano* **2009,** *3*, 3804-3808.

96. Yi, G. S.; Chow, G. M., *Adv. Funct. Mater.* **2006,** *16*, 2324-2329.

97. Chen, Z.; Chen, H.; Hu, H., et al., *J. Am. Chem. Soc.* **2008,** *130*, 3023-3029.

98. Wang, L.; Yan, R.; Huo, Z., et al., *Angew. Chem. Int. Ed.* **2005,** *44*, 6054-6057.

99. Li, Z.; Zhang, Y.; Jiang, S., *Adv. Mater.* **2008,** *20*, 4765-4769.

100. Ehlert, O.; Thomann, R.; Darbandi, M., et al., *Acs Nano* **2008,** *2*, 120-124.

101. Li, Z.; Zhang, Y., *Angew. Chem. Int. Ed.* **2006,** *45*, 7732-7735.

102. Nyk, M.; Kumar, R.; Ohulchanskyy, T. Y., et al., *Nano Lett.* **2008,** *8*, 3834-3838.

103. Idris, N. M.; Li, Z.; Ye, L., et al., *Biomaterials* **2009,** *30*, 5104-5113.

104. Nam, S. H.; Bae, Y. M.; Park, Y. I., et al., *Angew. Chem.* **2011,** *123*, 6217-6221.

105. Cannas, C.; Casu, M.; Mainas, M., et al., *J. Mater. Chem.* **2003,** *13*, 3079-3084.

106. Yang, J.; Zhang, C.; Peng, C., et al., *Chemistry – A European Journal* **2009,** *15*, 4649-4655.

107. Vetrone, F.; Naccache, R.; Juarranz de la Fuente, A., et al., *Nanoscale* **2010,** *2*, 495-498.

108. Lim, S. F.; Riehn, R.; Ryu, W. S., et al., *Nano Lett.* **2005,** *6*, 169-174.

109. Chatterjee, D. K.; Rufaihah, A. J.; Zhang, Y., *Biomaterials* **2008,** *29*, 937-943.

110. Cheng, L.; Yang, K.; Zhang, S., et al., *Nano Research* **2010,** *3*, 722-732.

111. Wang, M.; Mi, C.-C.; Wang, W.-X., et al., *Acs Nano* **2009,** *3*, 1580-1586.

112. Xiong, L.-Q.; Chen, Z.-G.; Yu, M.-X., et al., *Biomaterials* **2009,** *30*, 5592-5600.

113. Yu, X.-F.; Sun, Z.; Li, M., et al., *Biomaterials* **2010,** *31*, 8724-8731.

114. Shan, J.; Yong, Z.; Kian Meng, L., et al., *Nanotechnology* **2009,** *20*, 155101.

115. Zhang, P.; Steelant, W.; Kumar, M., et al., *J. Am. Chem. Soc.* **2007,** *129*, 4526-4527.

116. Qian, H. S.; Guo, H. C.; Ho, P. C.-L., et al., *Small* **2009,** *5*, 2285-2290.

117. Idris, N. M.; Gnanasammandhan, M. K.; Zhang, J., et al., *Nat Med* **2012,** *18*, 1580-1585.

118. Liu, Q.; Peng, J.; Sun, L., et al., *ACS Nano* **2011,** *5*, 8040-8048.

119. Zhang, J.; Li, B.; Zhang, L., et al., *Chem. Commun.* **2012,** *48*, 4860-4862.

120. Wang, Y.; Bao, L.; Liu, Z., et al., *Anal. Chem.* **2011,** *83*, 8130-8137.

121. Zhang, C.; Yuan, Y.; Zhang, S., et al., *Angew. Chem. Int. Ed.* **2011,** *50*, 6851-6854.

122. Wu, S.; Duan, N.; Ma, X., et al., *Anal. Chem.* **2012,** *84*, 6263-6270.

123. Zhang, P.; Rogelj, S.; Nguyen, K., et al., *J. Am. Chem. Soc.* **2006,** *128*, 12410-12411.

124. Liu, L.; Li, B.; Qin, R., et al., *Nanotechnology* **2010,** *21*, 285701.

125. Deng, R.; Xie, X.; Vendrell, M., et al., *J. Am. Chem. Soc.* **2011,** *133*, 20168-20171.

126. Sun, L.-N.; Peng, H.; Stich, M. I. J., et al., *Chem. Commun.* **2009,** 5000-5002.

127. Ali, R.; Saleh, S. M.; Meier, R. J., et al., *Sensor Actuat. B-Chem.* **2010,** *150*, 126-131.

128. Mader, H. S.; Wolfbeis, O. S., *Anal. Chem.* **2010,** *82*, 5002-5004.

129. Suyver, J. F.; Aebischer, A.; Garc ́a-Revilla, S., et al., *Phys. Rev. B* **2005,** *71*, 125123.

130. Wang, Y.; Tu, L.; Zhao, J., et al., *J. Phys. Chem. C* **2009,** *113*, 7164-7169.

131. Kumar, G. A.; Pokhrel, M.; Martinez, A., et al., *J. Alloys Compd.* **2012,** *513*, 559-565.

132. Kumar, V.; Rani, P.; Singh, D., et al., *R. Soc. Chem. Adv.* **2014,** *4*, 36101-36105.

133. Weissleder, R., *Nat Biotech* **2001,** *19*, 316-317.

134. Yu, X.; Li, M.; Xie, M., et al., *Nano Research* **2010,** *3*, 51-60.

135. Blasse, G., *Chem. Mater.* **1994,** *6*, 1465-1475.

136. Carpenter, C. M.; Sun, C.; Pratx, G., et al., *Med. Phys.* **2010,** *37*, 4011-4018.

137. Pratx, G.; Carpenter, C. M.; Sun, C., et al., *IEEE Trans. Med. Imag.* **2010,** *29*, 1992-1999.

138. Carpenter, C. M.; Pratx, G.; Sun, C., et al., *Phys. Med. Biol.* **2011,** *56*, 3487.

139. Badea, C. T.; Stanton, I. N.; Johnston, S. M., et al. 2012, 83130T-83130T-6.

140. Cong, W.; Pan, Z.; Filkins, R., et al., *J. Biomed. Opt.* **2014,** *19*, 076002-076002.

141. Chen, H.; Moore, T.; Qi, B., et al., *ACS Nano* **2013,** *7*, 1178-1187.

142. Chen, H.; Patrick, A. L.; Yang, Z., et al., *Anal. Chem.* **2011,** *83*, 5045-5049.

143. Chen, H.; Longfield, D. E.; Varahagiri, V. S., et al., *Analyst* **2011,** *136*, 3438-3445.

144. Zimmerli, W.; Waldvogel, F. A.; Vaudaux, P., et al., *J. Infect. Dis.* **1982,** *146*, 487-497.

145. Stinchfield, F. E.; Bigliani, L. U.; Neu, H. C., et al., *J. Bone Joint Surg. Am.* **1980,** *62*, 1345-1350.

146. Vertes, A.; Hitchins, V.; Phillips, K. S., *Anal. Chem.* **2012**.

147. Zimmerli, W., *Best Pract. Res. Clin. Rheumatol.* **2006,** *20*, 1045-1063.

148. Wirtanen, G.; Alanko, T.; Mattila-Sandholm, T., *Colloids Surf., B* **1996,** *5*, 319-326.

149. Szczotka-Flynn, L. B.; Imamura, Y.; Chandra, J., et al., *Cornea* **2009,** *28*, 918-926.

150. Burnett, S. L.; Chen, J.; Beuchat, L. R., *Appl. Environ. Microbiol.* **2000,** *66*, 4679-4687.

151. Vroom, J. M.; De Grauw, K. J.; Gerritsen, H. C., et al., *Appl. Environ. Microbiol.* **1999,** *65*, 3502-3511.

152. Piper, K. E.; Fernandez-Sampedro, M.; Steckelberg, K. E., et al., *PLoS ONE* **2010,** *5*, e9358.

153. Moran, E.; Byren, I.; Atkins, B. L., *J. Antimicrob. Chemother.* **2010,** *65*, iii45-iii54.

154. Piper, K. E.; Jacobson, M. J.; Cofield, R. H., et al., *J. Clin. Microbiol.* **2009,** *47*, 1878-1884.

155. Schiesser, M.; Stumpe, K. D. M.; Trentz, O., et al., *Radiology* **2003,** *226*, 391-398.

156. Xiong, Y. Q.; Willard, J.; Kadurugamuwa, J. L., et al., *Antimicrob. Agents Chemother.* **2005,** *49*, 380-387.

157. van Oosten, M.; Schäfer, T.; Gazendam, J. A. C., et al., *Nat Commun* **2013,** *4*.

158. Stewart, P. S.; Franklin, M. J., *Nat Rev Micro* **2008,** *6*, 199-210.

159. Zhang, T. C.; Fu, Y.-C.; Bishop, P. L., *Water Environ. Res* **1995,** *67*, 992-1003.

160. Damgaard, L. R.; Nielsen, L. P.; Revsbech, N. P., *Water Res.* **2001,** *35*, 1379-1386.

161. Hunter, R. C.; Beveridge, T. J., *Appl. Environ. Microbiol.* **2005,** *71*, 2501-2510.

162. Hidalgo, G.; Burns, A.; Herz, E., et al., *Appl. Environ. Microbiol.* **2009,** *75*, 7426-7435.

163. Wang, X.-d.; Meier, R. J.; Wolfbeis, O. S., *Angew. Chem. Int. Ed.* **2013,** *52*, 406-409.

164. Boas, D. A.; Brooks, D. H.; Miller, E. L., et al., *IEEE Signal Proc Mag* **2001,** *18*, 57-75.

165. Ntziachristos, V., *Nat Meth* **2010,** *7*, 603-614.

166. Farrell, T. J.; Wilson, B. C.; Patterson, M. S., *Phys. Med. Biol.* **1992,** *37*, 2281.

167. Hoover, E. E.; Squier, J. A., *Nat Photon* **2013,** *7*, 93-101.

168. Hell, S. W.; Wichmann, J., *Opt. Lett.* **1994,** *19*, 780-782.

169. Urban, Nicolai T.; Willig, Katrin I.; Hell, Stefan W., et al., *Biophys. J.* **2011,** *101*, 1277-1284.

170. Demaurex, N., *News Physiol Sci* **2002,** *17*, 1-5.

171. Talley, C. E.; Jusinski, L.; Hollars, C. W., et al., *Anal. Chem.* **2004,** *76*, 7064-7068.

172. Scaffidi, J.; Gregas, M.; Seewaldt, V., et al., *Anal. Bioanal. Chem.* **2009,** *393*, 1135-1141.

173. Bálint, Š.; Rao, S.; Marro, M., et al., *J. Raman Spectrosc.* **2011,** *42*, 1215-1221.

174. Kobzik, L., *J. Immunol.* **1995,** *155*, 367-376.

175. Tannock, I. F.; Rotin, D., *Cancer Res* **1989,** *49*, 4373-4384.

176. Dubach, J. M.; Harjes, D. I.; Clark, H. A., *J. Am. Chem. Soc.* **2007,** *129*, 8418-8419.

177. Kreft, O.; Javier, A. M.; Sukhorukov, G. B., et al., *J. Mater. Chem.* **2007,** *17*, 4471-4476.

178. Lee, Y.-E. K.; Kopelman, R., *Wiley Interdiscip Rev Nanomed Nanobiotechnol* **2009,** *1*, 98-110.

179. Volkan, M.; Stokes, D. L.; Vo-Dinh, T., *Appl. Spectrosc.* **2000,** *54*, 1842-1848.

180. Küstner, B.; Gellner, M.; Schütz, M., et al., *Angew. Chem. Int. Ed.* **2009,** *48*, 1950-1953.

181. Zhang, D.; Ansar, S. M.; Vangala, K., et al., *J. Raman Spectrosc.* **2010,** *41*, 952-957.

182. Roca, M.; Haes, A. J., *J. Am. Chem. Soc.* **2008,** *130*, 14273-14279.

183. Lee, J. R. I.; Willey, T. M.; Nilsson, J., et al., *Langmuir* **2006,** *22*, 11134-11141.

184. Kakiuchi, T.; Iida, M.; Imabayashi, S.-i., et al., *Langmuir* **2000,** *16*, 5397-5401.

185. Yamaguchi, A.; Namekawa, M.; Kamijo, T., et al., *Anal. Chem.* **2011,** *83*, 2939-2946.

186. Cunningham, D.; Littleford, R. E.; Smith, W. E., et al., *Faraday Discuss.* **2006,** *132*, 135-145.

187. Lee, C. T.; Smith, K. A.; Hatton, T. A., *Biochemistry* **2004,** *44*, 524-536.

188. Yang, H.-H.; Zhang, S.-Q.; Chen, X.-L., et al., *Anal. Chem.* **2004,** *76*, 1316-1321.

189. Vergne, I.; Constant, P.; Lanéelle, G., *Anal. Biochem.* **1998,** *255*, 127-132.

190. Möller, W.; Kreyling, W. G.; Kohlhäufl, M., et al., *J. Magn. Magn. Mater.* **2001,** *225*, 218-225.

191. Pratten, M. K.; Lloyd, J. B., *Biochim. Biophys. Acta* **1986,** *881*, 307-13.

192. Chan, Y.-H.; Wu, C.; Ye, F., et al., *Anal. Chem.* **2011,** *83*, 1448-1455.

193. Dou, X.; Jung, Y. M.; Cao, Z.-Q., et al., *Appl. Spectrosc.* **1999,** *53*, 1440-1447.

194. Ji, J.; Rosenzweig, N.; Griffin, C., et al., *Anal. Chem.* **2000,** *72*, 3497-3503.

195. Gong, J.-L.; Jiang, J.-H.; Liang, Y., et al., *J. Colloid Interface Sci.* **2006,** *298*, 752-756.

196. Ma, Z. Y.; Dosev, D.; Kennedy, I. M., *Nanotechnology* **2009,** *20*, 085608.

197. Fernando, L. P.; Kandel, P. K.; Yu, J., et al., *Biomacromolecules* **2010,** *11*, 2675-2682.

198. Bryers, J. D., *Biotechnol. Bioeng.* **2008,** *100*, 1-18.

199. Hetrick, E. M.; Schoenfisch, M. H., *Chem. Soc. Rev.* **2006,** *35*, 780.

200. Mody, R. M.; Zapor, M.; Hartzell, J. D., et al., *J. Trauma Acute Care Surg.* **2009,** *67*, 758-761.

201. Ehrlich, G. D.; Stoodley, P.; Kathju, S., et al., *Clin. Orthop. Relat. Res.* **2005,** 59-66.

202. Costerton, J. W.; Stewart, P. S.; Greenberg, E. P., *Science* **1999,** *284*, 1318-1322.

203. Trampuz, A.; Piper, K. E.; Jacobson, M. J., et al., *N Engl J Med* **2007,** *357*, 654-663.

204. Esposito, S.; Leone, S., *Int. J. Antimicrob. Ag.* **2008,** *32*, 287-293.

205. Wike-Hooley, J. L.; Haveman, J.; Reinhold, H. S., *Radiother. Oncol.* **1984,** *2*, 343-366.

206. Rottenberg, D. A.; Ginos, J. Z.; Kearfott, K. G., et al., *Ann. Neurol.* **1985,** *17*, 70-79.

207. Gu, B.; Yin, M.-J.; Zhang, A. P., et al., *Opt. Express* **2009,** *17*, 22296-22302.

208. Wang, F.; Widejko, R. G.; Yang, Z., et al., *Anal. Chem.* **2012,** *84*, 8013-8019.

209. Haase, M.; Schäfer, H., *Angew. Chem. Int. Ed.* **2011,** *50*, 5808-5829.

210. Wang, F.; Banerjee, D.; Liu, Y., et al., *Analyst* **2010,** *135*, 1839-1854.

211. Ong, L. C.; Gnanasammandhan, M. K.; Nagarajan, S., et al., *Luminescence* **2010,** *25*, 290-293.

212. Wang, C.; Tao, H.; Cheng, L., et al., *Biomaterials* **2011,** *32*, 6145-6154.

213. Chatterjee, D. K.; Gnanasammandhan, M. K.; Zhang, Y., *Small* **2010,** *6*, 2781-2795.

214. Salthouse, C.; Hilderbrand, S.; Weissleder, R., et al., *Opt. Express* **2008,** *16*, 21731-21737.

215. Yang, Y.; Shao, Q.; Deng, R., et al., *Angew. Chem. Int. Ed.* **2012,** *51*, 3125-3129.

216. Wang, L.; Yan, R.; Huo, Z., et al., *Angew. Chem.* **2005,** *117*, 6208-6211.

217. Wang, J.; Wang, F.; Wang, C., et al., *Angew. Chem. Int. Ed.* **2011,** *50*, 10369-10372.

218. Wang, F.; Deng, R.; Wang, J., et al., *Nat Mater* **2011,** *10*, 968-973.

219. Gruber, J. B.; Quagliano, J. R.; Reid, M. F., et al., *Phys. Rev. B* **1993,** *48*, 15561-15573.

220. Makote, R.; M. Collinson, M., *Anal. Chim. Acta* **1999,** *394*, 195-200.

221. Kirkland, J. J.; Henderson, J. W.; DeStefano, J. J., et al., *J. Chromatogr. A* **1997,** *762*, 97-112.

222. O'Neal, D. P.; Meledeo, M. A.; Davis, J. R., et al., *IEEE Sens. J.* **2004,** *4*, 728-734.

223. Wilson, K.; Homan, K.; Emelianov, S., *Nat Commun* **2012,** *3*, 618.

224. Ray, A.; Yoon, H. K.; Koo Lee, Y. E., et al., *Analyst* **2013,** *138*, 3126-3130.

225. Xing, M.; Cao, W.; Pang, T., et al., *Solid State Commun.* **2009,** *149*, 911-914.

226. Vertes, A.; Hitchins, V.; Phillips, K. S., *Anal. Chem.* **2012,** *84*, 3858-3866.

227. Zalavras, C.; Christensen, T.; Rigopoulos, N., et al., *Clinical Orthopaedics and Related Research®* **2009,** *467*, 1715-1720.

228. Mody, R. M.; Zapor, M.; Hartzell, J. D., et al., *J. Trauma Acute Care Surg.* **2009,** *67*, 758-761 10.1097/TA.0b013e3181af6aa6.

229. Sjollema, J.; Sharma, P. K.; Dijkstra, R. J. B., et al., *Biomaterials* **2010,** *31*, 1984-1995.

230. Stewart, P. S.; William Costerton, J., *Lancet* **2001,** *358*, 135-138.

231. Esmonde-White, K. A.; Esmonde-White, F. W. L.; Holmes, C. M., et al., *Diabetes Care* **2013,** *36*, 3652-3654.

232. Abu-Amer, Y.; Darwech, I.; Clohisy, J., *Arthritis Res. Ther.* **2007,** *9*, S6.

233. Anderson, J. M.; Rodriguez, A.; Chang, D. T., *Semin. Immunol.* **2008,** *20*, 86-100.

234. Shen, Y.; Liu, W.; Wen, C., et al., *J. Mater. Chem.* **2012,** *22*, 8662-8670.

235. Liu, X.; Liao, Q.; Wang, H., *Opt. Lett.* **2013,** *38*, 4530-4533.

236. Li, C.; Di, K.; Bec, J., et al., *Opt. Lett.* **2013,** *38*, 2339-2341.

237. Chen, D.; Zhu, S.; Yi, H., et al., *Med. Phys.* **2013,** *40*, 031111.

238. Tseng, T.-K.; Choi, J.; Jacobsohn, L., et al., *Appl. Phys. A* **2010,** *100*, 1137-1142.

239. Wang, F.; Raval, Y.; Chen, H., et al., *Adv. Healthcare Mater.* **2014,** *3*, 197-204.

240. Pratx, G.; Carpenter, C. M.; Sun, C., et al., *Opt. Lett.* **2010,** *35*, 3345-3347.

241. Cubeddu, R.; Pifferi, A.; Taroni, P., et al., *Appl. Phys. Lett.* **1999,** *74*, 874-876.

242. Farrell, T. J.; Patterson, M. S.; Wilson, B., *Med. Phys.* **1992,** *19*, 879-888.

243. Ge, J.; Zhao, L.; Chen, L.-R., et al., *J. Chromatogr. Sci.* **2010,** *48*, 29-34.

244. Helmchen, F.; Denk, W., *Nat Meth* **2005,** *2*, 932-940.

245. Drlica, K.; Zhao, X., *Microbiol. Mol. Biol. Rev.* **1997,** *61*, 377-92.

246. Sanders, C. C., *Rev. Infect. Dis.* **1988,** *10*, 516-527.

247. StepanoviĆ, S.; VukoviĆ, D.; Hola, V., et al., *APMIS* **2007,** *115*, 891-899.

248. Stepanović, S.; Vuković, D.; Dakić, I., et al., *J. Microbiol. Methods* **2000,** *40*, 175-179.

249. Wencel, D.; Barczak, M.; Borowski, P., et al., *J. Mater. Chem.* **2012,** *22*, 11720-11729.

250. Oesch, U.; Ammann, D.; Simon, W., *Clin. Chem.* **1986,** *32*, 1448-59.

251. Hu, Q. Development and characterization of fluorescent pH sensors based on porous silica and hydrogel support matrices. Dissertation, 2013.

252. Menkin, V.; Warner, C. R., *Am. J. Pathol.* **1937,** *13*, 25-44.1.

253. Niinikoski, J.; Grislis, G.; Hunt, T. K., *Ann. Surg.* **1972,** *175*, 588-593.